Integrated Servo-Mechanical Design of High-Performance Mechanical Systems

Yan Zhi Tan

NATIONAL UNIVERSITY OF SINGAPORE

2014

Integrated Servo-Mechanical Design of High-Performance Mechanical Systems

Yan Zhi Tan

B.Eng. (Hons.), National University of Singapore, 2010

A DISSERTATION SUBMITTED

FOR THE DEGREE OF DOCTOR OF PHILOSOPHY

NUS GRADUATE SCHOOL FOR INTEGRATIVE SCIENCES AND ENGINEERING

NATIONAL UNIVERSITY OF SINGAPORE

2014

Declaration

I hereby declare that this thesis is my original work and it has been written by me in its entirety. I have duly acknowledged all the sources of information which have been used in the thesis.

This thesis has also not been submitted for any degree in any university previously.

Tan Yan Zhi

5 December 2014

Acknowledgements

To begin, I am indebted to my supervisors Prof. Lee Tong Heng, Prof. Pang Chee Khiang, Justin, and Prof. Hong Fan. I am also grateful to Prof. Chen Benmei for being the Chair of my Thesis Advisory Committee. They have been great teachers who have taught me lessons both in life and research, and they have opened up many opportunities for my career. I hold them in high regards for their enthusiasm and passion in imparting knowledge and conducting world-class research.

I wish to thank Prof. Ng Tsan Sheng, Adam of NUS Department of Industrial and Systems Engineering for his invaluable comments and suggestions on robust optimization. I am also grateful to Dr. Teo Tat Joo of A*STAR Singapore Institute of Manufacturing Technology for the collaboration.

I would like to thank Prof. Won Sanchul of Pohang University of Science and Technology for the research internship opportunity. I am also thankful to Prof. Masayoshi Tomizuka of University of California, Berkeley, for the research attachment opportunity. Both overseas research experiences have been invaluable to me.

I am grateful to my parents Mr. Tan Boon Teong and Mdm. Seah Lee Tiang for their upbringing, love and support. It has been an arduous journey. I want to thank my best friends of twelve years and running, Mr. Lee Guangyi, Mr. Toh Zong Rong, Ms. Choo Jiahui, Ms. Ong Hanwei, and Ms. Seet Zhiyue, for the conversations, get-togethers, and adventures, *etc.* In addition, I would like to thank all members of the research group for the discussions and assistance. I am also thankful to NUS Graduate School for Integrative Sciences and Engineering Scholars' Alliance (NGSSA) for adding more colors to my Ph.D. journey.

Last but not least, I would like to thank NGS for the financial support in the form of a Research Scholarship. I would also like to thank the staffs of NGS, as well as the staffs of Control & Simulation and Mechatronics & Automation Laboratory, NUS Department of Electrical and Computer Engineering, who have aided me in one way or another to make this dissertation possible.

The thought of pursuing a Ph.D. had never crossed my mind when I began my undergraduate studies with the department of Electrical and Computer Engineering, NUS. This journey has pushed me out of my comfort zones, exploring uncharted territories, experiencing setbacks, and not remembering how many times I nearly wanted to call it quits. However, it is also this experience that has helped develop my tenacity and perseverance, which I believe will serve me well for the journey ahead...

Abbreviations

CAD	Computer-Aided Design
CVaR	Conditional-Value-at-Risk
DBIT	Discrete Bode's Integral Theorem
EUV	Extreme Ultra-Violet
FEA	Finite Element Analysis
FIR	Finite Impulse Response
GKYP	Generalized Kalman-Yakubovich-Popov
HDD	Hard Disk Drive
i.i.d.	Independent and Identically Distributed
LMI	Linear Matrix Inequality
LQE	Linear Quadratic Estimator
LQR	Linear Quadratic Regulator
LTI	Linear Time-Invariant
MagLev	Magnetic Levitation

NRRO	Non-Repeatable Run-Out
PZT	Pb-Zr-Ti
R&D	Research & Development
SISO	Single-Input-Single-Output
Tbit	Terabit
VCM	Voice Coil Motor
ZOH	Zero-Order Hold

Contents

Summary

High-performance mechatronics are required to satisfy specifications such as high control bandwidth, attenuation of disturbances at high frequencies, and robust stability in the presence of plant parametric perturbations. In the traditional cyclical research and development process for mechatronics, the achieved feedback control performance may be limited by the mechanical plant design. In this dissertation, novel integrated servo-mechanical design algorithms are proposed for reshaping the high-frequency response of a single-input-single-output mechanical plant to satisfy performance specifications and individual chance-constrained robust stability criterion.

First, the reshaping of the high-frequency response of a plant based on a low-order controller is proposed. The low-order controller is designed to compensate for the frequency response of the original mechanical plant at low frequencies, and plant design variables are introduced using Youla parametrization. Performance specifications are specified as finite frequency bounded realness constraints on the sensitivity transfer function, and the Generalized Kalman-Yakubovich-Popov (GKYP) Lemma is used for translating the constraints into Linear Matrix Inequalities (LMIs).

Next, a convex separable parametrization is proposed for reshaping the high-frequency responses of both the mechanical plant and a low-order controller. The performance specifications are similarly represented as LMI constraints using the GKYP Lemma, and an individual chance-constrained robust stability criterion which is based solely on the mean, variance, and support of the plant parameter distributions is included. A tractable approximation of the robust stability criterion under the conditional-value-at-risk measure is proposed. As a result, the robust stability criterion is formulated as several LMI and linear inequality constraints, where the LMI constraints are obtained by translating positive realness constraints using the GKYP Lemma. The design variables are solved simultaneously, and the parameterization is readily separable for obtaining the redesigned mechanical plant and controller.

The performance specifications and chance-constrained robust stability criterion can be visualized on the Nyquist plane, and a graphical approach is proposed for redesigning the mechanical plant based on a low-order controller to satisfy the specifications. Allowable regions for the Nyquist plot of the open loop transfer function are derived based on the bounded-real performance and positive-real robust stability specifications. The relation between Bounded Real Lemma and Positive Real Lemma is used for converting the positive realness constraint from the robust stability criterion into an equivalent bounded realness constraint. In order for tradeoff between performance specifications and robust stability criterion to be easily observed using a single measure on the Nyquist plane, the equivalent bounded realness constraint is approximated using Triangle Inequality.

This dissertation presents GKYP-Lemma based algorithms for satisfying performance and chance-constrained robust stability specifications by finite frequency reshaping of the mechanical plant. The effectiveness of the proposed algorithms is verified in simulations using the Pb-Zr-Ti active suspension from a commercial 3.5” dual-stage hard disk drive, which is an example of high-performance mechatronics.

List of Tables

List of Figures

Chapter 1

Introduction

Mechatronics is usually defined as a synergistic combination of electronics, mechanics, computer, and control [1]. Today, mechatronics is present in a wide range of products ranging from consumer electronics such as desktop printers, digital cameras, and Hard Disk Drives (HDDs), to industrial manufacturing equipment such as industrial robots, wafer positioning stages, and atomic force microscopes. Wafer positioning stages, atomic force microscopes, and servo systems in HDDs are examples of high-performance mechatronics which are capable of nanoscale resolution.

1.1 Servo-Mechanical-Prototype Production Cycle

The demand for smaller electronic devices, larger computational power, and larger digital storage capabilities, *etc*, is ever increasing. Based on the international technology roadmap for semiconductors [2], the manufacturing of integrated circuits will reach the few nanometers range within the next fifteen years. As a result, the precision of semiconductor manufacturing equipment such as wafer stages and atomic force microscopes have to be increased. In addition, the precision of HDD servo systems have to be increased further as areal densities of HDDs in production are driven towards 10 Tbit/in^2 [3] in order to satisfy the storage demands by data centers. As such, satisfying control specifications of high-performance mechatronics is getting more challenging in many areas of application.

In a typical production cycle for mechatronic products as shown in Figure 1.1, the business unit determines the requirements for the next generation of products based on consumers' feedback, market forces, and technological innovations. The Research & Development (R&D) cycle for satisfying the requirements is an iterative process comprising of the mechanical structure design, prototype manufacture and evaluation, and servo system analysis stages, where each stage begins only after the completion of the previous stages [4].

In the servo system analysis stage, the tracking accuracy of the high-performance mechatronic system has to be ensured in the presence of mechanical vibrations, external vibrations, and measurement noise. Disturbance observers [5–7] and peak filters [8–10] are commonly augmented to controllers for rejecting external vibrations. To reduce disturbances resulting from the mechanical vibrations, common methods include the phase-stabilization of in-phase resonant modes [8, 11–13] and changing of the mechanical properties of the out-of-phase plant to in-phase using peak filters [14].

The feedback control system is also required to be robustly stable in the presence of plant parametric perturbations resulting from mass pro-

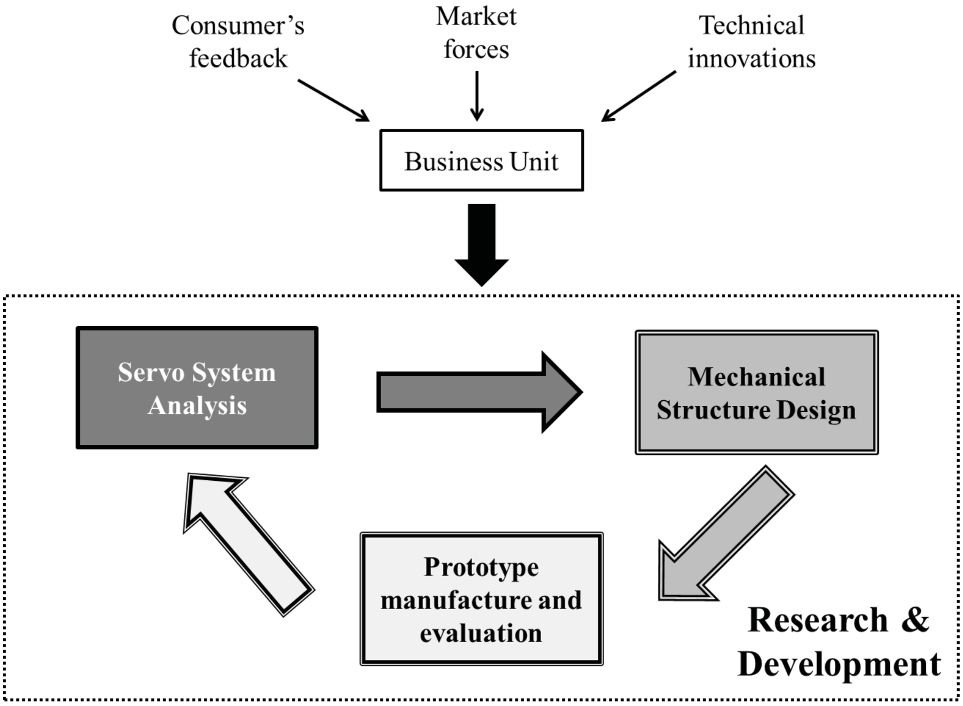

Figure 1.1: Typical servo-mechanical-prototype cycle for production of mechatronic products [4].

duction, variations in operating conditions, mechanical wear, *etc.* In the production of high quality and low cost mechatronic products such as the HDD, the feedback control system is required to be stable for a given proportion of the manufactured HDDs in order to satisfy a desired defect tolerance level. Robust controller design methods are commonly based on the $\mathcal{H}_\infty$ theory [15] considering norm-bounded uncertainties, as well as Kharitonov's theorem [16] considering interval polynomials. Controller design using probabilistic and randomized methods [17] are proposed recently for improving the performance of feedback control systems, as the worst case approach for considering uncertainties can be too conservative [17].

The dynamical performance of the overall control system is well known to be dependent on both the controller and mechanical designs [18, 19].

As such, the achievable performance and robust stability of the feedback control system may be limited by the mechanical plant.

1.2 Performance Limitations of Feedback Control

The dynamics of many mechatronic systems can be modeled as a Linear Time-Invariant (LTI) system when the operating range in consideration is close to an equilibrium point. In this dissertation, the main performance objective is achieving high-frequency disturbance attenuation for improving tracking accuracy. As such, the performance limitations of feedback control involving LTI systems are discussed in this section.

A typical discrete-time feedback control system is shown in Figure 1.2, where $C(z)$ is a feedback controller, u and y represent the input and output of a mechanical plant $P(z)$, respectively, r represents the reference signal given to the overall control system, and w represents the output disturbance.

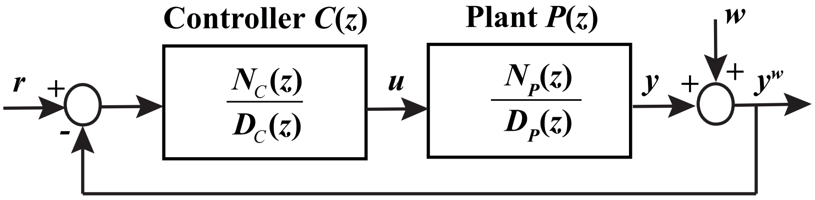

Figure 1.2: Block diagram of a typical discrete-time feedback control system.

1.2.1 Limitations by Resonant Poles of Mechanical Plant

The closed-loop from w to y^w as shown in Figure 1.2 corresponds to the sensitivity transfer function $S(z)$ which is given by

$$S(z) = \frac{D_P(z)D_C(z)}{N_P(z)N_C(z) + D_P(z)D_C(z)}, \tag{1.1}$$

where $N_C(z)$ and $N_P(z)$ are the zero polynomials of $C(z)$ and $P(z)$, respectively, and $D_C(z)$ and $D_P(z)$ are the pole polynomials of $C(z)$ and $P(z)$, respectively. Many performance specifications of the overall control system can be characterized as magnitude constraints on $S(z)$.

The resonant poles of $P(z)$ are the zeros of $S(z)$ as seen from (1.1). When $C(z)$ is a low-order controller and the resonant frequencies of $P(z)$ are fixed, disturbance attenuation capabilities at high frequencies can only be achieved by decreasing the damping ratios of the poles of $P(z)$ in $D_P(z)$.

1.2.2 Limitations by Unshifted Anti-Resonant Zeros of Mechanical Plant

In mechanical design, the anti-resonant zeros of a mechanical plant indicate the in-phase/out-of-phase property of the resonant modes. The frequency response of a mechanical plant with in-phase resonant modes is shown in Figure 1.3, where it can be seen that there are no unstable anti-resonant zeros. From the frequency response of a mechanical plant with an out-of-phase secondary resonant mode, it can be seen that there are unstable zeros between the resonant modes. The anti-resonant zeros result in the blocking of certain signal frequencies by the mechanical plant in control design. As such, it is desirable to have only stable anti-resonant zeros in the presence of mechanical resonant modes.

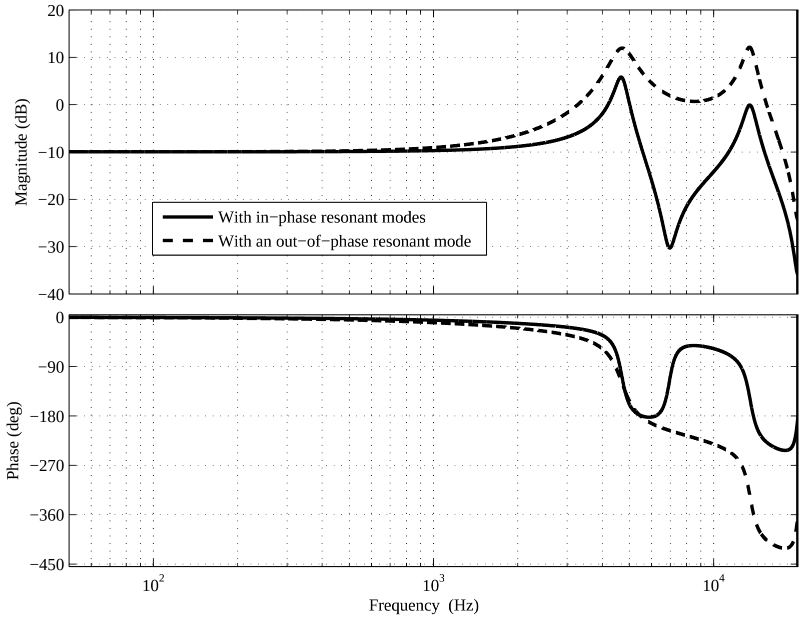

Figure 1.3: Frequency responses of mechanical plants with in-phase and out-of-phase resonant modes.

The complementary sensitivity transfer function $T(z)$ is a representation of the closed-loop from r to y in Figure 1.2, and is given by

$$T(z) = \frac{N_P(z)N_C(z)}{N_P(z)N_C(z) + D_P(z)D_C(z)}. \tag{1.2}$$

From (1.2), it can be seen that the unstable anti-resonant zeros of $P(z)$ are the unstable anti-resonant zeros of $T(z)$ when $N_C(z)$ is Schur stable.

The locations of the unstable anti-resonant zeros are not shifted by feedback control and limit the achievable performance of the feedback control system. In the presence of unstable anti-resonant zeros, an undershoot will be seen at the beginning of the time responses with lengthened settling time. In the frequency domain, the closed-loop bandwidth has to be lowered as the additional phase lag introduced by the unstable anti-resonant zeros reduces the phase margin. According to the Discrete Bode's Integral Theorem (DBIT), the magnitude of $S(z)$ is significantly greater than one at frequencies above the open loop bandwidth [20].

1.3 Integrated Servo-Mechanical Design

Integrated mechatronic design is the simultaneous consideration of electronics, mechanical, computer, and control components. According to [21], 43% of more than 140 enterprises are implementing and altering new product development processes for a multi-disciplinary approach to improving the development of mechatronic products, with the top-performing manufacturers being twice as likely to do so. Integrated servo-mechanical design is a subset of the more complex integrated mechatronic design problem as shown in Figure 1.4. In other words, the focus is on considering mechanical and control components simultaneously to satisfy performance specifications and robust stability criterion of the overall feedback control system, and can be used for overcoming the limitations discussed in Sections 1.1 and 1.2.

From a theoretical perspective, integrated servo-mechanical design is generally a nonlinear and nonconvex optimization problem. As discussed in [22], the approaches can be classified into iterative [23–27], nested [28–30], and simultaneous [31–36] optimization strategies. In [31], the sensitivities of the objective functions with respect to the plant parameters are used to formulate a gradient-based approach for simultaneous optimization.

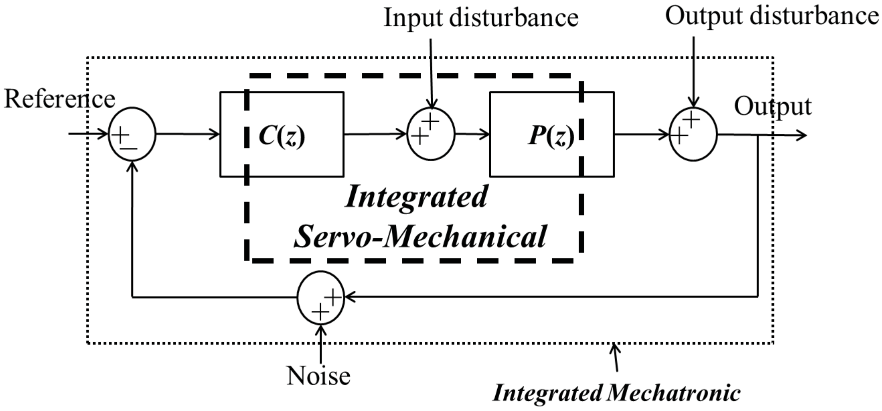

Figure 1.4: Integrated servo-mechanical.

A bond graph model of the mechanical plant is used in [33] for reducing the number of design variables and solving using physical programming. Evolutionary algorithms are used in [34, 36] for solving the simultaneous optimization problem. The solutions are commonly obtained by solving Linear Matrix Inequality (LMI)-based constraints iteratively [25–27, 32]. In [35], a non-iterative LMI-based method is proposed for simultaneous design of the controller and plant damping variable. A design for control approach is proposed in [19], where the focus is on designing the mechanical structure to obtain a simple dynamic model for ease of controller design. Simultaneous design of structure and control using $\mathcal{H}_2$ and $\mathcal{H}_\infty$ robust control formulations is approximated by a decoupled optimization approach in which the structures are optimized by shaping the structural singular values [37]. In [38–40], the sensor or actuator placement problem was solved using the integrated system design by separation approach, where simultaneous optimization of plant and controller parameters is avoided by designing the plant to have certain desired properties. A plant/controller design integration method for $\mathcal{H}_\infty$ loop-shaping using the Sum of Roots algebraic approach is proposed in [41]. In [25, 27, 37, 40], deterministic norm-bounded uncertainties are considered in the design phase.

From an experimental perspective, bandwidth estimation based on integrated servo-mechanical design of a HDD actuator is proposed in [42]. In [43], finite element modeling of the characteristics of a HDD actuator for effective integrated servo-mechanical design is presented. It is proposed in [44] that the servo-bandwidth of the head-positioning system in HDDs can be increased by redesigning the mode shape of the primary resonant mode such that its residue is reduced. The Pb-Zr-Ti (PZT) actuation system in a dual-stage HDD is made to have in-phase resonant modes in [45] by changing the directions of actuation of the PZT actuators.

1.4 Notations

The following notations are used in this dissertation. $\mathcal{RH}_\infty$ represents the real rational subspace of $\mathcal{H}_\infty$ which consists of all proper and real rational stable transfer matrices, and I denotes an identity matrix of appropriate dimensions. For a matrix Φ, its transpose, complex conjugate transpose, and Moore-Penrose inverse are denoted by appropriate dimension matrices Φ^T, Φ^*, and Φ^+, respectively. If Φ is Hermitian, $\Phi > (\geq) 0$ and $\Phi < (\leq) 0$ denote positive (semi) definiteness and negative (semi) definiteness, respectively. For simplicity, a discrete-time transfer function such as $P(z)$ is represented using P, and $P(e^{j\theta})$ is represented as $P(\theta)$ when emphasis of the dependence on angular frequency θ is required, unless otherwise stated.

1.5 GKYP Lemma

Performance and robust stability specifications are represented as finite frequency bounded realness and positive realness constraints in this dissertation. These constraints are formulated as LMIs using the Generalized Kalman-Yakubovich-Popov (GKYP) Lemma [46] in this section.

Consider (A_G, B_G, C_G, D_G) as a stable state-space realization of a square transfer matrix $G \in \mathcal{RH}_\infty$. The following theorem is the GKYP Lemma in discrete-time domain. The strict inequality is used as the state-space matrices considered are non-minimal representations of the system.

Theorem 1.1. *Let $\bar{\theta} := [\theta_{\bar{l}}, \theta_{\bar{u}}]$ denote a finite frequency range, where $\theta_{\bar{l}} \leq \theta_{\bar{u}}$, and $\theta_{\bar{l}}, \theta_{\bar{u}} \in [0, \pi]$. Given matrices A, B, and Hermitian matrices Θ, Φ, and Ψ, the following statements are equivalent*

(i) The frequency domain inequality given by

$$\begin{bmatrix} (e^{j\theta} I - A_G)^{-1} B_G \\ I \end{bmatrix}^* \Theta \begin{bmatrix} (e^{j\theta} I - A_G)^{-1} B_G \\ I \end{bmatrix} < 0 \qquad (1.3)$$

holds for all $\theta \in \bar{\theta}$.

(ii) There exist Hermitian matrices Ξ and $V > 0$ such that

$$\begin{bmatrix} A_G & B_G \\ I & 0 \end{bmatrix}^* \Pi \begin{bmatrix} A_G & B_G \\ I & 0 \end{bmatrix} + \Theta < 0, \qquad (1.4)$$

where $\Pi = (\Phi \otimes \Xi + \Psi \otimes V)$ *with*

$$\Phi = \begin{bmatrix} 1 & 0 \\ 0 & -1 \end{bmatrix} \text{ and } \Psi = \begin{bmatrix} 0 & \nu \\ \nu^* & \kappa\,(2cos\theta_R) \end{bmatrix}. \tag{1.5}$$

The values of scalars θ_R, ν, *and* κ *in* Ψ *for different choices of* $\bar{\theta}$ *are given in Table 1.1.*

Table 1.1: θ_R, ν, and κ for Different Frequency Range

$\bar{\theta}$	$\theta \le \theta_{\bar{u}}$	$\theta_{\bar{l}} \le \theta \le \theta_{\bar{u}}$	$\theta \ge \theta_{\bar{l}}$
θ_R	$\theta_{\bar{u}}$	$(\theta_{\bar{u}} - \theta_{\bar{l}})/2$	$\theta_{\bar{l}}$
ν	1	$e^{j((\theta_{\bar{l}}+\theta_{\bar{u}})/2)}$	-1
κ	-1	-1	1

The following corollaries demonstrate the use of GKYP Lemma to represent finite frequency bounded realness and $\mathrm{Re}(G(e^{j\theta})) > \varrho$ by an appropriate choice of Θ.

Corollary 1.1. *For a given* $\phi \in \mathbb{R}^+$, $\left\|G(e^{j\theta})\right\|_\infty < \phi$ *for all* $\theta \in \bar{\theta}$ *iff there exist Hermitian matrices* Ξ *and* $V > 0$ *such that*

$$\begin{bmatrix} \begin{bmatrix} A_G & B_G \\ I & 0 \end{bmatrix}^* \Pi \begin{bmatrix} A_G & B_G \\ I & 0 \end{bmatrix} + \begin{bmatrix} 0 & 0 \\ 0 & -\chi I \end{bmatrix} & \begin{bmatrix} {C_G}^* \\ {D_G}^* \end{bmatrix} \\ \begin{bmatrix} C_G & D_G \end{bmatrix} & -\beta I \end{bmatrix} < 0, \tag{1.6}$$

which is obtained by applying Schur's complement to (1.4) with

$$\Theta = \begin{bmatrix} \frac{{C_G}^* C_G}{\beta I} & \frac{{C_G}^* D_G}{\beta I} \\ \frac{D_G {C_G}^*}{\beta I} & \frac{{D_G}^* D_G}{\beta I} - \chi I \end{bmatrix}. \tag{1.7}$$

In (1.6) and (1.7), $\chi = \phi^2$ and $\beta = 1$. With the application of Schur's complement to (1.6), $\chi = \phi$ and $\beta = \phi$, and ϕ can be an optimization variable.

Corollary 1.2. *For all $\theta \in \bar{\theta}$, $\mathrm{Re}\big(G(e^{j\theta})\big) > \varrho$ for $\varrho \in \mathbb{R}$ iff there exist Hermitian matrices Ξ and $V > 0$ such that*

$$\begin{bmatrix} A_G & B_G \\ I & 0 \end{bmatrix}^* \Pi \begin{bmatrix} A_G & B_G \\ I & 0 \end{bmatrix} + \Theta < 0, \tag{1.8}$$

where

$$\Theta = \begin{bmatrix} 0 & -{C_G}^* \\ -C_G & -D_G - {D_G}^* + 2\varrho \end{bmatrix}. \tag{1.9}$$

The above corollaries will be used by the proposed integrated servo-mechanical design algorithms for specifying finite frequency constraints on the sensitivity transfer function, removing unstable zeros, and ensuring robust stability.

1.6 Phase-Stable Design and Sensitivity Disc

Non-Repeatable Run-Out (NRRO) is generally classified into NRRO induced by mechanical vibrations of the resonant modes and NRRO resulting from external disturbances. In this dissertation, the focus of integrated servo-mechanical design is on the attenuation of the former. With the use of notch filters for gain stabilization of resonant modes, control actions for damping the vibration will be annihilated. As such, NRRO is trapped in the frequency regions of the out-of-phase resonant modes [14], and tracking accuracy will be reduced. Phase-stable design [11] is a well-known method for satisfying high-frequency disturbance attenuation specifications, which is guaranteed using the proposed algorithms in this dissertation.

The Nyquist plot of an open loop transfer function PC with phase-stabilized resonant modes is as shown in Figure 1.5. The dotted unit circle centered at the origin denotes the unit disc, and σ_1 is the well-established phase margin. For a phase-stable design, the Nyquist curve leaves and re-enters the unit disc at least once. The dotted straight line from the origin to the Nyquist curve indicate a point which is furthest away from the origin, and corresponds to the peak of the phase-stabilized resonant mode in the open loop transfer function. In addition, the Nyquist stability criterion is satisfied by not encircling $(-1 + j0)$ if there are no unstable mechanical poles. The angle σ_2 as shown in Figure 1.5 represents the secondary phase margin, and a rule-of-thumb for guaranteeing stability is $\sigma_2 \geq 40^\circ$. The rule-of-thumb is also applicable to tertiary phase margins when there are multiple phase-stabilized resonant modes.

The bold dashed unit circle centered at $(-1+j0)$ as shown in Figure 1.5 is known as the sensitivity disc [14]. The avoidance of the unit sensitivity disc by the open loop transfer function PC corresponds to $|1+PC| > 1$ over a specific frequency range. As such, the magnitude of the sensitivity transfer function over the same frequency is given by $|S| = |1+PC|^{-1} < 1$, which corresponds to disturbance attenuation. From the concepts of phase-stable design and sensitivity disc, it can be seen that disturbance attenuation capabilities exist at the resonant frequencies of the phase-stabilized resonant

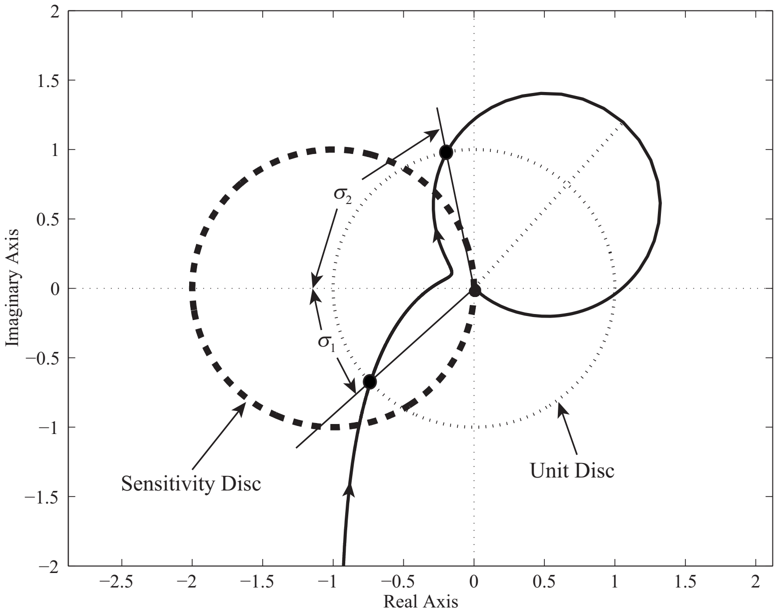

Figure 1.5: Nyquist plot of open loop transfer function PC for phase-stable design.

modes.

1.7 PZT Active Suspension from Commercial Dual-Stage Hard Disk Drives

The PZT active suspension which is used for simulation verification of the proposed algorithms in this dissertation is described in this section. The dual-stage servo system in a commercial 3.5″ dual-stage HDD is shown in Figure 1.6. In order to improve the positioning accuracy of the read/write head in the presence of disturbances, the PZT active suspension is appended to the arm of the Voice Coil Motor (VCM) which functions as the primary actuator. The secondary control loop is a high-performing mechatronic system with a larger bandwidth than the VCM control loop, and is used for expanding the overall dual-stage servo bandwidth. However, the PZT active suspension is a lightweight and flexible structure with resonant modes at high frequencies, and can be regarded as a multibody system.

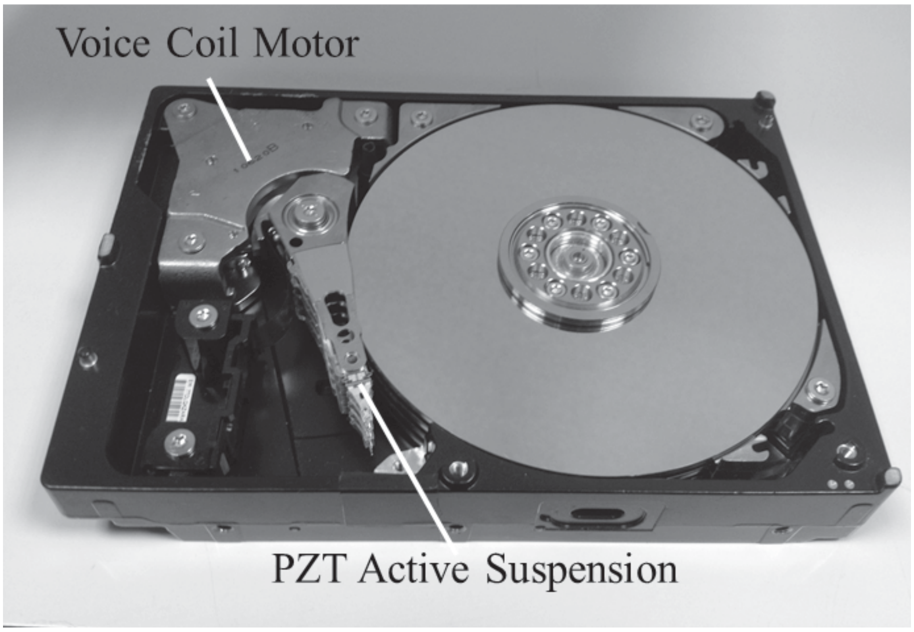

Figure 1.6: Internal structure of a dual-stage HDD.

A laser Doppler vibrometer is used for measuring the lateral displacement of the PZT active suspension. The simulations in this dissertation are performed by considering a closed-loop sampling frequency of $F_s = 40$ kHz. As such, the frequency response of the PZT active suspension is measured up to 20 kHz as shown in Figure 1.7. The measured frequency response is modeled using the modal summation form given as

$$P(s) = \sum_{i=1}^{M} \frac{R_i}{s^2 + 2\zeta_i\omega_i s + \omega_i^2}, \tag{1.10}$$

where M denotes the total number of resonant modes. R_i, ζ_i, and ω_i are the residue, damping ratio, and natural frequency of the i^{th} resonant mode, respectively. For frequencies smaller than 2 kHz, the PZT active suspension behaves like a pure gain. The primary resonant mode is at 4.70 kHz, and five resonant modes from 10 to 17 kHz are modeled as a single resonant mode for simplicity. Phase lag due to time delay is not modeled for simplicity, as well as the fact that integrated servo-mechanical design as depicted in Figure 1.4 results in the focus on shaping the resonant modes and anti-resonant zeros. From the frequency response of a fourth-order plant model for the PZT active suspension as shown in Figure 1.7, it can be seen that the main high-frequency resonant modes are at 4.70 kHz and 13.5 kHz. In this dissertation, the focus of the proposed algorithms is on the reshaping of the high-frequency resonant modes to satisfy performance and robust specifications.

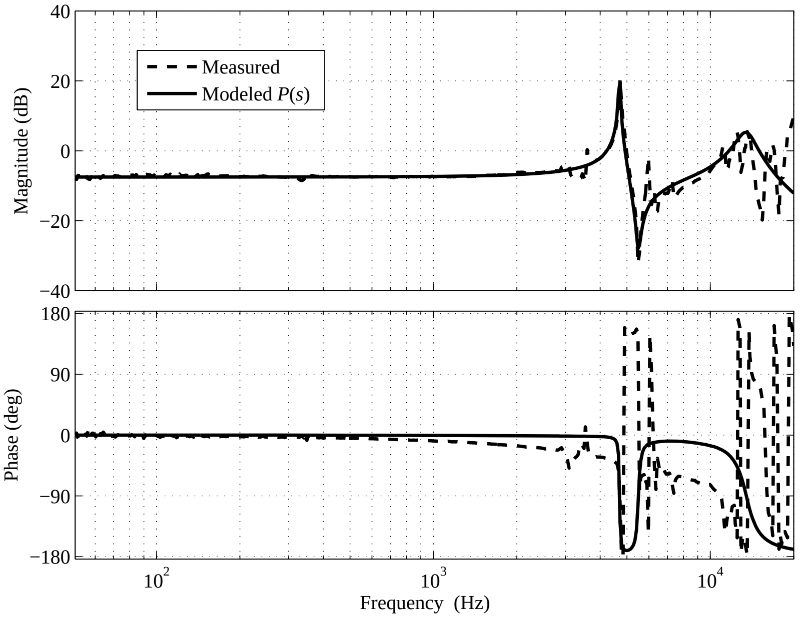

Figure 1.7: Measured and modeled frequency responses of PZT active suspension.

1.8 Motivation of Dissertation

The traditional silo approach towards R&D is insufficient for satisfying today's challenging demands of high-performance mechatronics [4]. For example, the achievable performance of the feedback control system may be limited by the resonant poles and unshifted resonant zeros of the mechanical plant as discussed in Section 1.2. Simultaneous phase-stabilization of resonant modes is easily carried out when the resonant modes at high frequencies are in-phase. Besides, control system design is simplified by mechanical plant properties such as controllability and dissipativity. Integrated servo-mechanical design can be used for overcoming the limitations as discussed in Sections 1.1 and 1.2.

The feedback control system is required to be robustly stable in the presence of plant parametric perturbations, and the tradeoff between performance and robust stability in control system design is well known. Probabilistic and randomized methods have been applied to controller design recently as discussed in Section 1.1. Deterministic uncertainties are considered by the integrated servo-mechanical design approaches in Section 1.3, and the worst case approach for considering uncertainties may be too conservative. In the context of mass production of high quality and low cost mechatronic products, more challenging performance specifications can be satisfied by considering the desired defect tolerance level using a chance-constrained robust stability criterion.

In the mechanical structure design stage of the R&D cycle, the Finite Element Analysis (FEA) model is often correlated with the frequency response function. For servo system analysis, the advantages of carrying out controller design in frequency domain are well known. Bandwidths and stability margins are frequency domain specifications, and disturbance attenuation capabilities are easily analyzed in the frequency domain using the sensitivity transfer function. Besides, well-established graphical tools such as the Nyquist plot can be utilized. As such, technical communication between mechanical and servo engineers can be improved, and many existing methods for servo system analysis can be employed by carrying out integrated servo-mechanical design in the frequency domain.

1.9 Contributions and Organization

This dissertation concentrates on the development of integrated servo-mechanical design algorithms for LTI systems with a Single-Input-Single-Output (SISO) mechanical plant to satisfy performance specifications and chance-constrained robust stability criterion. As digital controllers are commonly used in mechatronics, the algorithm is carried out in discrete-time. The proposed algorithms are applied to finite frequency redesign of the PZT active suspension from a commercial 3.5" dual-stage HDD at high frequencies, and can be applied to the redesign of any mechatronic systems with a SISO mechanical plant.

The original contributions of this dissertation are as follow:

1. Proposes a GKYP Lemma-based algorithm for satisfying performance specifications by redesigning the high-frequency response of a mechanical plant based on a low-order controller.

2. Formulates a convex separable parametrization for finite frequency reshaping of both mechanical plant and low-order controller. Using the GKYP Lemma and an approximation [47] based on the Conditional-

Value-at-Risk (CVaR) measure, the performance specifications and chance-constrained robust stability criterion are formulated as several convex constraints. The robust stability criterion is based entirely on the low-order moments and support of the plant parameter distributions.

3. Develops a Nyquist plot-based approach for reshaping the response of the mechanical plant at high frequencies based on a low-order controller to satisfy performance specifications and chance-constrained robust stability criterion. The robust stability criterion is formulated using the mean and variance of the plant parameter distributions. Based on the performance and robust stability specifications, allowable regions for the Nyquist plot of the open loop transfer function are derived.

The rest of the dissertation is organized as follows:

- Chapter 2 details the design algorithm for reshaping the response of the mechanical plant at high frequencies based on a low-order controller. The conversion of performance specifications into LMI constraints is shown.

- Chapter 3 illustrates the convex separable parametrization for reshaping the responses of both mechanical plant and low-order controller at high frequencies. The translation of performance specifications and chance-constrained robust stability criterion into several LMIs and linear inequalities is detailed. Comparative investigations are also carried out, where alternative numerical methods for integrated servo-mechanical design of robust mechatronics are considered.

- Chapter 4 explores the use of Nyquist plane for reshaping the high-frequency response of the mechanical plant based on a low-order controller. Considering performance and chance-constrained robust stability specifications, the derivation of allowable regions for the Nyquist plot of the open loop transfer function is shown. Comparison with other graphical approaches for robust feedback control system design is also carried out.
- Chapter 5 summarizes the findings and results of this dissertation, and presents some possible future research directions.

Chapter 2

Integrated Servo-Mechanical Design of High-Performance Mechatronics Using Generalized KYP Lemma

High-performance mechatronics have specifications which are difficult to satisfy when the mechanical plant is non-minimum phase and a low-order controller is used. In this chapter, an integrated servo-mechanical design algorithm is proposed for systematic finite frequency reshaping of a mechanical plant using the Generalized Kalman-Yakubovich-Popov (GKYP) Lemma. The synthesis of a minimum phase plant is carried out based on a low-order controller, as well as performance and positive realness specifications of the overall control system. Simulation results using the proposed algorithm achieve a high bandwidth control system with disturbance attenuation capabilities at the phase-stabilized resonant modes of the plant.

2.1 Background

Integrated servo-mechanical design is commonly solved using Linear Matrix Inequality (LMI)-based approaches as discussed in Chapter 1. The proposed LMI-based methods [25–27, 32] are usually iterative in nature. Simultaneous damping variable and control design for collocated structural systems is formulated as a non-iterative LMI optimization problem in [35]. In [38–40], the sensor or actuator placement problem was solved by designing the mechanical plant using the GKYP Lemma to have certain finite frequency positive realness and high gain properties.

In this chapter, we propose an integrated servo-mechanical design algorithm for synthesizing a minimum phase feedback control system which satisfies the frequency-domain performance specifications. The proposed algorithm for finite frequency reshaping of a mechanical plant considering a low-order controller is based on the GKYP Lemma and is non-iterative. Apart from the resonant frequencies, the characteristics of the resonant poles and anti-resonant zeros of the mechanical plant can be altered by the proposed algorithm to satisfy the magnitude and phase constraints imposed on the closed-loop frequency responses.

2.2 Youla Parametrization

The Youla parametrization approach is reviewed in this section, as the design variables for finite frequency reshaping of the mechanical plant are introduced using Youla parametrization in this chapter.

In Figure 2.1, a baseline controller C is designed based on the mechanical plant P in order to stabilize the feedback control system. The signals r, u, y, and w are as defined in Figure 1.2. The design variables for optimizing the controller are introduced by $Q \in \mathcal{RH}_\infty$ using the Youla parametrization approach, which is a well-known technique for designing optimal controllers to satisfy performance and robust specifications. The methods of Linear Quadratic Estimator (LQE) design and Linear Quadratic Regulator (LQR) design are commonly used for designing the baseline controller, and a simple choice for Q is the Finite Impulse Response (FIR) filter [15, 48].

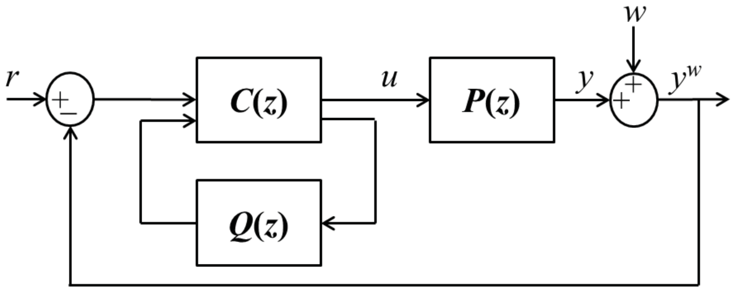

Figure 2.1: Controller optimization using Youla parametrization.

2.3 GKYP Lemma-Based Integrated Servo-Mechanical Design

The proposed algorithm for high-frequency reshaping of a mechanical plant based on a low-order controller considering performance and positive realness specifications is detailed in this section.

The application of the Youla parametrization approach to the synthesis of a new mechanical plant P_D is shown in Figure 2.2. It is worth noting that mechanical realization of P_D results in the ability to improve tracking accuracy by overcoming the limitation of unshifted zeros as mentioned in

Section 1.2. The signals r, u, y, and w represent reference input, control input to P_D, measurement output from P_D, and output disturbance, respectively. The low-frequency response of the original mechanical plant P will be retained in P_D, as the focus is on reshaping the high-frequency response. As such, C in Figure 2.2 is a low-order controller for compensating the low-frequency characteristics of P. The low-order plant P_N is subsequently designed based on C using LQE and LQR methods, which is akin to the design of a baseline controller prior to controller optimization as shown in Figure 2.1.

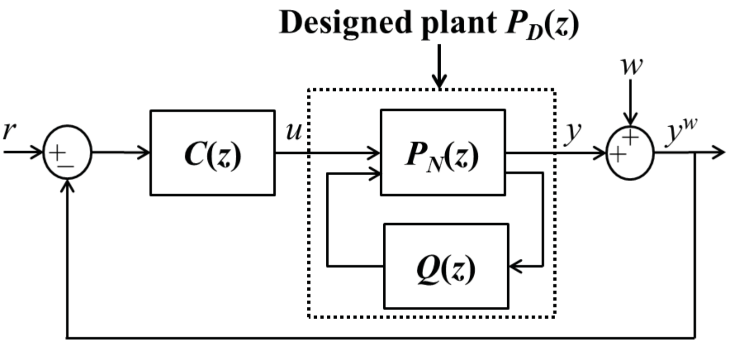

Figure 2.2: Mechanical plant redesign using Youla parametrization.

The details of P_N are depicted in Figure 2.3, where $\hat{C}$ is an observer of C. According to Figures 2.2 and 2.3, the state-space representation from y to u is given by

$$\begin{aligned} x_{t+1} &= A_c x_t - B_c y_t, \\ u_t &= C_c x_t - D_c y_t, \end{aligned} \tag{2.1}$$

where (A_c, B_c, C_c, D_c) are state-space matrices of C, and x_t denotes the

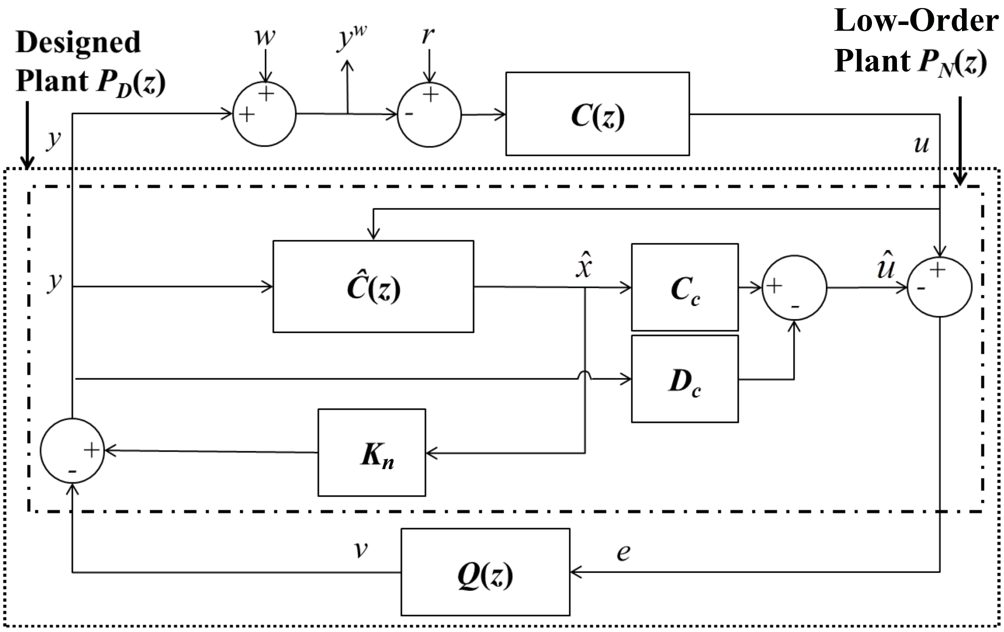

Figure 2.3: Detailed block diagram for the design of mechanical plant P_D.

value of x at discrete-time sample t. As such, $\hat{C}$ is given by

$$\hat{x}_{t+1} = A_c\hat{x}_t - B_c y_t + L_n(u_t - \hat{u}_t), \tag{2.2}$$

where

$$\hat{u}_t = C_c\hat{x}_t - D_c y_t, \tag{2.3}$$

$$y_t = K_n\hat{x}_t - v_t. \tag{2.4}$$

In (2.2) and (2.4), L_n and K_n denote the observer and feedback gain matrices, respectively. To carry out Youla parametrization, v is introduced in (2.4), and e is given by

$$e_t = u_t - \hat{u}_t. \tag{2.5}$$

The interconnections between the blocks $\hat{C}(z)$, C_c, D_c, and K_n are graphical representations of (2.2–2.5).

The design variables for shaping the high-frequency response of P_D enter affinely in the zero polynomial of FIR filter $Q \in \mathcal{RH}_\infty$, and will be solved subject to performance and positive realness constraints.

2.3.1 Performance and Positive Realness Specifications

From Figure 2.3, the sensitivity transfer function S is denoted by the closed-loop from w to y^w, and the complementary sensitivity transfer function T is denoted by the closed-loop from r to y.

Using the proposed integrated servo-mechanical design algorithm, the resonant poles of P_D are shaped based on finite frequency constraints imposed on S. A performance specification is formulated as

$$\|S(\bar{\theta})\|_\infty < \phi, \tag{2.6}$$

where $\phi \in \mathbb{R}^+$ is given, and $\bar{\theta}$ is a finite frequency range as defined in Section 1.5. This implies that the resonant poles of P_D have to be designed such that they are phase-stabilized by C.

The integrated servo-mechanical design algorithm ensures that there are no unstable anti-resonant zeros through restricting T to be positive real within a finite frequency range. This method is based on the fact that a discrete-time system with an equal number of inputs and outputs is minimum phase if it is positive real [49].

It is assumed that $P_D(z)$ is a strictly proper plant of relative degree one with no direct feedthrough. However, the relative degree of $P_D(s)$ is dependent on the sampling rate as documented in [50]. In the next section, the representation of performance specifications and positive realness constraints as LMIs using the GKYP Lemma will be detailed along with the presentation of the design steps.

2.3.2 Design Procedure

With reference to Figure 2.3, the steps for using the proposed integrated servo-mechanical design algorithm are

- **Step 1:** Design a low-order controller C of order n_c with state-space matrices denoted as (A_c, B_c, C_c, D_c) to compensate for the low-frequency response of the original plant P.

- **Step 2:** Compute observer gain matrix L_n and feedback gain matrix K_n based on (2.2–2.4) using the methods of LQE and LQR, respectively.

- **Step 3:** Formulate the equations given by

$$\begin{bmatrix} x_{t+1} \\ \hat{x}_{t+1} \end{bmatrix} = \begin{bmatrix} A_c & -B_cK_n \\ L_nC_c & A_E \end{bmatrix} \begin{bmatrix} x_t \\ \hat{x}_t \end{bmatrix} + \begin{bmatrix} -B_c & B_c & B_c \\ -L_nD_c & L_nD_c & B_c \end{bmatrix} \begin{bmatrix} w_t \\ r_t \\ v_t \end{bmatrix},$$

$$\begin{bmatrix} y_t^w \\ y_t \\ e_t \end{bmatrix} = \begin{bmatrix} 0 & K_n \\ 0 & K_n \\ C_c & -C_c \end{bmatrix} \begin{bmatrix} x_t \\ \hat{x}_t \end{bmatrix} + \begin{bmatrix} 1 & 0 & -1 \\ 0 & 0 & -1 \\ -D_c & D_c & 0 \end{bmatrix} \begin{bmatrix} w_t \\ r_t \\ v_t \end{bmatrix}, \tag{2.7}$$

  where $A_E := A_c - B_cK_n - L_nC_c$. The above state-space representation represents the block diagram in Figure 2.3 with Q excluded.

- **Step 4:** Specify Q as a FIR filter of order n_q. The transfer function of Q is given by

$$Q = \frac{q_{n_q}z^{n_q} + q_{n_q-1}z^{n_q-1} + \cdots + q_1z + q_0}{z^{n_q}}, \tag{2.8}$$

  where $q = \begin{bmatrix} q_{n_q} & q_{n_q-1} & \cdots & q_0 \end{bmatrix}$ is a vector of design variables. The state-space matrices of Q are

$$A_q = \begin{bmatrix} 0 & I_{n_q-1} \\ 0 & 0 \end{bmatrix}, B_q = \begin{bmatrix} 0 \\ 1 \end{bmatrix},$$
$$C_q = \begin{bmatrix} q_0 & q_1 & \cdots & q_{n_q-1} \end{bmatrix}, D_q = q_{n_q}. \tag{2.9}$$

  Set q_{n_q} to zero in order for P_D to have a relative degree of one, as most physical systems do not have direct feedthrough.

- **Step 5:** Let G_{y^ww} represent the closed-loop transfer function considering only input w and output y^w. The state-space matrices of $S = G_{y^w w} + G_{y^w v} Q G_{ew}$ are obtained using

$$A_S = \begin{bmatrix} A_{y^w w} & 0 & 0 \\ 0 & A_t & 0 \\ 0 & B_q C_t & A_q \end{bmatrix}, \; B_S = \begin{bmatrix} B_{y^w w} \\ B_t \\ B_q D_t \end{bmatrix},$$
$$C_S = \begin{bmatrix} C_{y^w w} & D_q C_t & C_q \end{bmatrix}, \; D_S = D_{y^w w} + D_q D_t, \tag{2.10}$$

where $(A_{y^w w}, B_{y^w w}, C_{y^w w}, D_{y^w w})$ and (A_t, B_t, C_t, D_t) are formulated using (2.7), and represent the minimal state-space realizations of $G_{y^w w}$ and $G_{y^w v} G_{ew}$, respectively. To achieve $\left\|S(\bar{\theta})\right\|_\infty < \phi$ using (1.6), the requirement of having the unknown design variables enter affinely in matrices C_S and D_S is fulfilled by choosing Q as a FIR filter. By relating (2.10) to (1.1), it can be further observed that the resonant poles of P_D are shaped through the design variables in matrices C_S and D_S to satisfy the constraints on S. For $T = G_{yr} + G_{yv} Q G_{er}$, the state-space matrices are given by

$$A_T = \begin{bmatrix} A_{yr} & 0 & 0 \\ 0 & A_{tT} & 0 \\ 0 & B_q C_{tT} & A_q \end{bmatrix}, \; B_T = \begin{bmatrix} B_{yr} \\ B_{tT} \\ B_q D_{tT} \end{bmatrix},$$
$$C_T = \begin{bmatrix} C_{yr} & D_q C_{tT} & C_q \end{bmatrix}, D_T = D_{yr} + D_q D_{tT}, \tag{2.11}$$

where $(A_{yr}, B_{yr}, C_{yr}, D_{yr})$ and $(A_{tT}, B_{tT}, C_{tT}, D_{tT})$ which are synthesized using (2.7) are the minimal state-space realizations of G_{yr} and $G_{yv} G_{er}$, respectively. Similarly, by relating (2.11) to (1.2), it can be seen that the anti-resonant zeros of P_D are shaped through the design variables in matrices C_T and D_T to satisfy the constraints on T.

- **Step 6:** Characterize the performance specifications as LMI constraints on S using (2.10) and (1.6), and remove the effects of unstable anti-resonant zeros by imposing constraints on T in the form of LMIs using (2.11) and (1.8).

- **Step 7:** Obtain the values of q and formulate the state-space matrices of the designed plant $P_D(z)$ given by

$$\begin{aligned} A_{PD} &= \begin{bmatrix} A_E + L_n D_c K_n & B_c C_q - L_n D_c C_q \\ B_q D_c K_n - B_q C_c & A_q - B_q D_c C_q \end{bmatrix}, \\ B_{PD} &= \begin{bmatrix} L_n^T \ {B_q}^T \end{bmatrix}^T, \ C_{PD} = \begin{bmatrix} K_n & -C_q \end{bmatrix}, \ D_{PD} = 0. \end{aligned} \tag{2.12}$$

The state-space matrices of the low-order plant P_N are given by

$$\begin{aligned} &A_{PN} = (A_E + L_n D_c K_n), B_{PN} = L_n, \\ &C_{PN} = K_n, D_{PN} = 0. \end{aligned} \tag{2.13}$$

The order of P_N denoted as n_n is equivalent to n_c, and the order of P_D is equivalent to $n_n + n_q$.

2.4 Simulation Example

The plant model $P(s)$ from Section 1.7 is discretized using a Zero-Order Hold (ZOH) considering F_s, and the frequency response of $P(z)$ is shown in Figure 2.4. In Step 1 of the algorithm, a discrete-time first-order lag compensator C is designed to result in an open loop PC with a 0 dB crossover frequency or open loop bandwidth of 1.80 kHz. The primary resonant frequency of P is 2.6 times greater than the open loop bandwidth as a result. This is a less conservative design compared to the rule of thumb which requires the primary resonant mode to be 3 to 4 times greater than the open loop bandwidth [20]. C is given by

$$C = \frac{0.9366z - 0.3287}{z - 0.9972}, \tag{2.14}$$

and $n_c = 1$. The frequency responses of C and PC are shown in Figure 2.4, and the state-space matrices of C is obtained as (A_c, B_c, C_c, D_c). The closed-loop is unstable due to the resonant mode at 4.70 kHz which is neither gain- nor phase-stabilized.

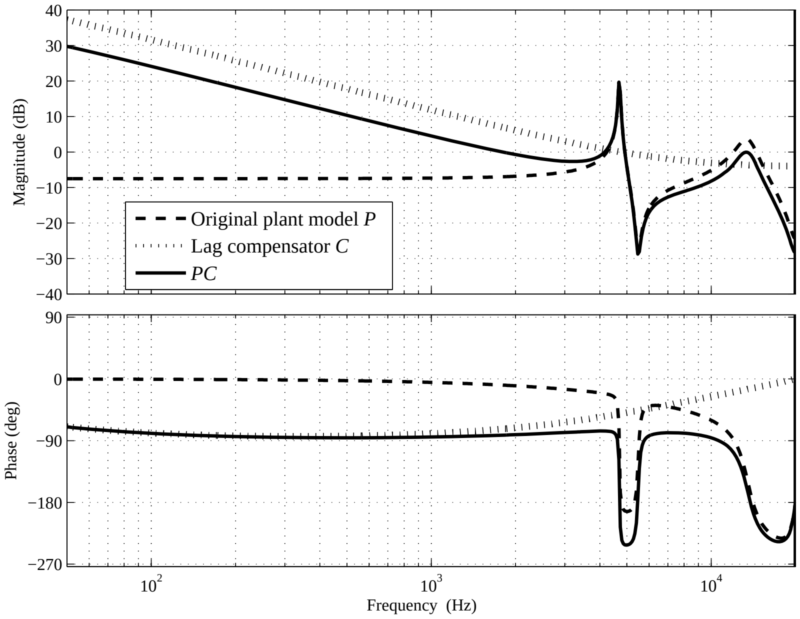

Figure 2.4: Frequency responses of original plant model P, lag compensator C, and open loop PC.

The weights for LQE design in Step 2 are given by $Q = 1$ and $R = 1$.

For the LQR design, the weights are given by $Q = C_c^T C_c$ and $R = 1$. L_n and K_n are obtained as 0.7382 and 0.4469, respectively. In Step 3, (2.7) is formulated using (A_c, B_c, C_c, D_c), L_n, and K_n. As the algorithm is used for shaping two high-frequency resonant modes in this case, the formulation of Q in Step 4 is carried out with $n_q = 4$. With (A_q, B_q, C_q, D_q), (2.10) and (2.11) are obtained in Step 5.

In Step 6, constraints are specified on S in the form of LMIs. The constraints are

a) $\left|S(\bar{\theta}_a)\right| < -20$ dB, $0.975 f_1\ (2\pi/F_s) \leq \bar{\theta}_a \leq 1.025 f_1\ (2\pi/F_s)$,

b) $\left|S(\bar{\theta}_b)\right| < -3.6$ dB, $0.975 f_2\ (2\pi/F_s) \leq \bar{\theta}_b \leq 1.025 f_2\ (2\pi/F_s)$,

c) $\left|S(\bar{\theta}_c)\right| < -1$ dB, $\bar{\theta}_c \leq 1.8$ kHz $(2\pi/F_s)$,

d) $\left|S(\bar{\theta}_d)\right| < \phi_d$, 9 kHz $(2\pi/F_s) \leq \bar{\theta}_d \leq 9.2$ kHz $(2\pi/F_s)$, and

e) $\left|S(\bar{\theta}_e)\right| < \phi_e$, 17.0 kHz $(2\pi/F_s) \leq \bar{\theta}_e \leq 20.0$ kHz $(2\pi/F_s)$,

where ϕ_d and ϕ_e are variables to be minimized. For Constraints (a–b), f_1 and f_2 are given by 4.70 kHz and 13.5 kHz, respectively.

Two phase-stabilized resonant modes will be created as a result of Constraints (a–b), and Non-Repeatable Run-Out (NRRO) induced by mechanical vibrations of the resonant modes will be attenuated by the overall control system. To have larger disturbance attenuation capabilities at the phase-stabilized resonant modes, the resonant peaks will be increased. The constraints imposed on $|S(f_a)|$ and $|S(f_b)|$ are based on the magnitude of P at 4.70 and 13.5 kHz, respectively. Frequency ranges f_a and f_b are chosen such that the resonant frequencies of P_D will be at around 4.70 kHz and 13.5 kHz, respectively.

Constraint (c) is used to ensure that the magnitudes of P_D and P are comparable at low frequencies, which will in turn result in comparable closed-loop bandwidths. When disturbance attenuation is achieved at certain frequencies, the sensitivity transfer function will be greater than 0 dB at other frequencies beyond the open loop bandwidth according to Discrete Bode's Integral Theorem (DBIT). This phenomenon is known as *spillover effects*. To reduce the spillover effects from disturbance attenuation at around 4.70 and 13.5 kHz, Constraints (d–e) are included.

After minimizing $\phi_4 + \phi_5$ subject to the LMI constraints, q is obtained in Step 7 as

$$q = \begin{bmatrix} 0 & -0.4259 & 0.3452 & -0.1783 & 0.7931 \end{bmatrix}. \tag{2.15}$$

The designed plant P_D and low-order plant P_N are obtained using (2.12) and (2.13), respectively. The order of P_N is given by $n_n = n_c = 1$, and the order of P_D is equivalent to $n_n + n_q = 5$ which is one order greater than the order of P. The order of P_D is increased in order for Constraints (a–b) to be satisfied. In general, the minimum value of n_q that is required will be equivalent to two times the number of resonant modes to be shaped. The choice of n_q is also dependent on the constraints specified and should be increased accordingly when required.

Based on the specified constraints, the sensitivity transfer function with C and P_D is shaped from the sensitivity transfer function with C and P_N as shown in Figure 2.5. From Figure 2.5, disturbance attenuation capabilities resulting from two phase-stabilized resonant modes can be seen. The frequency responses of P_D and P_N are shown in Figure 2.6, where it can be seen that the phase of P_D is smaller than $-180°$ for frequencies greater than 11.8 kHz as a result of unstable anti-resonant zero at 12.4 kHz. As such, the phase of the complementary sensitivity transfer function with C and P_D is smaller than $-180°$ for frequencies greater than 11.3 kHz as shown in Figure 2.7. As discussed in Section 1.2, unstable anti-resonant zeros result in lengthened settling time of time responses, lowered closed-loop bandwidth, and significant increase in magnitude of the sensitivity transfer function at frequencies beyond the open loop bandwidth, *etc.* The unstable anti-resonant zeros can be removed by an additional constraint given by

f) $\mathrm{Re}\left(T(\bar{\theta}_f)\right) > 0$ for 11.9 kHz $(2\pi/F_s) \leq \bar{\theta}_f \leq$ 12.9 kHz $(2\pi/F_s)$.

With Constraints (a–f), the minimum phase designed plant P_D^{MP} is obtained using

$$q = \begin{bmatrix} 0 & -0.5325 & 0.4857 & -0.2602 & 0.7740 \end{bmatrix}. \tag{2.16}$$

The order of P_D^{MP} is similarly equivalent to $n_n + n_q = 5$. In the next section, the simulation results are analyzed in detail.

2.5 Discussion of Results

The sensitivity transfer function with C and P_D^{MP} is shown in Figure 2.5. From Figure 2.5, it can be seen that spillover effects are reduced at frequencies between 6.60 kHz and 12.4 kHz when there are no unstable anti-resonant zeros. For frequencies greater than 14.6 kHz, spillover effects are increased. However, the net result is a reduction in overall spillover effects according to DBIT. The frequency responses of P_D^{MP} and the complemen-

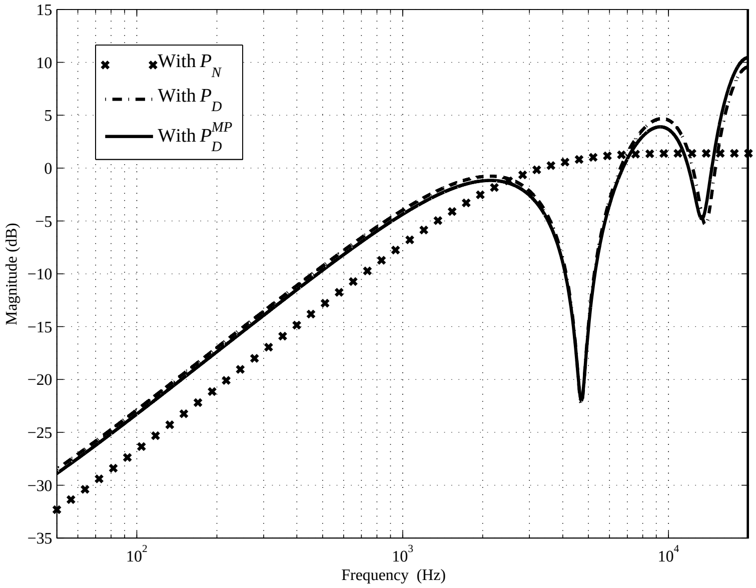

Figure 2.5: Frequency responses of sensitivity transfer functions.

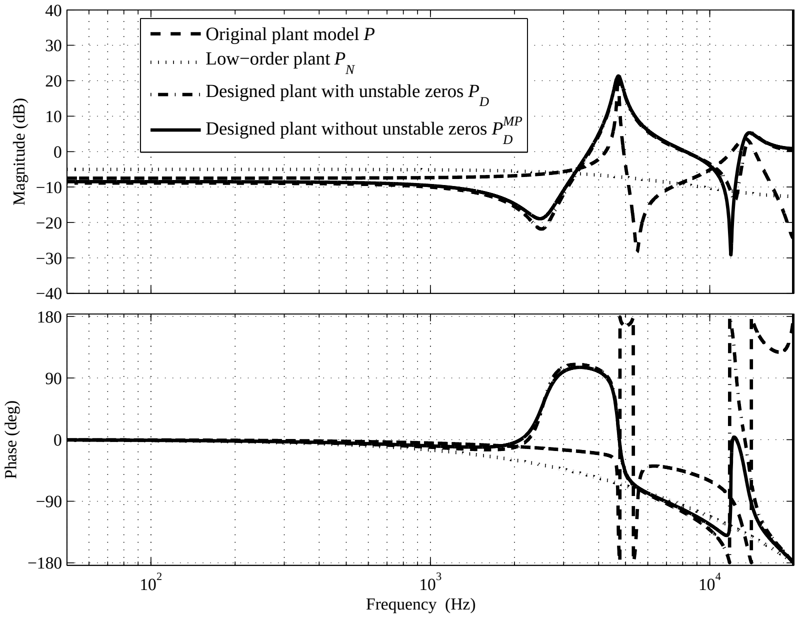

Figure 2.6: Frequency responses of original plant model P, and designed plants P_D and P_D^{MP}.

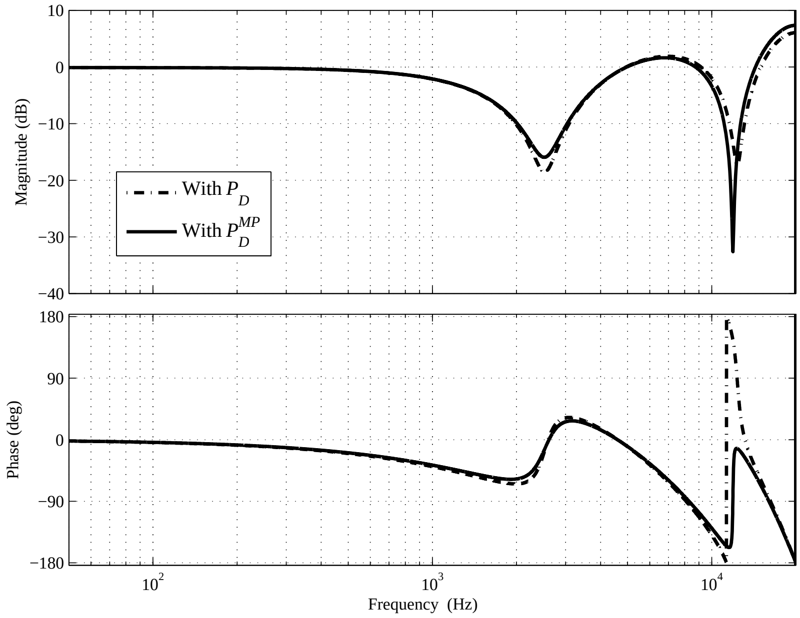

Figure 2.7: Frequency responses of complementary sensitivity transfer functions.

tary sensitivity transfer function are shown in Figures 2.6 and 2.7, respectively. From Figure 2.7, it can be seen that the phase of the complementary sensitivity transfer function is now greater than $-180°$ for frequencies up to the Nyquist frequency.

Although the closed-loop control system with the designed plants are stable, it can be seen from Figures 2.5 and 2.7 that the sensitivity and complementary sensitivity transfer functions are much greater than 0 dB near the Nyquist frequency. This is due to the shaping of the resonant mode at around 13.5 kHz which is in close proximity with the Nyquist frequency. It is worth noting that if the sampling frequency is increased to more than 100 kHz, the sensitivity and complementary sensitivity transfer functions will be smaller than 5 and -3 dB, respectively, when near the Nyquist frequency.

As a result of Constraint (c), the magnitudes of P_D and P_D^{MP} are comparable to the magnitude of P at low frequencies as shown in Figure 2.6. The resonant modes of P_D are at 4.71 and 13.8 kHz. For P_D^{MP}, the resonant modes are at 4.71 and 13.4 kHz.

P, P_D, and P_D^{MP} comprise of a rigid body mode of pure gain for frequencies less than 2 kHz, and flexible modes for frequencies greater than 2 kHz. However, for both P_D and P_D^{MP}, the rigid body mode is separated from the flexible modes by a stable anti-resonant zero at approximately 2.50 kHz. The stable anti-resonant zero provides the required phase lead for the phase-stabilization of the resonant mode at 4.71 kHz using C. An unstable anti-resonant zero at 12.4 kHz results in an out-of-phase resonant mode at 13.8 kHz for P_D. On the other hand, a stable anti-resonant zero at 11.9 kHz results in P_D^{MP} having an in-phase resonant mode at 13.4 kHz.

The frequency responses of the open loop transfer functions are shown in Figure 2.8, where it can be seen that the open loop bandwidth is reduced to approximately 1.20 kHz for both P_DC and $P_D^{MP}C$. This is due to the anti-resonant zero at around 2.50 kHz. However, the rule of thumb for the open loop bandwidth as mentioned in Section 2.4 remains satisfied.

The Nyquist plots of the open loop transfer functions are shown in Figure 2.9. The enlarged Nyquist plots are shown in Figure 2.10, where the dotted unit circle centered at the origin denotes the unit disc, and the bold dashed unit circle centered at $(-1 + j0)$ denotes the sensitivity disc as reviewed in Section 1.6. The dotted straight lines from the origin to the Nyquist curves in Figures 2.9 and 2.10 indicate the points which are furthest from the origin. These points correspond to the resonant peaks in the frequency responses of the open loop transfer functions. From Figures 2.9

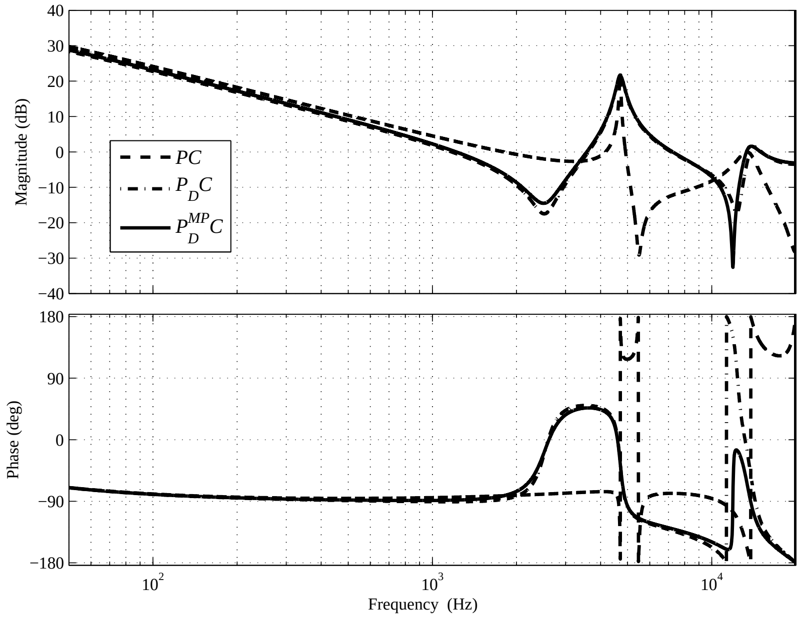

Figure 2.8: Frequency responses of open loop transfer functions.

and 2.10, it can be seen that while the resonant modes of P are not phase-stabilized by C, the resonant modes of P_D and P_D^{MP} are phase-stabilized by C even though P_D has an out-of-phase resonant mode. This is due to the fact that the resonant modes are not required to be in-phase in order for them to be phase-stabilized for satisfying the disturbance attenuation constraints on S. However, the trade-off is increased spillover effects as seen in Figure 2.5. From Figure 2.10, it can be seen that the increased spillover effects are due to the Nyquist curve of P_DC entering and remaining in the sensitivity disc over a wider range of frequency.

Although the five resonant modes which are in close proximity as shown in Figure 1.7 can be individually considered when specifying the constraints, the resonant modes will be shaped by the algorithm as a single resonant mode at around 13.5 kHz. The synthesis of distinct resonant modes is dependent on their proximity and damping ratios. As a rough

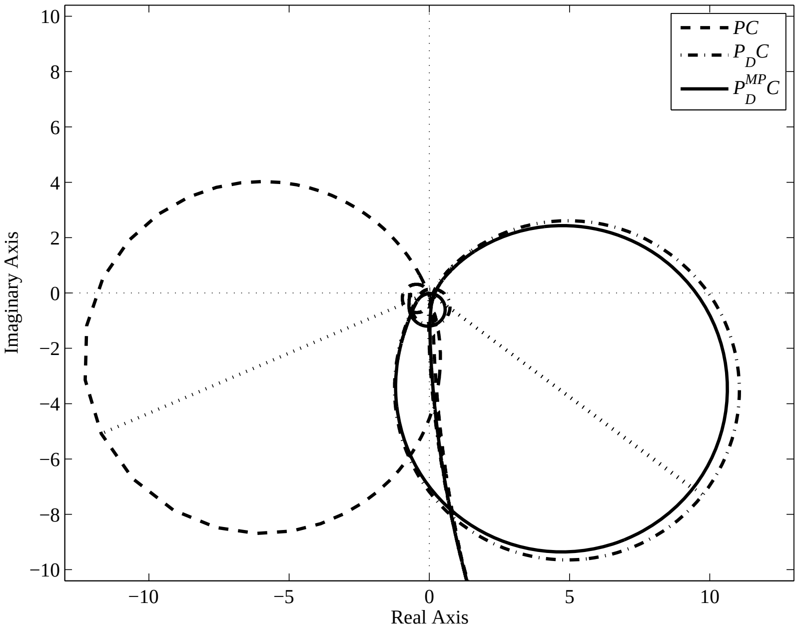

Figure 2.9: Nyquist plots of open loop transfer functions.

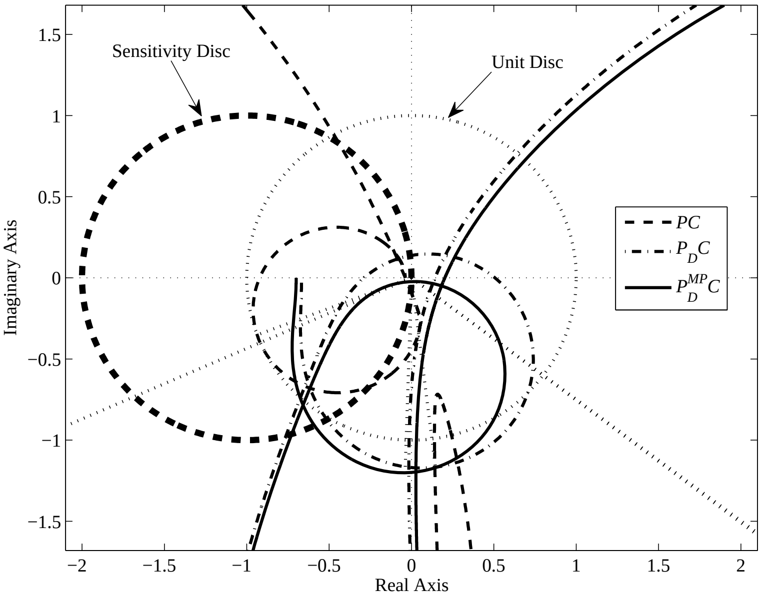

Figure 2.10: Enlarged Nyquist plots of open loop transfer functions.

guide, the resonant frequencies have to be at least 1.5 times apart for the synthesis of two distinct resonant modes with a small absolute difference in damping ratios.

Following the synthesis of the feedback control system in simulation, a continuous-time transfer function of the mechanical plant can be obtained by performing an inverse ZOH. The frequency response is related to mechanical design variables which are mass m, stiffness k, and damping coefficient B in order to mechanically realize the frequency response. This can be carried out by curve-fitting using (1.10), where $R_i = m_i^{-1}$, $\zeta_i = B_i(2\sqrt{m_i k_i})^{-1}$, and $\omega_i = \sqrt{k_i m_i^{-1}}$. It is worth noting that the curve-fitted solution $P_D(s)$ is non-unique. The mechanical design variables will be considered in the design of the mechanical structure using Computer-Aided Design (CAD) software, and the process iterates between CAD and Finite Element Analysis (FEA) till a close match between the FEA results and the frequency response $P_D(s)$ is obtained. A prototype is constructed based on the CAD design, and the measured frequency responses with the prototype and redesigned controller $C_D(z)$ should match closely the simulation results. The additional steps which are necessary for practical realization are summarized by the following block diagram.

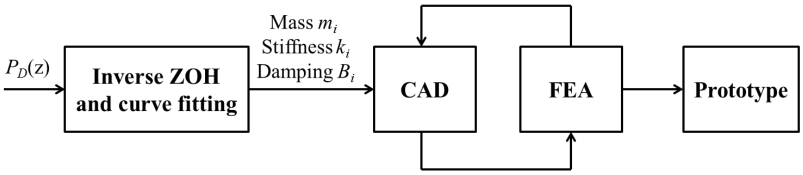

Figure 2.11: Summary of additional steps for practical realization.

It is worth noting that redesigning the mechanical plant based on a low-order controller to satisfy control specifications is in line with the perspective of integrated servo-mechanical design. This is due to the fact that the values of m, k, and B for mechanical realization are based on control specifications in addition to satisfying mechanical objectives. In addition, constraints can be placed on the plant parameters during the design phase in order to ensure physical realizability of the plant design.

2.6 Summary

In this chapter, an integrated servo-mechanical design is used for the synthesis of a minimum phase feedback control system which satisfies the performance and positive realness specifications. A GKYP Lemma-based integrated servo-mechanical design algorithm is proposed for systematic finite frequency reshaping of a mechanical plant based on a low-order controller. Simulation results using the proposed algorithm show that a high-bandwidth control system with disturbance attenuation capabilities at the phase-stabilized resonant modes of the plant is achieved.

In the next chapter, we consider the redesign of both mechanical plant and controller to satisfy performance specifications and chance-constrained robust stability criterion. A convex separable parametrization will be proposed, and the robust stability criterion will be formulated based on low-order moments and support.

Chapter 3

Integrated Servo-Mechanical Design of Robust Mechatronics Based on Ambiguous Chance Constraint

Simultaneous redesign of mechanical plant and controller to satisfy performance specifications and robust stability criterion is generally a nonlinear and nonconvex optimization problem. In this chapter, a convex separable parametrization for simultaneous finite frequency reshaping of both mechanical plant and a low-order controller taking into account an individual chance-constrained robust stability criterion is provided. Using the Generalized Kalman-Yakubovich-Popov (GKYP) Lemma and considering low-order moments and support, the robust stability criterion is formulated as several convex constraints. Simulations results show that when distributional changes in plant parameters occur under moderate violation of the mean and variance assumptions during the design phase, the specified $1-\epsilon$ remains satisfied.

3.1 Background

In the servo system analysis stage, $\mathcal{H}_\infty$ loop-shaping and μ-synthesis [15] are well-known methods for robust feedback controller design considering the worst-case scenario. Robust fixed-order controller design considering deterministic polytopic uncertainties is a worst-case approach as well. Examples include the generalized Kharitonov's Theorem [51] and convex parametrizations considering $\mathcal{H}_\infty/\mathcal{H}_2$ constraints [52, 53]. Given all statistical moments of the parametric perturbations, the desired defect tolerance level can be satisfied using probabilistic and randomized methods [17, 54–57] which will result in a controller that improves closed-loop performance. The assumption on the statistical moments can be relaxed by considering a truncated uniform distribution as the worst-case scenario [58, 59]. For ambiguous chance-constrained problems where only a few statistical moments are known, robust optimization algorithms are proposed [47, 60–62]. By solely designing a controller based on the mechanical plant design, the feedback control system may have limited achievable performance and robust stability as discussed in Chapter 1.

The simultaneous redesign of both mechanical plant and controller for satisfying performance and robust stability specifications is a nonlinear and nonconvex optimization problem, and various methods have been proposed for deriving a convex approximation as discussed in Chapters 1 and 2. Deterministic uncertainties are considered by the integrated servo-mechanical design approaches in [25, 27, 37, 40].

Furthering the redesign of a mechanical plant considered in Chapter 2, a convex separable parametrization is proposed for simultaneous finite frequency reshaping of *both* mechanical plant and a low-order controller to satisfy performance specifications and an ambiguous *chance-constrained* robust stability criterion. In order for the design variables to be solved simultaneously and efficiently, the robust stability criterion which is based on low-order moments and support is approximated [47, 62] using the Conditional-Value-at-Risk (CVaR) measure. The algorithm is compared with alternative methods for considering uncertainties in integrated servo-mechanical design. The Kharitonov's theorem and $\mathcal{H}_\infty$ loop-shaping approaches are considered under deterministic assessment. Under probabilistic assessment, distribution-free and distribution-based randomized approaches, as well as the $\mathcal{H}_\infty$ probabilistic theory are considered.

3.2 Integrated Servo-Mechanical Design Based on Chance Constraints

Integrated servo-mechanical design is carried out in this chapter using the block diagram shown in Figure 3.1. The redesigned mechanical plant and controller are denoted as P_D and C_D, respectively. The signals r, u, y, and w are as defined in Chapter 2 for Figure 2.2. The transfer functions

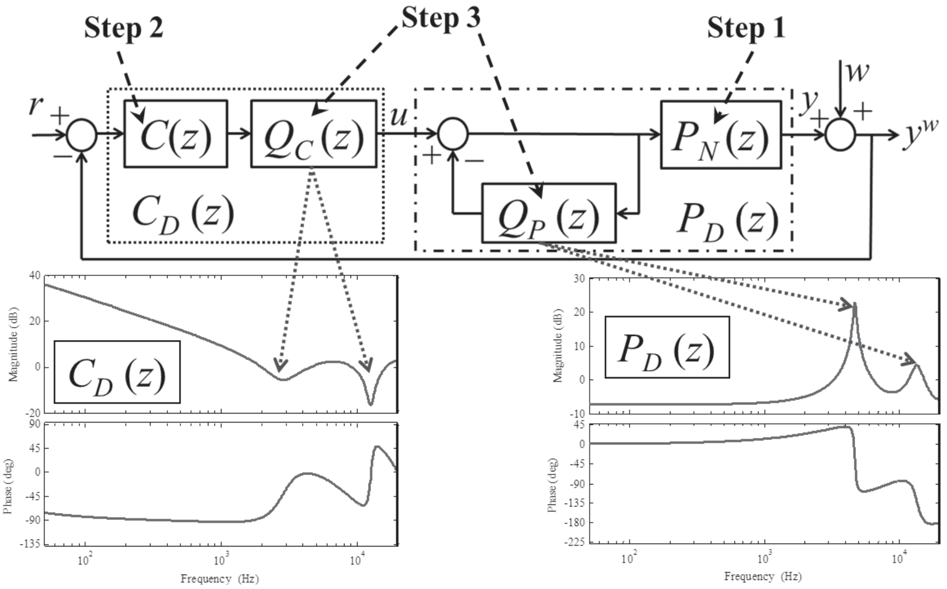

Figure 3.1: Block diagram for integrated servo-mechanical design.

of P_D and C_D are given by

$$\begin{aligned} P_D &= \frac{N_{PD}}{D_{PD}} \\ &= \frac{b_{n_p-\lambda}z^{n_p-\lambda} + \cdots + b_1 z + b_0}{z^{n_p} + a_{n_p-1}z^{n_p-1} + \cdots + a_1 z + a_0}, \qquad (3.1) \\ C_D &= \frac{N_{CD}}{D_{CD}}, \qquad (3.2) \end{aligned}$$

where n_p, λ, $b_{0,1,\cdots,n_p-\lambda}$, and $a_{0,1,\cdots,n_p-1}$ denote the order, relative degree, zero polynomial coefficients, and pole polynomial coefficients of P_D respectively. The low-frequency response of the open loop transfer function $P_D C_D$ is determined by low-order transfer functions P_N and C. In order to satisfy the performance and robust stability specifications, the resonant poles of P_D and anti-resonant zeros of C_D at high frequencies are shaped by design variables in Q_P and Q_C, respectively. Q_P and Q_C are given by

$$\begin{aligned} Q_P &= \frac{N_{QP}}{D_{QP}} = \frac{p_{n_{qp}-1} z^{n_{qp}-1} + \cdots + p_1 z + p_0}{(z+\alpha)^{n_{qp}}}, && (3.3) \\ Q_C &= \frac{N_{QC}}{D_{QC}} = \frac{c_{n_{qc}} z^{n_{qc}} + \cdots + c_1 z + c_0}{(z+\alpha)^{n_{qc}}}, && (3.4) \end{aligned}$$

where $z = -\alpha$ is specified as a high-frequency pole. The design variable vector is given by $q = [p_{n_{qp}-1} \cdots p_1 \, p_0 \, c_{n_{qc}} \cdots c_1 \, c_0]^T$ in this chapter. In (3.3), the order of Q_P is given by $n_{qp} = 2L$, where L denotes the number of high-frequency mechanical resonant modes for redesign. Let n_{cd} denote the desired order of C_D, and let n_c represent the order of C. The order of Q_C in (3.4) is given by $n_{qc} = n_{cd} - n_c$. The poles of Q_P and Q_C are chosen to be identical to result in stable pole-zero cancellations in the open loop transfer function $P_D C_D$. As such, the resonant poles and anti-resonant zeros of $P_D C_D$ at high frequencies are shaped by Q_P and Q_C, respectively. The design of P_N and C, and solving of q subject to performance and chance-constrained robust stability specifications will be provided along with the presentation of the design procedure in Section 3.3.

3.2.1 Performance Specifications

The performance specifications of the feedback control system are similarly characterized as finite frequency bounded realness constraints on the sensitivity transfer function S as shown by (2.6). Based on Figure 3.1 and (3.1–3.2), the closed-loop transfer function from w to y^w is given by

$$S = \frac{D_{PD} D_{CD}}{D_{PD} D_{CD} + N_{PD} N_{CD}}. \tag{3.5}$$

As a result of unknown design variables in the denominator polynomial of S, a sufficient condition given by [63]

$$\left\| \frac{D_{PD}D_{CD}}{\hat{D}} \right\|_{\infty} < (1-\varphi)\phi, \tag{3.6a}$$

$$\left\| 1 - \frac{D_{PD}D_{CD} + N_{PD}N_{CD}}{\hat{D}} \right\|_{\infty} < \varphi,\ \varphi \in (0,1), \tag{3.6b}$$

is formulated in order to use the GKYP Lemma for satisfying (2.6). $\hat{D}$ in (3.6) is specified as a reference characteristic polynomial for the redesigned feedback control system.

In retrospect, the redesigned mechanical plant as obtained in Step 7 of the design procedure in Chapter 2 can be equivalently represented as a transfer function given by

$$P_D = \frac{\bar{X} - \bar{M}Q}{\bar{Y} + \bar{N}Q}, \tag{3.7}$$

where $\bar{N}$, $\bar{M}$, $\bar{X}$, and $\bar{Y} \in \mathcal{RH}_{\infty}$ are specified as

$$\begin{aligned} &\bar{N} = G_{ew},\ \bar{M} = G_{y^w v}, \\ &\bar{X} = G_{yr}\bar{N}^{-1},\ \bar{Y} = G_{y^w w}\bar{M}^{-1}. \end{aligned} \tag{3.8}$$

Based on $\bar{N}\bar{X} + \bar{M}\bar{Y} \equiv 1$ and $C = \bar{N}\bar{M}^{-1}$, the sensitivity transfer function is given by

$$\begin{aligned} S &= (\bar{Y} + \bar{N}Q)\bar{M} \\ &= G_{y^w w} + G_{y^w v} Q G_{ew}. \end{aligned} \tag{3.9}$$

where it can be seen that the closed-loop characteristic polynomial of the designed feedback control system is restricted to be equivalent to the specified polynomial $\hat{D}$ derived from the denominator polynomials of $\bar{M}, \bar{Y}, \bar{N}$, and Q.

It is worth noting that in this chapter, the closed-loop characteristic polynomial is designed based on satisfying (3.6b) over finite frequency ranges and the robust stability criterion in the next section. As compared to the proposed method in Chapter 2 which restricts the closed-loop characteristic polynomial to be equivalent to the specified $\hat{D}$, the feedback control system can be designed to be stable for a larger proportion of perturbed plants.

3.2.2 Chance-Constrained Robust Stability Criterion

The robust stability criterion is formulated using the well-known positive realness approach [64] for ensuring stability of the closed-loop poles. An individual chance-constrained robust stability is formulated by specifying a single positive realness criterion to be satisfied with a probability of at least $1 - \epsilon$ under parametric perturbations, where $1 - \epsilon$ represents the desired probability tolerance for closed-loop stability. In fact, the robust stability criterion is an ambiguous chance constraint, where only the low-order moments and support of the parametric perturbations are known. From the perspective of satisfying a desired defect tolerance level in mass production, the feedback control system is required to be stable for at least a given $(1 - \epsilon) \times 100\%$ of the manufactured mechatronic products. It is worth nothing that as ϵ tends towards zero, the robust stability criterion tends towards the requirement of having stable feedback control systems for all manufactured mechatronic products under the worst-case scenario. The individual chance-constrained robust stability criterion is derived as follows.

The parametric perturbation of P_D by random variables $\mu_k + \tilde{\delta}_k$ is represented using multiplicative uncertainty, where μ_k is a given mean value, and $k = 1, 2, ..., K$. As a simple example, consider P_D with $n_p = 2$ and $\lambda = 1$. The perturbed plant $\tilde{P}_D$ is given by

$$\begin{aligned}\tilde{P}_D &= \frac{b_1(1+\mu_2+\tilde{\delta}_2)z + b_0 - b_1(\mu_2+\tilde{\delta}_2)}{z^2 + a_1(1+\mu_1+\tilde{\delta}_1)z + a_0 - a_1(\mu_1+\tilde{\delta}_1)} \\ &= \frac{b_1 z + b_0 + b_1(z-1)(\mu_2+\tilde{\delta}_2)}{z^2 + a_1 z + a_0 + a_1(z-1)(\mu_1+\tilde{\delta}_1)},\end{aligned} \tag{3.10}$$

where $-a_1(\mu_1+\tilde{\delta}_1)$ and $-b_1(\mu_2+\tilde{\delta}_2)$ are for ensuring that the DC gains of P_D and $\tilde{P}_D$ are identical. Based on the above formulation, $K = 2n_p - \lambda - 1$.

The closed-loop characteristic equation $\tilde{CE}$ considering $\tilde{P}_D$ and C_D is derived as

$$\begin{aligned}\tilde{CE} = &D_{CD}[D_{PD} + a_1(z-1)(\mu_1+\tilde{\delta}_1)] \\ &+ N_{CD}[N_{PD} + b_1(z-1)(\mu_2+\tilde{\delta}_2)].\end{aligned} \tag{3.11}$$

Let $F(z, \tilde{\delta}) = \tilde{CE}/CE$, where CE denotes the closed-loop characteristic polynomial without plant parametric perturbations. The roots of $\tilde{CE}$ will be stable for given $\mu + \tilde{\delta}$ if $\mathrm{Re}(F(\theta, \tilde{\delta})) > 0$ for all $\theta \in [0, \pi]$ [64]. Due to unknown design variables in CE, consider $\hat{F}(\theta, \tilde{\delta})$ derived as

$$\begin{aligned}&\hat{F}(\theta,\tilde{\delta}) = \hat{F}_0(\theta) + \hat{F}_1(\theta)\tilde{\delta}_1 + \hat{F}_2(\theta)\tilde{\delta}_2, \\ &\hat{F}_0 := \frac{D_{CD}[D_{PD}+a_1(z-1)\mu_1]+N_{CD}[N_{PD}+b_1(z-1)\mu_2]}{\hat{D}},\end{aligned}$$

$$\begin{aligned}\hat{F}_1 &:= \frac{D_{CD}}{\hat{D}} a_1(z-1),\\ \hat{F}_2 &:= \frac{N_{CD}}{\hat{D}} b_1(z-1),\end{aligned} \tag{3.12}$$

where $\hat{D}$ is as defined in (3.6). In general, $\hat{F}(\theta, \tilde{\delta})$ is obtained as

$$\begin{aligned}\hat{F}(\theta, \delta) &= \hat{F}_0(\theta) + \sum_{k=1}^{K} \hat{F}_k(\theta)\tilde{\delta}_k,\\ \hat{F}_0 &:= \Bigg[D_{CD}[D_{PD} + a_1(z-1)\mu_1 + \cdots + a_{n_p-1}(z^{n_p-1}-1)\mu_{n_p-1}].\\ &\quad + N_{CD}[N_{PD} + b_1(z-1)\mu_{n_p} + \cdots + b_{K-n_p+1}(z^{K-n_p+1}-1)\mu_K] \Bigg] \frac{1}{\hat{D}},\\ \hat{F}_k &:= \begin{cases} \frac{D_{CD}}{\hat{D}} a_k(z^k-1) \text{ for } k=1,2,...,n_p-1,\\ \frac{N_{CD}}{\hat{D}} b_{k-n_p+1}(z^{k-n_p+1}-1) \text{ for } k=n_p, n_p+1, ..., K.\end{cases}\end{aligned} \tag{3.13}$$

The following is the assumption on the low-order moments and support of $\tilde{\delta}$.

Assumption 3.1. *The elements of $\tilde{\delta}$ are stochastically independent and zero mean random variables. Let μ_{Ak} denote the mean value of $|\tilde{\delta}_k|$ for $k=1, 2, ..., K$, and let the support of $[\,|\tilde{\delta}_1|\ |\tilde{\delta}_2|\ \cdots\ |\tilde{\delta}_K|\,]^T$ be given by $[\underline{\delta}_A, \bar{\delta}_A]$, where $\underline{\delta}_A, \bar{\delta}_A \in [0, \infty)^K$. As such, $|\tilde{\delta}_k| - \mu_{Ak}$ are zero mean with finite positive definite covariance matrix $\mathbf{\Sigma}_A$ and support $\mathcal{W}_A = [\underline{\delta}_A - \mu_A, \bar{\delta}_A - \mu_A]$, where μ_A represents $[\mu_{A1}\ \mu_{A2} \cdots \mu_{AK}]^T$ and $-(\underline{\delta}_A - \mu_A), \bar{\delta}_A - \mu_A \in [0, \infty)^K$.*

The robust stability criterion is formulated as an individual chance-constrained problem given by

$$\text{Prob}\left(\text{Re}(\hat{F}(\theta, \tilde{\delta})) > 0\ \forall\ \theta \in [0, \pi]\right) \geq 1 - \epsilon, \tag{3.14}$$

where $\tilde{\delta}$ satisfies Assumption 3.1.

Consider $(A_{\hat{F}}, B_{\hat{F}}, C_{\hat{F}0}, D_{\hat{F}0})$ and $(A_{\hat{F}}, B_{\hat{F}}, C_{\hat{F}k}, D_{\hat{F}k})$ as the state-space representations of $\hat{F}_0$ and $\hat{F}_k$ in (3.13) for $k = 1, 2, ..., K$, respectively. The state-space realization of $\hat{F}(\theta, \tilde{\delta})$ is given by $(A_{\hat{F}}, B_{\hat{F}}, C_{\hat{F}}(\tilde{\delta}), D_{\hat{F}}(\tilde{\delta}))$, where matrices $C_{\hat{F}}$ and $D_{\hat{F}}$ are obtained as

$$C_{\hat{F}}=C_{\hat{F}0}+\sum_{k=1}^{K} C_{\hat{F}k}\tilde{\delta}_k,\ \ D_{\hat{F}}=D_{\hat{F}0}+\sum_{k=1}^{K} D_{\hat{F}k}\tilde{\delta}_k, \tag{3.15}$$

with $D_{\hat{F}0}=1$ and $D_{\hat{F}k}=0$ for $k = 1, 2, ..., K$. Using (1.8) with state-space matrices $(A_{\hat{F}}, B_{\hat{F}}, C_{\hat{F}}, D_{\hat{F}})$, (3.14) can be equivalently represented as an individual chance-constrained Linear Matrix Inequality (LMI) problem given by

$$\text{Prob}\left(\begin{bmatrix} A_{\hat{F}} & B_{\hat{F}} \\ I & 0 \end{bmatrix}^{*} \Pi \begin{bmatrix} A_{\hat{F}} & B_{\hat{F}} \\ I & 0 \end{bmatrix} + \Theta(\tilde{\delta}) < 0 \right) \geq 1-\epsilon. \tag{3.16}$$

In existing literature, (3.16) can be satisfied using distribution-based [17, 54–57, 65] and distribution-free randomized methods [58, 59]. We use the CVaR approximation as it allows the plant and controller design variables to be solved simultaneously and efficiently to satisfy both performance and robust stability criterion. Besides, the designed feedback control system will be robustly stable when distributional changes in plant parameters occur under the assumed mean, variance, and support.

3.2.3 CVaR Approximation of Robust Stability Criterion

The following theorem enables a chance-constrained LMI problem to be represented using several convex constraints under Assumption 3.1 and the CVaR measure.

Theorem 3.1. *The individual chance-constrained LMI specification given by (3.16) is satisfied if there exist* $q \in \mathbb{R}^{n_{qp}+n_{qc}+1}$, η_0^a, η_0^b, η_0^c, η_k, v_a, v_b, $v_c \in \mathbb{R}$, $k = 0, 1, \dots, K$, η^a, η^b, η^c, ξ_a, ξ_b, ι_a, $\iota_b \in \mathbb{R}^K$ *such that*

$$\mathrm{Re}\left(\hat{F}_0(\theta)\right) > \eta_0 \ \forall \ \theta \in [0, \pi], \tag{3.17a}$$

$$\mathrm{Re}\left(\hat{F}_k(\theta)\right) > -\eta_k \ \forall \ \theta \in [0, \pi], \ \ k = 1, 2, \dots, K, \tag{3.17b}$$

$$\mathrm{Re}\left(-\hat{F}_k(\theta)\right) > -\eta_k \ \forall \ \theta \in [0, \pi], \ \ k = 1, 2, \dots, K, \tag{3.17c}$$

$$v_a + v_b + v_c \leq 0, \tag{3.17d}$$

$$-\eta_0^a + (\eta^a)^T \mu_A + {\xi_a}^T \left(\bar{\delta}_A - \mu_A\right) + {\iota_a}^T \left|\underline{\delta}_A - \mu_A\right| \leq v_a, \tag{3.17e}$$

$$\xi_a - \iota_a = \eta^a, \ \ \xi_a, \iota_a \geq 0, \tag{3.17f}$$

$$-\eta_0^b + \left(\eta^b\right)^T \mu_A + \Upsilon {\xi_b}^T \left(\bar{\delta}_A - \mu_A\right) + \Upsilon {\iota_b}^T \left|\underline{\delta}_A - \mu_A\right| \leq v_b, \tag{3.17g}$$

$$\xi_b - \iota_b = -\eta^b, \ \ \xi_b, \iota_b \geq 0, \tag{3.17h}$$

$$-\eta_0^c + (\eta^c)^T \mu_A + \sqrt{\Upsilon} \left\| \sqrt{\mathbf{\Sigma_A}} \, (\eta^c) \right\|_2 \leq v_c, \tag{3.17i}$$

$$-\eta_0^a - \eta_0^b - \eta_0^c = -\eta_0, \tag{3.17j}$$

$$\eta^a + \eta^b + \eta^c = \eta, \ \ \eta := [\, \eta_1 \ \eta_2 \ \cdots \ \eta_K \,]^T \geq 0, \tag{3.17k}$$

where $\Upsilon := (1/\epsilon - 1)$, *and (3.17a–3.17c) are formulated using (1.8). In addition,* $\bar{\delta}_A$, $\underline{\delta}_A$, μ_A, *and* $\mathbf{\Sigma_A}$ *are as defined in Assumption 3.1.*

Remark 3.1. *In Theorem 3.1,* $1 - \epsilon$ *can be maximized by using a binary* *search algorithm [47].*

Remark 3.2. *The number of linear inequality constraints is constant, while the number of LMI constraints is linearly proportional to K. As such, computational complexity is significantly reduced as compared to randomized methods.*

The proof of Theorem 3.1 is as follows.

Proof. The proof for Theorem 3.1 is established based on Assumption 3.1 and the relationship between $\hat{F}(\theta, \tilde{\delta})$ and $\hat{F}_k(\theta)$ in (3.13) for $k = 0, 1, ..., K$. For simplicity, $\hat{F}(\theta, \tilde{\delta})$ and $\hat{F}_k(\theta)$ are represented using $\hat{F}$ and $\hat{F}_k$ in the proof from here onwards, respectively. As the denominators of $\hat{F}$ and $\hat{F}_k$ are identical for $k = 0, 1, ..., K$,

$$\mathrm{Re}(\hat{F}){=}\mathrm{Re}(\hat{F}_0){+}\sum_{k=1}^{K}\mathrm{Re}(\hat{F}_k\tilde{\delta}_k)\ \forall\ \theta{\in}[0,\pi]\,, \tag{3.18}$$

and $\mathrm{Re}(\hat{F}) > 0$ for all $\theta \in [0, \pi]$ is equivalent to

$$\mathrm{Re}(\hat{F}_0){+}\sum_{k=1}^{K}\mathrm{Re}(\hat{F}_k\tilde{\delta}_k){>}0\ \forall\ \theta{\in}[0,\pi]\,. \tag{3.19}$$

As a result, the individual chance-constrained problem given by (3.14) is equivalent to

$$\mathrm{Prob}\left(\mathrm{Re}(\hat{F}_0){+}\sum_{k=1}^{K}\mathrm{Re}(\hat{F}_k\tilde{\delta}_k){>}0\ \forall\ \theta{\in}[0,\pi]\right){\geq}1{-}\epsilon. \tag{3.20}$$

Due to $\hat{F}_0$, $\hat{F}_k$, and $-\hat{F}_k \in \mathcal{RH}_\infty$, the gains of the frequency responses of $\hat{F}_0$, $\hat{F}_k$, and $-\hat{F}_k$ are finite for all $\theta \in [0, \pi]$, where $k = 1, 2, ..., K$. As such, there exists a finite lower bound $\eta_0 \in \mathbb{R}$ on $\mathrm{Re}(\hat{F}_0)$ for all $\theta \in [0, \pi]$, and a finite lower bound $-\eta_k$ on both $\mathrm{Re}(\hat{F}_k)$ and $\mathrm{Re}(-\hat{F}_k)$ for all $\theta \in [0, \pi]$, where $\eta_k \geq 0$ for $k = 1, 2, ..., K$, resulting in the formulation of (3.17a–3.17c).

A finite lower bound on $\mathrm{Re}(\hat{F}_k\tilde{\delta}_k)$ for all $\theta \in [0, \pi]$ is derived as $-|\tilde{\delta}_k|\eta_k$, where $k = 1, 2, ..., K$. This is shown by the following relationships, where for $\tilde{\delta}_k > 0$ and $k = 1, 2, ..., K$,

$$\mathrm{Re}(\hat{F}_k\tilde{\delta}_k) = \tilde{\delta}_k \mathrm{Re}(\hat{F}_k) > -\tilde{\delta}_k\eta_k \ \forall \ \theta \in [0, \pi] \, , \tag{3.21}$$

and for $\tilde{\delta}_k < 0$ and $k = 1, 2, ..., K$,

$$\mathrm{Re}(\hat{F}_k\tilde{\delta}_k) = |\tilde{\delta}_k| \mathrm{Re}(-\hat{F}_k) > -|\tilde{\delta}_k|\eta_k \ \forall \ \theta \in [0, \pi] \, . \tag{3.22}$$

As a result, (3.20) is satisfied if

$$\mathrm{Prob}\left(\eta_0 - \textstyle\sum_{k=1}^{K} \eta_k |\tilde{\delta}_k| \geq 0\right) \geq 1 - \epsilon. \tag{3.23}$$

The chance-constrained linear inequality in (3.23) can be approximated as a second-order conic optimization problem under the CVaR measure [47] by equivalently representing (3.23) as

$$\mathrm{Prob}\left(\eta_0 - \eta^T \mu_A - \sum_{k=1}^{K} \eta_k \left(|\tilde{\delta}_k| - \mu_{Ak}\right) \geq 0\right) \geq 1 - \epsilon, \tag{3.24}$$

where $|\tilde{\delta}_k| - \mu_{Ak}$ satisfies Assumption 3.1. Using the second-order conic approximation, (3.24) is satisfied if the constraints in (3.17d–3.17k) are fulfilled based on the lower bounds η_0 and $-\eta_k$ obtained, where $k =$

$1, 2, ..., K$. $\square$

Remark 3.3. *Using (3.23), closed-loop stability under parametric perturbations is evaluated based on a lower bound on the positive realness measure in (3.20). As a result, the design problem can be solved efficiently using several convex constraints under the CVaR approximation.*

Remark 3.4. *CVaR approximation is the tightest convex approximation of the individual chance constraint given by (3.23) [62].*

3.3 Design Procedure

With reference to Figure 3.1, the proposed integrated servo-mechanical design algorithm is detailed as

- **Step 1:** Obtain the low-order plant given as

  $$P_N = \frac{N_{PN}}{D_{PN}}, \tag{3.25}$$

  by modeling the low-frequency response of the original plant P which is sampled with sampling frequency F_s. Let the order of P_N be denoted as n_n. In addition, the relative degrees of P_N and P_D are equivalent.

- **Step 2:** Design a low-order controller C of order n_c such that $P_N C$ achieves the desired low-frequency gain and open loop bandwidth. Let the transfer function of C be given by

  $$C = \frac{N_C}{D_C}. \tag{3.26}$$

- **Step 3:** Formulate Q_P and Q_C in Figure 3.1 using (3.3) and (3.4), respectively.

- **Step 4:** Let the reference closed-loop characteristic polynomial be given by

$$\hat{D} = (D_{PN}D_C + \bar{N}_{PN}N_C)(z+\alpha)^{(n_{qp}+n_{qc})}. \tag{3.27}$$

Obtain $(A_{S1}, B_{S1}, C_{S1}, D_{S1})$ as the state-space matrices of

$$S_1 := \frac{D_{PN}D_C D_{QC}(D_{QP}+N_{QP})}{\hat{D}}. \tag{3.28}$$

Derive $(A_{S2}, B_{S2}, C_{S2}, D_{S2})$ as the state-space matrices of

$$\begin{aligned} &S_2 := 1 - \frac{N_{S2}}{\hat{D}}, \\ &N_{S2} := D_{PN}D_C D_{QC}(D_{QP}+N_{QP}) + \bar{N}_{PN}N_C N_{QC} D_{QP}, \end{aligned} \tag{3.29}$$

where $\bar{N}_{PN} := k_N N_{PN}$. The value of k_N is given by

$$k_N = \left.\frac{N_{PN}(z)N_C(z) + D_{PN}(z)D_C(z) - D_{PN}(z)D_C(z)(z+\alpha)^{n_{qp}+n_{qc}}}{N_{PN}(z)N_C(z)(z+\alpha)^{n_{qp}+n_{qc}}}\right|_{z=1}, \tag{3.30}$$

and is used for ensuring that the DC gains of $\hat{D}$ and $(D_{PN}D_C + N_{PN}N_C)$ are identical in order for the low-frequency gains of $P_D C$ and $P_N C$ to be approximately identical.

Specify a finite frequency performance specification $\|S(\bar{\theta})\|_\infty < \phi$ as

$$\|S_1(\bar{\theta})\|_\infty < (1-\varphi)\phi, \tag{3.31a}$$

$$\|S_2(\bar{\theta})\|_\infty < \varphi,\ \varphi \in (0,1), \tag{3.31b}$$

and represent the constraints as LMIs using the GKYP Lemma.

- **Step 5:** To ensure that the poles of P_D are stable, restrict S_1 to be positive real around the resonant frequencies by specifying $\mathrm{Re}(S_1(\bar{\theta})) > 0$ using (1.8). Specify $\mathrm{Re}(Q_c(\bar{\theta})) > 0$ using (1.8) to remove unstable zeros in C_D.

- **Step 6:** Using (3.13) and (3.15), the state-space representations of $\hat{F}_0$ and $\hat{F}_k$ are derived as $(A_{\hat{F}}, B_{\hat{F}}, C_{\hat{F}0}, D_{\hat{F}0})$ and $(A_{\hat{F}}, B_{\hat{F}}, C_{\hat{F}k}, D_{\hat{F}k})$ for $k = 1, 2, ..., K$, respectively. In addition, $A_{\hat{F}} = A_{S1} = A_{S2}$ and $B_{\hat{F}} = B_{S1} = B_{S2}$. Formulate the robust stability criterion in (3.14) as several convex constraints using Theorem 3.1.

- **Step 7:** Obtain the values of q, and synthesize P_D and C_D using

$$P_D = \frac{N_{PD}}{D_{PD}} = k_P \frac{\bar{N}_{PN}}{D_{PN}} \frac{D_{QP}}{D_{QP} + N_{QP}}, \tag{3.32}$$

$$C_D = \frac{N_{CD}}{D_{CD}} = \frac{1}{k_P} \frac{N_C}{D_C} \frac{N_{QC}}{D_{QC}}, \tag{3.33}$$

where k_P in (3.32) and (3.33) is a constant gain for ensuring identical low-frequency gains between P_D and P. The order of P_D is given by $n_p = n_n + n_{qp}$.

3.4 Simulation Example

Based on Step 1 of the design algorithm, P_N is obtained as

$$P_N = \frac{N_{PN}}{D_{PN}} = \frac{0.3817}{z+\alpha}, \tag{3.34}$$

where $\alpha = -0.09478$ results in a stable pole at 15 kHz which is greater than the resonant frequencies of $P(z)$. The frequency response of P_N is shown in Figure 3.2. A first-order lag compensator C is designed as

$$C = \frac{N_C}{D_C} = \frac{0.6079z - 0.1264}{z - 0.9979} \tag{3.35}$$

in Step 2 in order for $P_N C$ to have an open loop bandwidth of 1.35 kHz. The frequency responses of C and $P_N C$ are shown in Figure 3.3.

In order to redesign $L = 2$ resonant modes at 4.70 kHz and 13.5 kHz to be phase-stabilized by C_D, Q_P and Q_C are specified in Step 3 using $n_{qp} = 4$, $n_{qc} = 4$, and $\alpha = -0.09478$. The required state-space matrices in Steps 4–5 are formulated with $k_N = 2.2307$ and $\alpha = -0.09478$, and the performance specifications are

a) $\left|S_1(\bar{\theta}_a)\right| < (1-\varphi_1)10^{(-l_1/20)}$, $0.975 f_1\ (2\pi/F_s) \le \bar{\theta}_a \le 1.025 f_1\ (2\pi/F_s)$,

b) $\left|S_2(\bar{\theta}_a)\right| < \varphi_1$,

c) $\left|S_1(\bar{\theta}_c)\right| < (1-\varphi_2)10^{(-l_2/20)}$, $0.975 f_2\ (2\pi/F_s) \le \bar{\theta}_c \le 1.025 f_2\ (2\pi/F_s)$,

d) $\left|S_2(\bar{\theta}_c)\right| < \varphi_2$,

e) $\left|S_1(\bar{\theta}_e)\right| < (1-\varphi_3)10^{(-15/20)}$, $0.05\ \text{kHz}\ (2\pi/F_s) \le \bar{\theta}_e \le 0.2\ \text{kHz}\ (2\pi/F_s)$,

f) $\left|S_2(\bar{\theta}_e)\right| < \varphi_3$,

g) $\left|S_1(\bar{\theta}_g)\right| < (1-\varphi_4)10^{(10/20)}$, 1.35 kHz $(2\pi/F_s) \le \bar{\theta}_g \le$ 20 kHz $(2\pi/F_s)$,

h) $\left|S_2(\bar{\theta}_g)\right| < \varphi_4$,

i) $\mathrm{Re}\left(S_1(\bar{\theta}_a)\right) > 0$,

j) $\mathrm{Re}\left(S_1(\bar{\theta}_c)\right) > 0$, and

k) $\mathrm{Re}\left(T_1(\bar{\theta}_k)\right) > 0$, 10 kHz $(2\pi/F_s) \le \bar{\theta}_k \le 0.975 f_2$ $(2\pi/F_s)$.

For Constraints (a–d), l_1, f_1, l_2, and f_2 are given by 20 dB, 4.70 kHz, 1 dB, and 13.5 kHz, respectively. Gains l_1 and l_2 are chosen based on the magnitude of P at f_1 and f_2, respectively. Constraints (e–f) are specified to achieve an open loop bandwidth of approximately 1.35 kHz, and Constraints (g–h) are used for limiting the spillover effects from disturbance attenuation.

In Step 6, the robust stability criterion is formulated. As an example, the poles of P_D are perturbed under a constant low-frequency gain. The zeros are not perturbed due to their relatively small effects on closed-loop stability. As such, $K = 4$ and $\mu+\tilde{\delta}=[\mu_1+\tilde{\delta}_1\ \mu_2+\tilde{\delta}_2\ \mu_3+\tilde{\delta}_3\ \mu_4+\tilde{\delta}_4]^T$. The following are the assumptions on the low-order moments and support to result in unstable primary and secondary resonant poles. μ is given by $[\,0.75\ 1\ {-0.5}\ {-0.2}\,]^T$, and the mean μ_{Ak}, variance, and support of $|\tilde{\delta}_k|$ are given by 0.0937, 0.00439, and $[0, 0.281]$ for $k = 1, 2$, respectively. For $k = 3, 4$ the mean μ_{Ak}, variance, and support are given by 9.37×10^{-3}, 4.39×10^{-5}, and $[0, 0.0281]$, respectively.

In Step 7, q which satisfies Constraints (a–k) and the convex constraints in Theorem 3.1 is obtained. In addition, $1-\epsilon$ is maximized as 0.3281. P_D

is obtained as

$$\begin{aligned} P_D &= k_P \frac{\bar{N}_{PN}}{z-0.09478} \frac{(z-0.09478)^4}{(z-0.09478)^4+N_{QP}} \\ &= k_P \frac{\bar{N}_{PN}(z-0.09478)^3}{(z-0.09478)^4+N_{QP}}, \end{aligned} \tag{3.36}$$

where N_{QP} is given by $N_{QP} = -0.2177z^3 + 0.3136z^2 - 0.1094z + 0.6132$, and $k_P = 0.8486$. The order of P_D is given by $n_n + n_{qp} = 5$. With a stable pole-zero cancellation at $z = 0.09478$, the order of P_D is equivalent to the order of P which is four. Compared to the order of P_D in Chapter 2, a fourth-order plant is obtained in this case as a result of simultaneous optimization of the low-order controller for satisfying Constraints (a–d). The fifth-order C_D is given by

$$C_D = \frac{1}{k_P} \frac{N_C}{D_C} \frac{N_{QC}}{(z-0.09478)^4}, \tag{3.37}$$

where N_{QC} is given by $N_{QC} = 1.4717z^4 - 1.4507z^3 + 0.8310z^2 - 1.4717z + 1.2083$.

3.4.1 Performance Analysis

The frequency responses of the redesigned plant P_D and controller C_D are shown in Figures 3.2 and 3.3, respectively. The frequency response of the open loop transfer function $P_D C_D$ is shown in Figure 3.3, where the bandwidth is slightly reduced to 1.16 kHz due to zeros at 2.56 kHz. The sensitivity transfer function S is shown in Figure 3.4, where it can be seen that disturbance is attenuated at 4.71 kHz and 13.6 kHz as a result of phase-stabilized resonant modes. The rough guide for the synthesis of two distinct resonant modes, and realization of the mechanical plant are as discussed in Chapter 2.

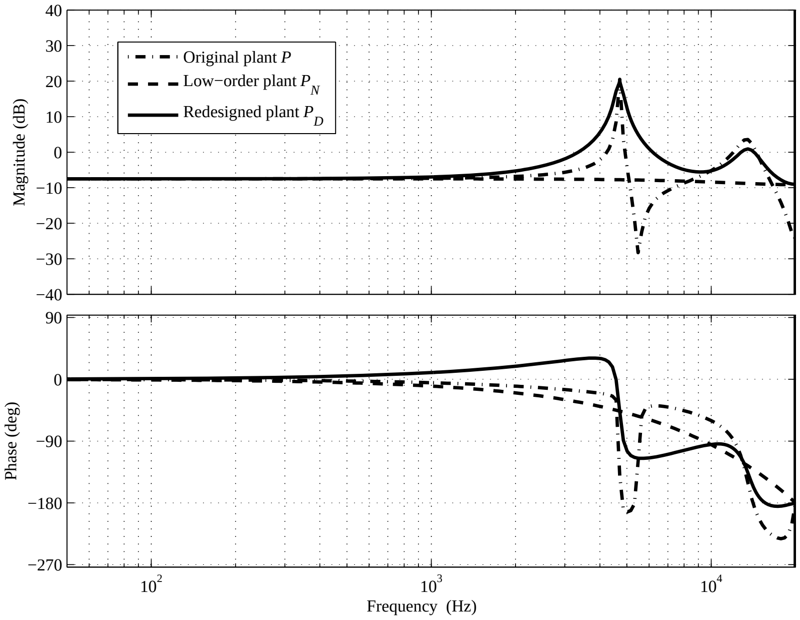

Figure 3.2: Frequency responses of original plant P, low-order plant P_N, and redesigned plant P_D.

3.4.2 Robustness Analysis

In order to demonstrate the robust stability of the designed feedback control system under distributional changes, triangle- and $\beta(0.15, 0.09)$-distributed plant parameters are considered. In this case, the mean and variance assumptions are violated by the $\beta(0.15, 0.09)$ distribution.

The low-order moments and support of the triangle distribution are as assumed in the design phase for $|\tilde{\delta}_k|$, where $k = 1, 2, 3, 4$. The values are tabulated under Case 2 of Tables 3.1 and 3.2. Compared to the triangle-distribution, the mean μ_{Ak} and variance of the $\beta(0.15, 0.09)$-distributed $|\tilde{\delta}_k|$ are greater than the assumed values in order for the support to remain

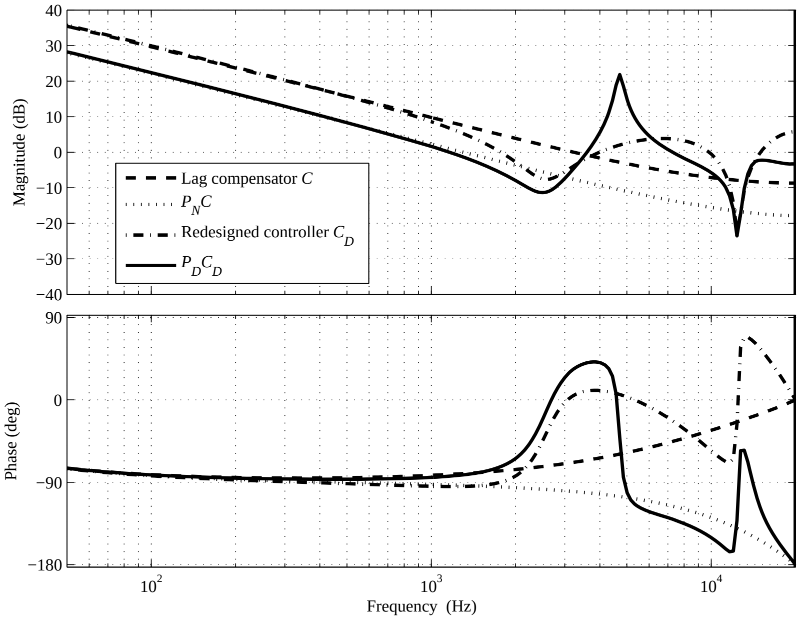

Figure 3.3: Frequency responses of lag compensator C, redesigned controller C_D, and open loop transfer functions.

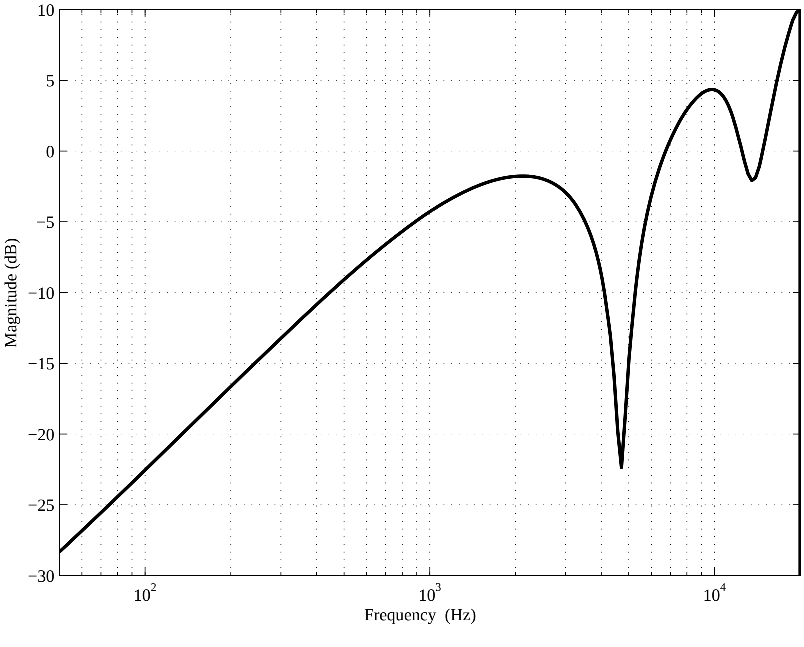

Figure 3.4: Frequency response of sensitivity transfer function S.

identical, where $k = 1, 2, 3, 4$. It is worth noting that the modal values of the triangle and $\beta(0.15, 0.09)$ distributions are at $\underline{\delta}_A$ and $\bar{\delta}_A$, respectively.

The number of Independent and Identically Distributed (i.i.d.) samples required is determined using [17, 55]

$$H \geq \frac{\log\frac{1}{\varsigma}}{\log\frac{1}{1-\epsilon}}, \tag{3.38}$$

where $1 - \varsigma$ is the confidence interval of the estimate. The choice of $H = 10000$ for the triangle and $\beta(0.15, 0.09)$ distributions is sufficient for estimating $1 - \epsilon \leq 0.999$ with $1 - \varsigma = 0.999$.

For the purpose of comparison, two additional feedback control systems are synthesized based on Constraints (a–k) and the assumptions under Cases 1 and 3 in Tables 3.1 and 3.2. Robust stability evaluation is similarly carried out using triangle and $\beta(0.15, 0.09)$ distributions.

Table 3.1: Assumptions on $|\tilde{\delta}_1|$ and $|\tilde{\delta}_2|$

	$\lvert\tilde{\delta}_k\rvert$, $k = 1, 2$		
	Mean μ_{Ak}	Variance	Support
Case 1	0.078	0.00304	[0 0.234]
Case 2 (Section 3.4.1)	0.0937	0.00439	[0 0.281]
Case 3	0.109	0.00598	[0 0.328]

Table 3.2: Assumptions on $|\tilde{\delta}_3|$ and $|\tilde{\delta}_4|$

	$\lvert\tilde{\delta}_k\rvert$, $k = 3, 4$		
	Mean μ_{Ak}	Variance	Support
Case 1	7.8×10^{-3}	3.04×10^{-5}	[0 0.0234]
Case 2 (Section 3.4.1)	9.37×10^{-3}	4.39×10^{-5}	[0 0.0281]
Case 3	1.09×10^{-2}	5.98×10^{-5}	[0 0.0328]

The results are tabulated in Table 3.3, and plotted in Figure 3.5. Under distributional changes in plant parameters for all cases, the proportion of feedback control systems with stable closed-loop poles remains larger than the specified $1 - \epsilon$ during the design phase.

The CVaR measure is applied to the sufficient condition for closed-loop stability in (3.23). Considering the triangle distributions, a smaller proportion of the feedback control systems satisfy (3.23). Although the use of (3.23) results in a more conservative feedback control system design, it ensures that the specified $1 - \epsilon$ is satisfied when the assumptions on the mean and variance are moderately violated.

The difference between the specified $1 - \epsilon$ and the values obtained using (3.23) is mainly due to the fact that phase-stabilization of resonant modes for satisfying the performance specifications result in a highly robust feedback control system. Without considering the robust stability criterion, 80.38% of the feedback control systems have stable closed-loop poles when evaluated using triangle-distributed parametric perturbations with statistical moments as assumed in Case 2. In addition, there is conservatism due to the CVaR measure as well. However, the CVaR approximation is the tightest convex approximation of (3.23) [62].

Table 3.3: Summary of Closed-Loop Robust Stability Evaluation

	Proportion of feedback control systems			
	Specified $1 - \epsilon$	(3.23)	Stable closed-loop poles	
		Triangle	Triangle	$\beta(0.15, 0.09)$
Case 1	60.94%	87.4%	99.57%	78.93%
Case 2 (Section 3.4.1)	32.81%	75.36%	97.15%	70.58%
Case 3	13.28%	64.86%	93.93%	71%

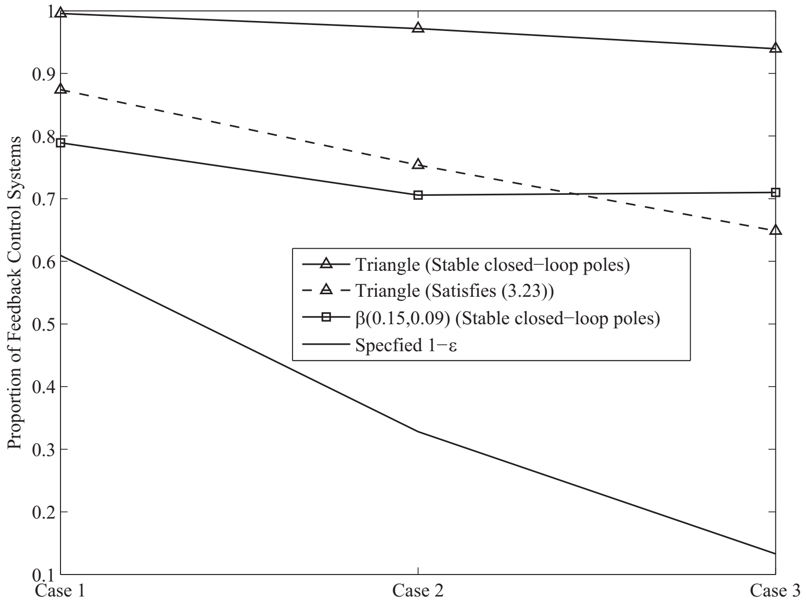

Figure 3.5: Stability of synthesized feedback control systems under varied plant parametric distributions.

3.5 Comparative Investigations

In this section, the proposed design algorithm is compared with alternative methods for considering uncertainties in integrated servo-mechanical design of robust mechatronics. For deterministic assessment, the Kharitonov's Theorem and $\mathcal{H}_\infty$ loop-shaping approaches are considered. A distribution-free randomized approach and the $\mathcal{H}_\infty$ probabilistic theory are considered under probabilistic assessment, and can be regarded as probabilistic counterparts of the Kharitonov's Theorem and $\mathcal{H}_\infty$ loop-shaping approaches, respectively. In addition, a distribution-based approach is also considered under probabilistic assessment.

The frequency response of the *mechanical plant* is shaped based on the designed controller C_D from Section 3.4 for all methods. The frequency responses of the open loop and sensitivity transfer functions from all methods are compared in Figures 3.6 and 3.7. Robust stability evaluation is carried out considering ten thousand i.i.d. samples, and the triangle and $\beta(0.15, 0.09)$ distributions are as assumed in Case 2 of Section 3.4.2. The results are tabulated in Table 3.4.

3.5.1 Deterministic Assessment

The design problem using a Kharitonov's Theorem-based approach is convexified using the robust stability criterion given by

$$\mathrm{Re}(\hat{F}(\theta, \tilde{\delta})) > 0 \ \forall \ \theta \in [0, \pi], \tag{3.39}$$

where $\tilde{\delta}_k$ varies within $[-0.281, 0.281]$ and $[-0.0281, 0.0281]$ for $k = 1, 2$, and $k = 3, 4$, respectively. The intervals are specified based on the support assumptions in Section 3.4, and Constraints (a–k) are not considered. In this case, the resonant magnitude and disturbance attenuation capability at the primary resonant frequency is reduced as shown in Figures 3.6 and 3.7, respectively. It is worth noting that Constraints (a–k) cannot be satisfied simultaneously when included in the design problem.

Using the $\mathcal{H}_\infty$ loop-shaping approach, a plant P_{D1} is designed such that

$$\left\| W_{p1}(1 + P_{D1}C_D)^{-1} \right\|_\infty < 1, \tag{3.40}$$

$$\left\| W_u \frac{P_{D1}C_D}{1 + P_{D1}C_D} \right\|_\infty < 1, \tag{3.41}$$

are satisfied, where W_{p1} denotes a low-order performance weight. The robust stability criterion is given by (3.41). The transfer function W_u is an upper bound on the magnitude of Δ_h given by

$$\Delta_h = \frac{\tilde{P}_D - P_D}{P_D}, \quad h = 1, 2, ..., 10000, \tag{3.42}$$

where P_D is as synthesized in Section 3.4. In (3.42), each $\tilde{P}_D$ is generated using triangle-distributed plant parameters with low-order moments and support as assumed in Section 3.4. Robust stability evaluation is carried out by considering $P_{D1}(1 + \Delta_h)$ as the perturbed plant, where Δ_h for $h = 1, 2, ..., 10000$, are generated using the triangle or $\beta(0.15, 0.09)$ distributions.

3.5.2 Probabilistic Assessment

The robust stability criterion for the distribution-free randomized approach is equivalent to (3.14). Using the uniformity principle [58], $\tilde{\delta}_k$ in (3.14) is assumed to be uniformly-distributed in the intervals given by $[-0.281, 0.281]$ and $[-0.0281, 0.0281]$ for $k = 1, 2$, and $k = 3, 4$, respectively. Based on the results in Section 3.4, $1 - \epsilon$ is specified as 0.3281. Using (3.38), $H = 7$ is sufficient for satisficing (3.14) with a confidence interval of $1 - \varsigma = 0.999$. The plant design problem is solved using (3.16), where $\tilde{\delta}$ is substituted with the i.i.d. samples. From Figures 3.6 and 3.7, it can be seen that Constraints (a–k) are not all satisfied in order to fulfill the robust stability criterion.

Using the $\mathcal{H}_\infty$ probabilistic theory, the objective is to synthesize a redesigned plant P_{D2} such that

$$\left\| W_{p2}(1 + P_{D2}C_D)^{-1} \right\|_\infty < 1, \tag{3.43}$$

$$\text{Prob}\left(\left\| \Delta_h \frac{P_{D2}C_D}{1 + P_{D2}C_D} \right\|_\infty < 1 \right) \geq 1 - \epsilon, \; h = 1, 2, ..., 7 \tag{3.44}$$

where W_{p2} denotes a low-order performance weight. The robust stability criterion to be satisficed is given by (3.44), where $1 - \epsilon$ is similarly specified as 0.3281, and seven i.i.d samples are considered. For the design phase, $\Delta_h \in \mathcal{RH}_\infty$ is generated using (3.42) and considering triangle-distributed plant parameters with low-order moments and support as assumed in Section 3.4. The approach for generating Δ_h is identical to the $\mathcal{H}_\infty$ loop-shaping method for the evaluation phase.

The distribution-based approach [65] is carried out by considering (3.14) as the robust stability criterion, where $1 - \epsilon$ is similarly specified as 0.3281. The random variables $\tilde{\delta}_k$ are assumed to be triangle-distributed with low-order moments and support as assumed in Section 3.4 for $k = 1, 2, ..., 4$, and seven i.i.d. samples are considered. The plant design problem is solved using (3.16), where $\tilde{\delta}$ is substituted with the i.i.d. samples. In this case, Constraints (a–k) are simultaneously satisfied.

In general, probabilistic methods consider the stabilization of a smaller number of perturbed plants compared to their deterministic counterparts. The result is an improvement in closed-loop performance as shown in Figures 3.6 and 3.7. From Table 3.3, the Kharitonov's Theorem-based approach synthesized a feedback control system which achieves the largest proportion of stable feedback control systems.

Both $\mathcal{H}_\infty$ methods produced higher order plants with negligible disturbance attenuation capabilities at the resonant frequencies. However, only a small proportion of feedback control systems are stable during robust evaluation. This is due to gain-stabilization of resonant modes using the small-gain theorem. The Nyquist stability criterion is violated when the poles of perturbed P_{D1} and P_{D2} are unstable. Feedback control systems with phase-stabilized resonant modes can be achieved using $\mathcal{H}_\infty$ methods when the inverse performance weighting functions include high-frequency anti-resonant zeros. However, it is challenging to design non-conservative weighting functions for satisficing the performance specifications, and robust stability may be reduced as a result.

Among the distribution-free, distribution-based, and CVaR-based approaches, the largest and smallest perturbation sets are considered by the distribution-free and distribution-based approaches for satisficing a particular $1 - \epsilon$, respectively. As a result, the CVaR-based approach results in a more robust feedback control system compared to the distribution-based approach. Compared to the distribution-free randomized method, the CVaR-based approach results in a feedback control system which is less robust but satisfies Constraints (a–k).

Table 3.4: Comparison of Closed-Loop Robust Stability

	Proportion of feedback control systems (Stable closed-loop poles)	
	Triangle	$\beta(0.15, 0.09)$
Kharitonov's Theorem-based	100%	100%
$\mathcal{H}_\infty$ loop-shaping	34.78%	31.8%
Distribution-free	100%	100%
$\mathcal{H}_\infty$ probabilistic	37.44%	32.9%
Distribution-based	91.76%	68.69%
CVaR-based	97.15%	70.58%

3.6 Summary

In this chapter, a convex separable parametrization in integrated servo-mechanical design is used for the synthesis of a feedback control system

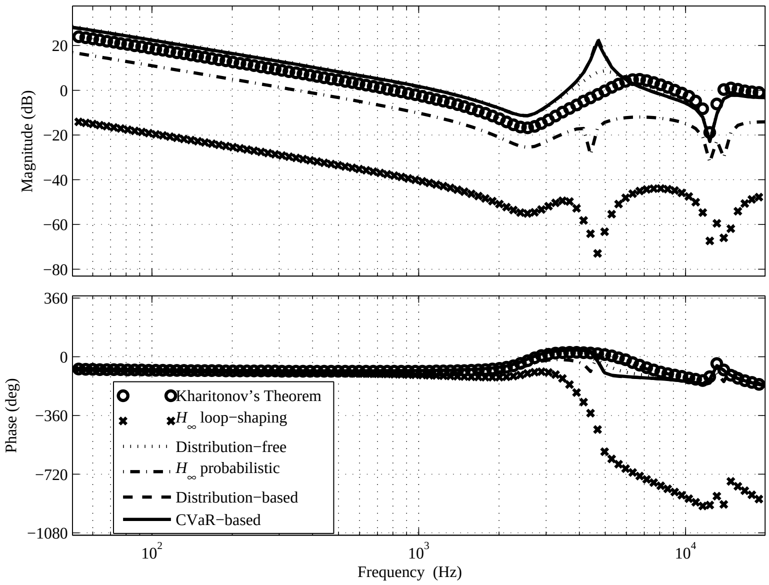

Figure 3.6: Comparison of open loop transfer functions.

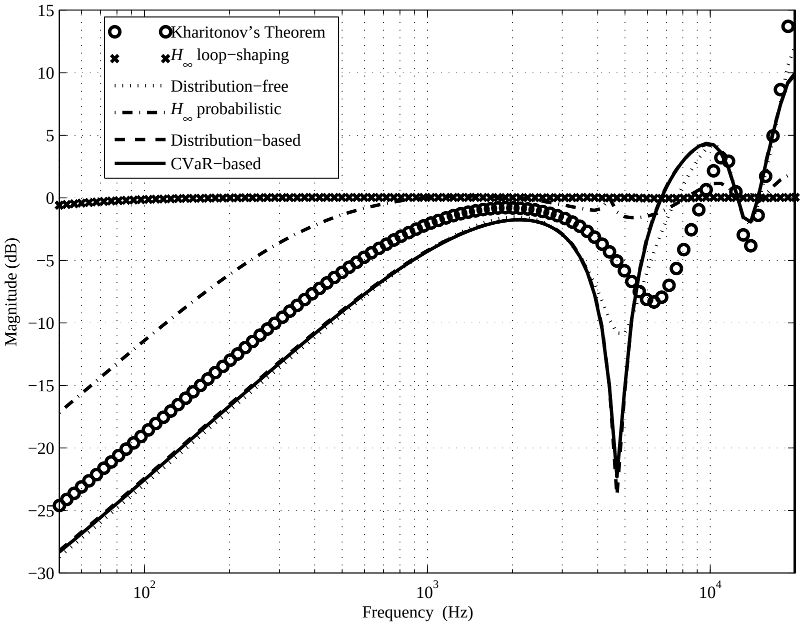

Figure 3.7: Comparison of sensitivity transfer functions.

which satisfies the performance specifications and chance-constrained robust stability criterion. Simulations results demonstrate that the specified $1-\epsilon$ remains satisfied when distributional changes in plant parameters result in moderate violation of the mean and variance assumptions during the design phase. As illustrated by the comparative investigations, the CVaR approximation enables performance specifications to be satisfied based on the specified $1-\epsilon$, and ensures a higher proportion of stable feedback control systems compared to the distribution-based approach.

In the next chapter, we consider the identification of allowable regions for the Nyquist plot of the open loop transfer function in order to carry out finite frequency redesign of the mechanical plant based on a low-order controller. The allowable regions will be derived based on performance specifications and a chance-constrained robust stability criterion.

Chapter 4

Integrated Servo-Mechanical Design of Chance-Constrained Robust Mechatronics Using Nyquist Plots

Integrated servo-mechanical design is commonly solved using numerical methods. In this chapter, finite frequency reshaping of the mechanical plant based on a low-order controller is carried out by identifying allowable regions for the Nyquist plot of the open loop transfer function. The allowable regions are derived based on performance specifications and chance-constrained robust stability criterion. Simulation results using the proposed approach synthesize a feedback control system with high-frequency disturbance attenuation specifications further satisfied based on the robust stability criterion.

4.1 Background

The Bode and Nyquist plots are well-established graphical tools commonly used for the design of feedback control systems. SBode [66] and RBode [67] plots are proposed to include performance and robust performance constraints on the open loop Bode plot, respectively. In [67], deterministic and norm-bounded uncertainties are considered. The CRCBode plot is proposed in [68] for designing robust controllers for nonlinear single-input-single-output systems using the Bode plot. Phase and gain information of deterministic uncertainties are represented on the Bode plot in [69].

System properties such as minimum phase, positive realness, and robust stability can be easily observed using the Nyquist plot. The inverse Nyquist array [70] is proposed for designing multi-variable feedback control systems. In order to improve tracking-following performance, the Nyquist plot is used for designing an optimal adaptive feedforward cancellation filter [71] to reject high-frequency disturbances. The Popov and circle criteria are proposed in [72] for designing an absolutely stable feedback control system considering sector-bounded time-invariant and time-varying nonlinearities in the feedback path, respectively. Robust feedback controller is designed in [73] by formulating circle condition-based frequency shaping as Linear Matrix Inequalities (LMIs). Individual generators in a multi-machine network are robustly stabilized in [74] by sequential relation to the circle criterion. In [51], the generalized Kharitonov's theorem is visualized on the Nyquist plane. Robust stability of the feedback control system in the presence of positive real and negative imaginary uncertainties can be ensured by restricting the complementary sensitivity transfer function to the right [75] and lower [76] half of the Nyquist plane, respectively. In [14], control design was carried out under a unified framework considering the unit disc, robust disc, and sensitivity disc regions in the Nyquist plane.

In this chapter, a graphical approach is proposed for reshaping the high-frequency characteristics of the mechanical plant based on a low-order controller to satisfy performance specifications and chance-constrained robust stability criterion. The robust stability criterion is formulated using the mean and variance of the plant parameter distributions. The fundamental significance of developing the graphical approach is to relate the analytical approach in Chapter 3 to the commonly used Nyquist plot which has several well-established theories for feedback control system design. Based on the performance and robust stability specifications, allowable regions for the Nyquist plot of the open loop transfer function are derived. As such, integrated servo-mechanical design is carried out without solving LMIs, and tradeoff between performance and chance-constrained robust stability specifications is easily visualized based on a *single* Nyquist plot.

4.2 Performance and Robust Stability Specifications

Let the transfer function of the redesigned mechanical plant P_D be given by (3.1). Plant design variables for shaping the high-frequency resonant modes and anti-resonant zeros are included in N_{PD} and D_{PD} in order for performance specifications and robust stability criterion to be satisfied using a low-order controller C given by (3.26). Let the vector of plant design variables be similarly denoted as q, where q will be obtained based on allowable regions for the Nyquist plot of open loop transfer function P_DC.

4.2.1 Performance Specifications

The performance specifications are represented as finite frequency bounded realness constraints on the sensitivity transfer function. In this chapter, the sensitivity transfer function is given by

$$S = \frac{D_{PD} D_C}{D_{PD} D_C + N_{PD} N_C}, \tag{4.1}$$

considering a unity feedback control system with P_D and C in the feed-forward path. A performance specification formulated as (2.6) is satisfied using a convex approximation given by

$$\|S_1(\bar{\theta})\|_\infty < (1 - \varphi)\phi, \tag{4.2a}$$

$$\|S_2(\bar{\theta})\|_\infty < \varphi, \ \varphi \in (0, 1), \tag{4.2b}$$

which is the approach used in Step 4 of the design algorithm in Chapter 3. In this chapter, S_1 and S_2 are given by

$$\begin{aligned} S_1 &= \frac{D_{PD}(\bar{\theta}) D_C(\bar{\theta})}{\hat{D}(\bar{\theta})}, \\ S_2 &= 1 - \frac{D_{PD}(\bar{\theta}) D_C(\bar{\theta}) + N_{PD}(\bar{\theta}) N_C(\bar{\theta})}{\hat{D}(\bar{\theta})}, \end{aligned} \tag{4.3}$$

where $\hat{D}$ similarly represents a reference characteristic equation for the redesigned feedback control system.

4.2.2 Chance-Constrained Robust Stability Criterion

The parametric perturbation of P_D by random variables $\tilde{\delta}_k$ is represented using the multiplicative uncertainty structure given in (3.10), where $\mu_k = 0$

and $k = 1, 2, ..., K$. Using the same method in Chapter 3, $\hat{F}(\theta, \tilde{\delta})$ is derived as

$$
\begin{aligned}
&\hat{F}(\theta, \delta) = \hat{F}_0(\theta) + \sum_{k=1}^{K} \hat{F}_k(\theta)\tilde{\delta}_k, \\
&\hat{F}_0 := \frac{D_C D_{PD} + N_C N_{PD}}{\hat{D}}, \\
&\hat{F}_k := \begin{cases} \frac{D_C}{\hat{D}} a_k(z^k - 1) \text{ for } k = 1, 2, ..., n_p - 1, \\ \frac{N_C}{\hat{D}} b_{k-n_p+1}(z^{k-n_p+1} - 1) \text{ for } k = n_p, n_p + 1, ..., K. \end{cases}
\end{aligned} \tag{4.4}
$$

The robust stability criterion is similarly formulated as an individual chance-constrained problem given by (3.14). In order to represent the robust stability criterion as constraints on the Nyquist plane, the CVaR-based approximation in Chapter 3 is simplified by using only the assumed μ_A, $\mathbf{\Sigma_A}$, and the specified $1-\epsilon$. Using the simplified approximation, the robust stability criterion is convexified using the following theorem.

Theorem 4.1. *The individual chance-constrained specification in (3.14) is satisfied if there exist plant design vector* q *and* $\eta_k \in \mathbb{R}$*, where* $k = 0, 1, ..., K$*, such that*

$$\mathrm{Re}\left(\hat{F}_k(\theta)\right) > -\eta_k \ \forall \ \theta \in [0, \pi], \ \ k = 1, 2, ..., K, \tag{4.5a}$$

$$\mathrm{Re}\left(-\hat{F}_k(\theta)\right) > -\eta_k \ \forall \ \theta \in [0, \pi], \ \ k = 1, 2, ..., K, \tag{4.5b}$$

$$\mathrm{Re}\left(\frac{D_{PD}(\theta) D_C(\theta) + N_{PD}(\theta) N_C(\theta)}{\hat{D}(\theta)}\right) - \varrho > 0 \ \forall \ \theta \in [0, \pi], \tag{4.5c}$$

$$\varrho = (\eta)^T \mu_A + \sqrt{\Upsilon} \left\| \sqrt{\mathbf{\Sigma_A}} \, (\eta) \right\|_2, \tag{4.5d}$$

$$\eta := [\, \eta_1 \ \eta_2 \ \cdots \ \eta_K \,]^T \geq 0, \tag{4.5e}$$

where $\Upsilon := (1/\epsilon - 1)$*, and* μ_A *and* $\mathbf{\Sigma_A}$ *are as defined in Assumption 3.1.*

The proof for Theorem 4.1 is as follows.

Proof. In Chapter 3, it has been proven that based on the mean μ_A, variance $\mathbf{\Sigma_A}$, and support $[\underline{\delta}_A, \bar{\delta}_A]$ assumptions of $|\tilde{\delta}|$ in Assumption 3.1, the individual chance-constrained problem in (3.14) can be approximated by the convex constraints in (3.17).

Using only mean μ_A and variance $\mathbf{\Sigma_A}$, the constraints in (3.17) are simplified as

$$\operatorname{Re}\left(\hat{F}_0(\theta)\right) > \eta_0 \ \forall\ \theta \in [0, \pi], \tag{4.6a}$$

$$\operatorname{Re}\left(\hat{F}_k(\theta)\right) > -\eta_k \ \forall\ \theta \in [0, \pi],\ \ k = 1, 2, ..., K, \tag{4.6b}$$

$$\operatorname{Re}\left(-\hat{F}_k(\theta)\right) > -\eta_k \ \forall\ \theta \in [0, \pi],\ \ k = 1, 2, ..., K, \tag{4.6c}$$

$$v_c \leq 0, \tag{4.6d}$$

$$-\eta_0 + (\eta)^T \mu_A + \sqrt{\Upsilon} \left\| \sqrt{\mathbf{\Sigma_A}}\,(\eta) \right\|_2 \leq v_c, \tag{4.6e}$$

$$\eta := [\, \eta_1 \ \eta_2 \ \cdots \ \eta_K \,]^T \geq 0. \tag{4.6f}$$

The constraints in Theorem 4.1 are obtained by letting $v_c = 0$ and combining (4.6a) with (4.6e). ☐

4.3 Main Results

In this section, the performance specifications in (4.2) and robust stability criterion formulated using Theorem 4.1 are translated into allowable regions for the Nyquist plot of open loop transfer function $P_D C$. It is worth noting that when the sensitivity disc in Section 1.6 is of radius $1/\phi$, the avoidance of the sensitivity disc by the open loop transfer function $P_D C$ over a specific frequency range corresponds to $|1 + P_D C|^{-1} < \phi$ over the same frequency range, which coincides with a performance specification. The results in this section is based on extending the sensitivity disc concept in order to include chance-constrained robust stability. For simplicity, a polynomial $\hat{D}(\bar{\theta})$ which is a function of the finite frequency range $\bar{\theta}$ is represented using $\hat{D}$ in this section, unless otherwise stated.

4.3.1 Performance Specifications on Nyquist Plane

The following lemma is used for representing part of the performance specifications as positive realness constraints.

Lemma 4.1. *The constraints in (4.2b) is equivalent to positive realness constraints given by*

$$\begin{aligned} \mathrm{Re}\left(\frac{D_{PD}D_C+N_{PD}N_C}{\hat{D}}\right)&>1-\varphi,\\ \mathrm{Re}\left(\frac{D_{PD}D_C+N_{PD}N_C}{\hat{D}}\right)&<1+\varphi. \end{aligned} \tag{4.7}$$

Proof. A relation between Bounded Real Lemma and Positive Real Lemma is established in [77] for $\bar{\theta}:=[0,\pi]$, and therefore holds for $\bar{\theta}:=[\theta_{\bar{l}},\theta_{\bar{u}}]$. Based on the relation in [77], the constraint in (4.2b) is equivalent to

$$\mathrm{Re}\left(\frac{\hat{D}-\varphi^{-1}(\hat{D}-D_{PD}D_C+N_{PD}N_C)}{\hat{D}+\varphi^{-1}(\hat{D}-D_{PD}D_C+N_{PD}N_C)}\right)>0. \tag{4.8}$$

In [78], it is shown that (4.8) is satisfied if and only if

$$\begin{aligned} \mathrm{Re}\left(\frac{\hat{D}-\varphi^{-1}(\hat{D}-D_{PD}D_C+N_{PD}N_C)}{\hat{D}}\right)&>0,\\ \mathrm{Re}\left(\frac{\hat{D}+\varphi^{-1}(\hat{D}-D_{PD}D_C+N_{PD}N_C)}{\hat{D}}\right)&>0, \end{aligned} \tag{4.9}$$

are satisfied. The constraints in (4.9) can be rewritten as

$$\begin{aligned}&\begin{cases}\operatorname{Re}\left(1-\varphi^{-1}+\frac{\varphi^{-1}(D_{PD}D_C+N_{PD}N_C)}{\hat{D}}\right)>0\\ \operatorname{Re}\left(1+\varphi^{-1}-\frac{\varphi^{-1}(D_{PD}D_C+N_{PD}N_C)}{\hat{D}}\right)>0\end{cases}\\ \equiv&\begin{cases}\operatorname{Re}\left(\frac{D_{PD}D_C+N_{PD}N_C}{\hat{D}}\right)>1-\varphi\\ \operatorname{Re}\left(\frac{D_{PD}D_C+N_{PD}N_C}{\hat{D}}\right)<1+\varphi\end{cases}.\end{aligned} \tag{4.10}$$

□

Using Lemma 4.1, the relation between φ from the performance specifications and ϱ from the robust stability criterion is established by the following theorem.

Theorem 4.2. *The $\mathcal{H}_\infty$ norm of S is minimized to $(\varrho\phi(2-\varrho)^{-1},\phi)$ when φ is equivalent to $1-\varrho$, $\|S_1\|_\infty<(\varrho)\phi$ is satisficed, and $\|S_2\|_\infty<1-\varrho$ is satisfied.*

Proof. From (4.2b), it can be seen that satisfying the bounded realness constraint implies

$$1-\varphi<\left\|\frac{D_CD_{PD}+N_CN_{PD}}{\hat{D}}\right\|_\infty<1+\varphi. \tag{4.11}$$

As a result,

$$\frac{(1-\varphi)\phi}{1+\varphi}<\|S\|_\infty<\phi \tag{4.12}$$

when (4.11) is combined with (4.2a), where (4.2a) is satisficed. In addition, $\frac{(1-\varphi)\phi}{1+\varphi}$ decreases as φ is increased.

In order to fulfill (2.6) and (3.14), the constraints in (4.7) and (4.5c) have to be satisfied. From the relationship between φ and ϱ as shown in Figure 4.1, it can be seen that when $1-\varphi$ is smaller than ϱ, the constraint given by (4.5c) may not be satisfied. As such, the maximum value of φ in order to satisfy all constraints is given by $1-\varrho$, where $\varrho\in(0,1)$. By substituting φ with $1-\varrho$ in (4.12), the constraint given by

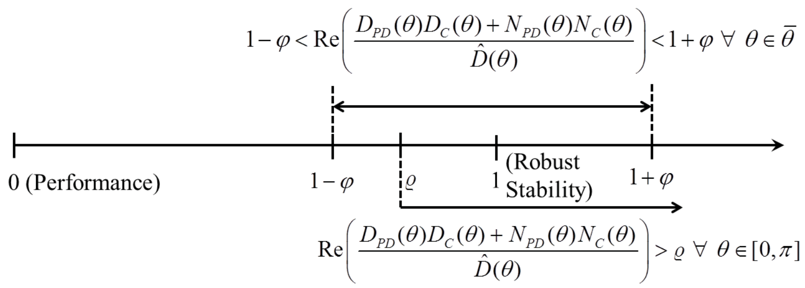

Figure 4.1: Relationship between φ and ϱ.

$$\frac{(\varrho)\phi}{2-\varrho}<\|S\|_{\infty}<\phi \tag{4.13}$$

is obtained when $\|S_1\|_{\infty}<(\varrho)\phi$ is satisficed, and $\|S_2\|_{\infty}<1-\varrho$ is satisfied.

$\square$

Remark 4.1. *From Figure 4.1 and (4.13), it is worth noting that performance can be improved based on the knowledge of the robust stability criterion. The tradeoff in robust stability increases as ϱ is reduced to zero, and vice versa as ϱ is increased to one.*

The following Lemma is used for translating the performance specifications into graphical constraints on the Nyquist plane.

Lemma 4.2. *The constraints in (4.2a–4.2b) are equivalent to*

$$\left\|\left(\frac{\hat{D}}{D_{PD}D_C}-1\right)+1\right\|_{\infty}>\frac{1}{\phi}+\varphi\left\|\frac{\hat{D}}{D_{PD}D_C}\right\|_{\infty}, \tag{4.14a}$$

$$\left\|\left(\frac{\hat{D}}{D_{PD}D_C}-1\right)-\frac{N_{PD}N_C}{D_{PD}D_C}\right\|_{\infty}<\varphi\left\|\frac{\hat{D}}{D_{PD}D_C}\right\|_{\infty}. \tag{4.14b}$$

Proof. The constraint given by

$$\left\|\frac{D_{PD}D_C}{\hat{D}}\right\|_\infty<(1-\varphi)\phi \tag{4.15}$$

is equivalent to

$$\begin{aligned}
&\left\|\frac{\hat{D}}{D_{PD}D_C}\right\|_\infty>\frac{1}{(1-\varphi)}\frac{1}{\phi}\\
\equiv&\left\|\frac{\hat{D}}{D_{PD}D_C}\right\|_\infty-\varphi\left\|\frac{\hat{D}}{D_{PD}D_C}\right\|_\infty>\frac{1}{\phi}\\
\equiv&\left\|\left(\frac{\hat{D}}{D_{PD}D_C}-1\right)+1\right\|_\infty>\frac{1}{\phi}+\varphi\left\|\frac{\hat{D}}{D_{PD}D_C}\right\|_\infty.
\end{aligned} \tag{4.16}$$

In addition, the constraint given by

$$\left\|1-\frac{D_{PD}D_C+N_{PD}N_C}{\hat{D}}\right\|_\infty<\varphi \tag{4.17}$$

is equivalent to

$$\begin{aligned}
&\left\|\frac{\hat{D}-(D_{PD}D_C+N_{PD}N_C)}{D_{PD}D_C}\frac{D_{PD}D_C}{\hat{D}}\right\|_\infty<\varphi\\
\equiv&\left\|\frac{\hat{D}}{D_{PD}D_C}-\left(1+\frac{N_{PD}N_C}{D_{PD}D_C}\right)\right\|_\infty\left\|\frac{D_{PD}D_C}{\hat{D}}\right\|_\infty<\varphi\\
\equiv&\left\|\left(\frac{\hat{D}}{D_{PD}D_C}-1\right)+\frac{N_{PD}N_C}{D_{PD}D_C}\right\|_\infty<\varphi\left\|\frac{\hat{D}}{D_{PD}D_C}\right\|_\infty.
\end{aligned} \tag{4.18}$$

□

Based on Theorem 4.2 and Lemma 4.2, $\|S\|_\infty$ can be reduced to $(\frac{\varrho\phi}{2-\varrho},\phi)$

using

$$\left\|\left(\frac{\hat{D}}{D_{PD}D_C}-1\right)+1\right\|_\infty > \frac{1}{\phi}+(1-\varrho)\left\|\frac{\hat{D}}{D_{PD}D_C}\right\|_\infty, \tag{4.19a}$$

$$\left\|\left(\frac{\hat{D}}{D_{PD}D_C}-1\right)-\frac{N_{PD}N_C}{D_{PD}D_C}\right\|_\infty < (1-\varrho)\left\|\frac{\hat{D}}{D_{PD}D_C}\right\|_\infty. \tag{4.19b}$$

A graphical representation of (4.19a–4.19b) is shown in Figure 4.2. The

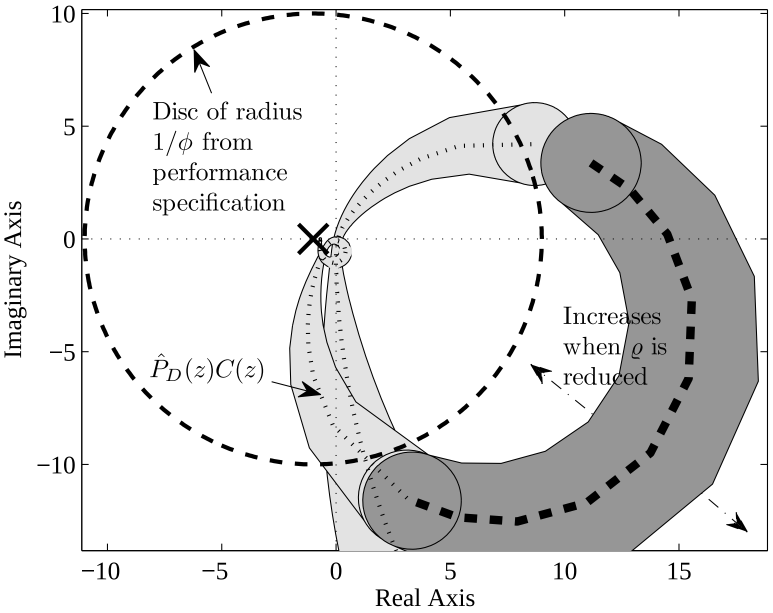

Figure 4.2: Allowable regions (shaded) for Nyquist plot of P_DC based on performance and robust stability specifications.

dark shaded area is made up of discs of radius $(1-\varrho)\left\|\frac{\hat{D}(\theta)}{D_{PD}(\theta)D_C(\theta)}\right\|_\infty$ centered at $\left(\frac{\hat{D}(\theta)}{D_{PD}(\theta)D_C(\theta)}-1\right)$ for $\theta\in\bar{\theta}$. For simplicity, it is sufficient to only plot the discs at $\theta=\theta_{\bar{l}}$ and $\theta=\theta_{\bar{u}}$. In fact, $\left(\frac{\hat{D}(z)}{D_{PD}(z)D_C(z)}-1\right)$ can be regarded as a fictitious system $\hat{P}_D(z)C(z)$. The closed-loop characteristic polynomial from the negative feedback loop of $\hat{P}_D(z)C(z)$ is equivalent to $\hat{D}(z)$. The Nyquist plot of $\hat{P}_D(\theta)C(\theta)$ for $\theta\in\bar{\theta}$ is represented using the thick dashed-line. From Figure 4.2, it can be seen that the constraint in (4.19a) is satisficed when the dark shaded area just avoids the dashed sensitivity disc of radius $1/\phi$. The point $(-1+j0)$ is indicated by the cross. In order to satisfy (4.19b), it can be seen that the Nyquist plot of $P_D C$ has to be within the dark shaded area. The derivation of the light shaded area based on the robust stability criterion is detailed in the next section.

4.3.2 Chance-Constrained Robust Stability Criterion on Nyquist Plane

The following Lemma is used for translating the positive realness constraint from the robust stability criterion into an equivalent bounded realness constraint.

Lemma 4.3. *The positive realness constraint given by (4.5c) is equivalent to*

$$\frac{\left\|\left((\varrho+1)\frac{\hat{D}}{D_{PD}D_C}-1\right)-\frac{N_{PD}N_C}{D_{PD}D_C}\right\|_\infty}{\left\|\left((\varrho-1)\frac{\hat{D}}{D_{PD}D_C}-1\right)-\frac{N_{PD}N_C}{D_{PD}D_C}\right\|_\infty}<1. \tag{4.20}$$

Proof. Using the relation between Bounded Real Lemma and Positive Real Lemma [77],

$$\begin{aligned}
&\mathrm{Re}\left(\frac{D_{PD}D_C+N_{PD}N_C}{\hat{D}}\right)-\varrho>0,\\
\equiv&\left\|\frac{\hat{D}-D_{PD}D_C-N_{PD}N_C+\varrho\hat{D}}{\hat{D}+D_{PD}D_C+N_{PD}N_C-\varrho\hat{D}}\right\|_\infty\leq 1\\
\equiv&\left\|\frac{\frac{\hat{D}}{D_{PD}D_C}-1-\frac{N_{PD}N_C}{D_{PD}D_C}+\frac{\varrho\hat{D}}{D_{PD}D_C}}{-\left(\frac{\hat{D}}{D_{PD}D_C}+1+\frac{N_{PD}N_C}{D_{PD}D_C}-\frac{\varrho\hat{D}}{D_{PD}D_C}\right)}\right\|_\infty<1
\end{aligned}$$

$$\equiv\frac{\left\|\left((\varrho+1)\frac{\hat{D}}{D_{PD}D_C}-1\right)-\frac{N_{PD}N_C}{D_{PD}D_C}\right\|_\infty}{\left\|\left((\varrho-1)\frac{\hat{D}}{D_{PD}D_C}-1\right)-\frac{N_{PD}N_C}{D_{PD}D_C}\right\|_\infty}<1. \tag{4.21}$$

□

Based on Lemma 4.3, the following Lemma is used for representing the robust stability criterion as constraints on the Nyquist plane.

Lemma 4.4. *The constraint in (4.20) can be satisfied using*

$$\left\|\left(\frac{\hat{D}}{D_{PD}D_C}-1\right)-\frac{N_{PD}N_C}{D_{PD}D_C}\right\|_\infty<(1-\varrho)\left\|\frac{\hat{D}}{D_{PD}D_C}\right\|_\infty, \tag{4.22}$$

where $\varrho\in(0,1)$.

Proof. The $\mathcal{H}_\infty$-norm measures in the numerator and denominator of (4.20) can be regarded as the distance between $\frac{N_{PD}N_C}{D_{PD}D_C}$ and $(\varrho+1)\frac{\hat{D}}{D_{PD}D_C}-1$, and the distance between $\frac{N_{PD}N_C}{D_{PD}D_C}$ and $(\varrho-1)\frac{\hat{D}}{D_{PD}D_C}-1$ on the Nyquist plane for $\theta\in[0,\pi]$, respectively. The constraint in (4.20) is satisfied for $\frac{N_{PD}N_C}{D_{PD}D_C}$ designed to be between $\varrho\frac{\hat{D}}{D_{PD}D_C}-1$ and $(\varrho+1)\frac{\hat{D}}{D_{PD}D_C}-1$ on the Nyquist plane for $\theta\in[0,\pi]$. As a result,

$$\begin{aligned}&\left\|\left((\varrho+1)\frac{\hat{D}}{D_{PD}D_C}-1\right)-\frac{N_{PD}N_C}{D_{PD}D_C}\right\|_\infty\\ <&\left\|\left((\varrho+1)\frac{\hat{D}}{D_{PD}D_C}-1\right)-\left(\varrho\frac{\hat{D}}{D_{PD}D_C}-1\right)\right\|_\infty\\ \equiv&\left\|\left((\varrho+1)\frac{\hat{D}}{D_{PD}D_C}-1\right)-\frac{N_{PD}N_C}{D_{PD}D_C}\right\|_\infty<\left\|\frac{\hat{D}}{D_{PD}D_C}\right\|_\infty\end{aligned} \tag{4.23}$$

is a sufficient condition for satisfying (4.20). By applying Triangle Inequality, (4.23) can be satisfied using (4.22). □

The constraint in (4.22) corresponds to the constraint in (4.19b) for $\theta\in[0,\pi]$. As such, both performance and robust stability specifications are based on restricting $\left\|\left(\frac{\hat{D}}{D_{PD}D_C}-1\right)-\frac{N_{PD}N_C}{D_{PD}D_C}\right\|_\infty$ to less than $(1-\varrho)\left\|\frac{\hat{D}}{D_{PD}D_C}\right\|_\infty$ over their respective frequency ranges.

The light shaded area in Figure 4.2 is derived from (4.22) for $\theta\in[0,\pi]$ excluding $\bar{\theta}$ from the performance specification. The thick dotted line represents the Nyquist plot of $\hat{P}_D C$ over the same frequency range. The Nyquist plot of $P_D C$ has to be within both light and dark shaded areas in order to satisfy the robust stability constraint in (4.22). The performance specifications will be satisfied by a less robust feedback control system with higher performance when ϱ is decreased. This is due to the fact that a reduction in ϱ results in an increase in the width of the shaded areas as shown in Figure 4.2, and the magnitude of $\hat{P}_D(\bar{\theta})C(\bar{\theta})$ has to be increased in order to satisfice (4.19a). In addition, the shaded areas will not encircle $(-1+j0)$ when $\hat{D}(z)$ and $D_{PD}(z)D_C(z)$ are Schur stable.

4.3.3 Relation between LMI and Graphical Approaches

Let $(A_{\hat{D}}, B_{\hat{D}}, C_{S1}(q), D_{S1})$ and $(A_{\hat{D}}, B_{\hat{D}}, C_{S2}(q), D_{S2})$ represent the state-space realizations of S_1 and S_2, respectively. The state-space representation of of $\frac{D_{PD}D_C+N_{PD}N_C}{\hat{D}}$ is denoted as $(A_{\hat{D}}, B_{\hat{D}}, C_{CE}(q), D_{CE})$. Using the Generalized Kalman-Yakubovic-Popov (GKYP) Lemma, solving for the plant design variables in q to satisfy the constraints in (4.2a–4.2b) is equivalent to finding φ, Hermitian matrices Ξ_{S1} and Ξ_{S1}, as well as positive definite matrices V_{S1} and V_{S2} such that

$$\begin{bmatrix} \begin{bmatrix} \Lambda_{11}(\Xi_{S1},V_{S1}) & \Lambda_{12}(\Xi_{S1},V_{S1}) \\ \Lambda_{21}(\Xi_{S1},V_{S1}) & \Lambda_{22}(\Xi_{S1}) \end{bmatrix} - \begin{bmatrix} 0 & 0 \\ 0 & I \end{bmatrix} & \begin{bmatrix} C_{S1}(q)^* \\ D_{S1}^* \end{bmatrix} \\ \begin{bmatrix} C_{S1}(q) & D_{S1} \end{bmatrix} & -((1-\varphi)\phi)^2 \end{bmatrix} < 0, \tag{4.24}$$

$$\begin{bmatrix} \begin{bmatrix} \Lambda_{11}(\Xi_{S2},V_{S2}) & \Lambda_{12}(\Xi_{S2},V_{S2}) \\ \Lambda_{21}(\Xi_{S2},V_{S2}) & \Lambda_{22}(\Xi_{S2}) \end{bmatrix} - \begin{bmatrix} 0 & 0 \\ 0 & I \end{bmatrix} & \begin{bmatrix} C_{S2}(q)^* \\ D_{S2}^* \end{bmatrix} \\ \begin{bmatrix} C_{S2}(q) & D_{S2} \end{bmatrix} & -\varphi^2 \end{bmatrix} < 0, \tag{4.25}$$

where

$$\begin{bmatrix} \Lambda_{11}(\Xi,V) & \Lambda_{12}(\Xi,V) \\ \Lambda_{21}(\Xi,V) & \Lambda_{22}(\Xi) \end{bmatrix} := \begin{bmatrix} A_{\hat{D}} & B_{\hat{D}} \\ I & 0 \end{bmatrix}^* \Pi(\Xi,V) \begin{bmatrix} A_{\hat{D}} & B_{\hat{D}} \\ I & 0 \end{bmatrix}, \tag{4.26}$$

and $\Pi(\Xi,V)$ is defined based on the finite frequency range $\bar{\theta}$ as detailed in Section 1.5. Using Schur's complement, (4.24) is equivalent to

$$-((1-\varphi)\phi)^2 < 0 \tag{4.27a}$$

$$\left(\begin{bmatrix} C_{S1}^* \\ D_{S1}^* \end{bmatrix}\right)^+ \left(\Lambda - \begin{bmatrix} 0 & 0 \\ 0 & I \end{bmatrix}\right)\left(\begin{bmatrix} C_{S1} & D_{S1} \end{bmatrix}\right)^+ < \left[-((1-\varphi)\phi)^2\right]^{-1} \tag{4.27b}$$

From (4.27b), it can be seen that $\left[-((1-\varphi)\phi)^2\right]^{-1}$ increases when φ is increased. As a result, the solution space of Ξ_{S1}, V_{S1}, and q for satisfying (4.27) is increased. For (4.25), an increase in φ will similarly result in an increase in the solution space of Ξ_{S2}, V_{S2}, and q.

Solving for the plant design variables to satisfy constraint (4.5c) is equivalent to obtaining ϱ, Ξ_{CE}, and $V_{CE}{>}0$ to satisfy

$$\begin{bmatrix} \Lambda_{11}(\Xi_{CE}, V_{CE}) & \Lambda_{12}(\Xi_{CE}, V_{CE}) \\ \Lambda_{21}(\Xi_{CE}, V_{CE}) & \Lambda_{22}(\Xi_{CE}) \end{bmatrix} + \begin{bmatrix} 0 & -C_{CE}(q)^* \\ -C_{CE}(q) & -D_{CE}-D_{CE}^*+2\varrho \end{bmatrix} < 0, \tag{4.28}$$

where the LMI in (4.28) is derived using the GKYP Lemma. Based on the Schur's complement, (4.28) is equivalent to

$$\Lambda_{22} < -2\varrho + D_{CE} + D_{CE}^*, \tag{4.29a}$$

$$\left([\Lambda_{12} - C_{CE}^*]\right)^+ \Lambda_{11} \left([\Lambda_{21} - C_{CE}]\right)^+ < (\Lambda_{22} - D_{CE} - D_{CE}^* + 2\varrho)^{-1}. \tag{4.29b}$$

In this case, it can be seen that a smaller ϱ will result in an increase in the solution space of Ξ_{CE} to satisfy (4.29a) as $D_{CE}{=}1$. For a given $\Lambda_{22}(\Xi_{CE})$, a reduction in ϱ increases the value of $(\Lambda_{22}-D_{CE}-D_{CE}^*+2\varrho)^{-1}$, and the solution space of V_{CE} and q for satisfying (4.29b) is increased. As a result, solving for the plant design problem using the LMI approach is dependent on the values φ and ϱ.

For the graphical approach in Section 4.3, solving for (4.14a–4.14b) and (4.20) is equivalent to solving for the LMI constraints in (4.24–4.25) and (4.28), respectively. Based on $\varphi{=}1{-}\varrho$, (4.14a–4.14b) is visualized as shown in Figure 4.2, where the size of the dark shaded area representing the allowable region for the Nyquist plot of $P_D C$ is enlarged with an increase in φ. In order for performance and robust stability specifications to be based on $\left\|\left(\frac{\hat{D}}{D_{PD}D_C}-1\right)-\frac{N_{PD}N_C}{D_{PD}D_C}\right\|_\infty$ over their respective frequency ranges, (4.22) is derived as a sufficient condition for satisfying (4.20). In Figure 4.2, the light and dark shaded areas representing the allowable regions based on (4.22) are enlarged with a reduction in ϱ. It is worth noting that the LMI constraints are guaranteed to be satisfied when $P_D C$ is designed to satisfy the graphical constraints on the Nyquist plane.

Remark 4.2. *The graphical constraints in this chapter are sufficient conditions for satisfying the numerical constraints for performance and robust stability in Chapter 3. This is due to the fact that (4.24–4.25) are used for specifying the performance specifications in Chapter 3, and (4.28) is formulated based on a robust stability criterion which considers a larger perturbation set as a result of excluding the support sets of* $\tilde{\delta}$.

4.4 Design Procedure

The proposed graphical approach for integrated servo-mechanical design is detailed as

- **Step 1:** Obtain a low-order plant P_N as described in Step 1 of the design procedure in Chapter 3.
- **Step 2:** Design the low-order controller C to satisfy the conditions in Step 2 of the design procedure in Chapter 3. In addition, let N_C and D_{PN} have identical roots in order to allow C to be factorized from the designed open loop transfer function $P_D C$. The effects of imperfect pole-zero cancellation are considered by the robust stability criterion.
- **Step 3:**

Specify the reference closed-loop characteristic polynomial $\hat{D}$ using

$$(D_{PN}D_C+k_N N_{PN}N_C)(z+\alpha)^{2L}, \tag{4.30}$$

where α corresponds to a root at high frequencies, and L represents the number of high-frequency resonant modes to be redesigned. k_N is given by

$$k_N=\left.\frac{N_{PN}(z)N_C(z)+D_{PN}(z)D_C(z)-D_{PN}(z)D_C(z)(z+\alpha)^{2L}}{N_{PN}(z)N_C(z)(z+\alpha)^{2L}}\right|_{z=1}, \tag{4.31}$$

and is used for ensuring that the low-frequency gains of $P_D C$ and $P_N C$ are approximately identical.

- **Step 4:** Obtain an initial design of the fictitious system $\hat{P}_D C=\frac{\hat{D}}{D_{PD}D_C}-1$. The polynomial $D_{PD}(z):=D_{PN}(z)D_Q(z)$ is specified based on the performance specifications at high frequencies. $D_Q(z)$ can be obtained by discretizing the polynomial $D_Q(s)=\prod_{l=1}^{L}(s^2+2\zeta_l\omega_l s+\omega_l^2)$ using matched transformation. For $l=1,2,...,L$, the natural frequency ω_l is initialized as the corresponding resonant frequency of $P(z)$, and the damping ratio ζ_l is initialized using

$$M_r=(2\zeta_l\sqrt{1-\zeta_l^2})^{-1}, \tag{4.32}$$

where M_r is the desired amount of disturbance attenuation at ω_l.

- **Step 5:** Based on the specified $1-\epsilon$, μ_A, and $\mathbf{\Sigma_A}$, determine the value of ϱ using (4.5a)–(4.5b) and (4.5d). The robust stability criterion cannot be satisfied for large values of $1-\epsilon$, μ_A, and $\mathbf{\Sigma_A}$ such that $\varrho\geq1$. In (4.5a)–

(4.5b), $\hat{F}_k$ is formulated based on the known $\hat{P}_D$ of order $n_n{+}2L$ using (4.4), and $-\eta_k$ is obtained as the tightest lower bound on $\mathrm{Re}\left(\hat{F}_k(\theta)\right)$ and $\mathrm{Re}\left(-\hat{F}_k(\theta)\right)$ for all $\theta{\in}[0,\pi]$, where $k{=}1,2,...,K$. Plot each performance specification as a sensitivity disc of radius $1/\phi$, and obtain the allowable regions for the Nyquist plot of P_DC based on (4.19b).

- **Step 6:** Demarcate the allowable regions based on (4.22) which is derived from the robust stability criterion.

- **Step 7:** Design $\hat{P}_DC$ such that the sensitivity discs from the performance specifications are just avoided as shown in Figure 4.2. The constraint in (4.19a) is satisficed as a result. $\hat{P}_DC$ can be designed by by adjusting the value of ζ_l beginning with the largest resonant mode. A sensitivity disc can be avoided by reducing the value of ζ_l, where $l{=}1,2,...,L$.

- **Step 8:** Obtain the Nyquist plot of P_DC as a curve which passes through the allowable regions. A simple choice is given by $k_P\hat{P}_DC$, where k_P is a constant gain. The order of P_D is given by $n_p{=}n_n{+}2L$.

The flowchart shown in Figure 4.3 is a summary of the above iterative algorithm.

Remark 4.3. *The main advantage of the above graphical approach is the derivation of allowable regions on the Nyquist plot for the redesigned open loop transfer function P_DC, as opposed to a single solution using the analytical approach in Chapter 3. The allowable regions are useful when considering the fact that practical realization might require small deviations from the obtained design in simulation. The other advantage of the graphical approach is ease of implementation as it involves the plotting of Nyquist plots and allowable regions without the use of numerical solvers.*

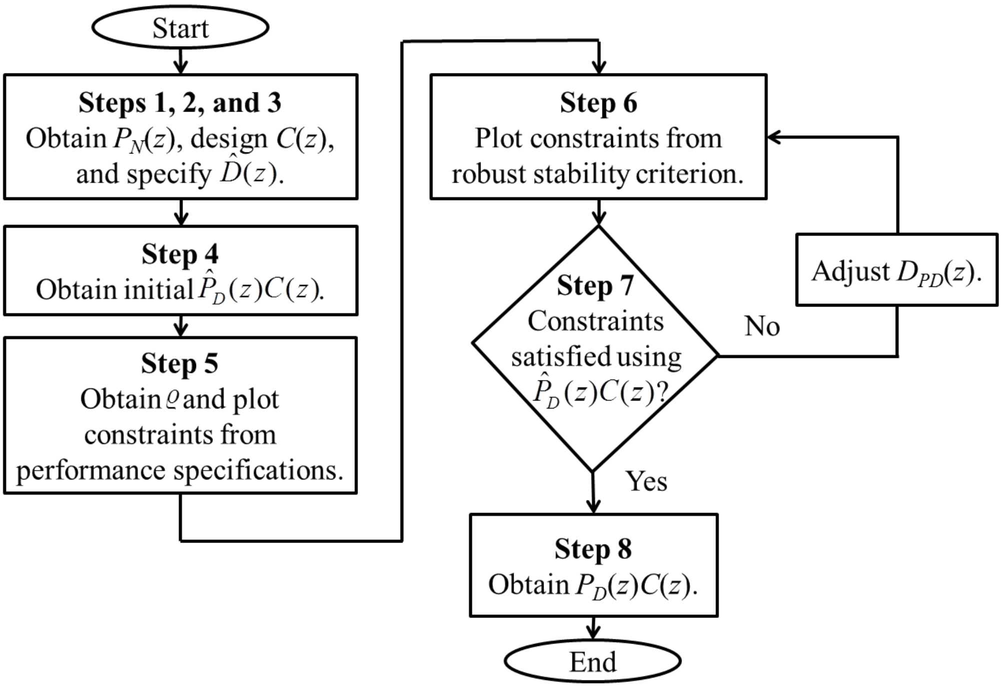

Figure 4.3: Summary of design algorithm.

From the perspective of computational complexity, there is no obvious advantage using the graphical approach. For the analytical approach, the number of unknown variables to be solved is greater than the number of design variables for the feedback control system. This is due to the Hermitian matrices Ξ *and* V *in the GKYP Lemma-based LMIs, and slack variables from the CVaR approximation. On the other hand, the iterative graphical approach involves graph plotting instead of solving for unknown variables.*

4.5 Simulation Example

According to the design procedure, the low-order plant P_N is obtained as (3.34) in Step 1. In Step 2, a first-order lag compensator C is designed as

$$C=\frac{N_C}{D_C}=\frac{0.5539z-0.0525}{z-0.9979} \tag{4.33}$$

to result in an open loop control system $P_N C$ with an open loop bandwidth of 1.35 kHz. In order to redesign $L=2$ resonant modes to be phase-stabilized by C, the characteristic polynomial $\hat{D}$ is formulated in Step 3 using $L=2$, $\alpha=0$ which result in dead-beat poles, and $k_N=1$.

The performance specifications are

a) $\left|S(\bar{\theta}_a)\right|<-l_1$, $0.975f_1\ (2\pi/F_s) \leq\bar{\theta}_a\leq 1.025f_1\ (2\pi/F_s)$ and

b) $\left|S(\bar{\theta}_b)\right|<-l_2$, $0.975f_2\ (2\pi/F_s) \leq\bar{\theta}_b\leq 1.025f_2\ (2\pi/F_s)$,

where l_1, f_1, l_2, and f_2 are given by 20 dB, 4.70 kHz, 1 dB, and 13.5 kHz, respectively. Gains l_1 and l_2 are chosen as described in Chapter 3. The constraints on low-frequency gain and spillover effects are not included in this case as the focus is on further satisfying the disturbance attenuation specifications based on the robust stability criterion. The initial design of the fictitious system $\hat{P}_D C$ is obtained in Step 4 using $M_1=10^{(l_1/20)}$ and $M_2=10^{(l_2/20)}$.

For Steps 5–7, the desired probability tolerance for closed-loop stability is specified as $1-\epsilon=0.50$. As an example, the numerator and denominator coefficients of the fifth order and relative degree one $\hat{P}$ are perturbed by $\tilde{\delta}=[\tilde{\delta}_1\ \tilde{\delta}_2 \cdots \tilde{\delta}_8]^T$ according to the structure in (3.10), where each element of $\tilde{\delta}$ is assumed to vary within $[-0.08, 0.08]$ as a result of mass production. Using the uniform distribution, μ_{Ak} of $|\tilde{\delta}_k|$ is given by 0.04 for $k=1, 2, ..., 8$, and $\mathbf{\Sigma_A}$ is given by $0.0231I$. The uniform distribution is used solely for the purpose of deriving the low-order moments for the CVaR approximation.

In fact, there are many other distributions with the assumed mean and variance.

According to Constraints (a–b), sensitivity discs of radii 10 and 1.12 are plotted on the Nyquist plane. The discs are shown in Figures 4.4 and 4.5, where $(-1+j0)$ is indicated by a cross. The allowable regions for the Nyquist plot of P_DC are obtained, and the Nyquist plot of the final design for the fictitious system is shown in Figures 4.4 and 4.5. The values of ζ_1 and ζ_2 for the final design of $\hat{P}_DC$ are given by 0.0251 and 0.0747, respectively.

In Figure 4.4, the allowable regions based on Constraint (a) and the robust stability criterion is shown. For frequency range $\bar{\theta}_a$, the Nyquist plot of $\hat{P}_DC$ is represented using the thick dashed-line, and the dark shaded area represents the region which the Nyquist plot of P_DC has to pass through. It can be seen that $\hat{P}_DC$ is designed such that the dark shaded area just avoids the dashed disc.

The allowable regions based on Constraint (b) and the robust stability criterion is shown in Figure 4.5. The thick dashed-dot line represents the Nyquist plot of $\hat{P}_DC$ for frequency range $\bar{\theta}_b$, and the dark shaded area represents the region which the Nyquist plot of P_DC has to enter for $\theta \in \bar{\theta}_b$. In Figures 4.4 and 4.5, the thick dotted line and the light shaded area represent the Nyquist plot of $\hat{P}_DC$ and the allowable regions as a result of the robust stability criterion for the frequency range $[2\pi 500, 2\pi 20000]$ excluding $\bar{\theta}_a \cup \bar{\theta}_b$, respectively. The Nyquist plot of $\hat{P}_DC$ is not shown for frequencies less than 0.5 kHz due to the focus on performance specifications and frequency response changes at high frequencies.

In Step 8, P_DC is obtained using k_P=1.0593, and n_p=5. The order

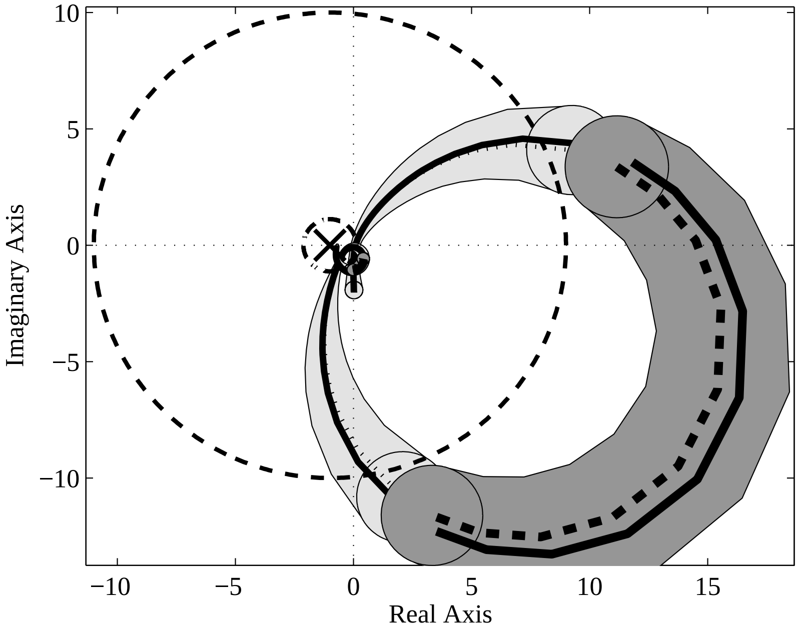

Figure 4.4: Nyquist plot of $P_D C$ (thick solid lines) passing through allowable regions from Constraint (a) and robust stability criterion.

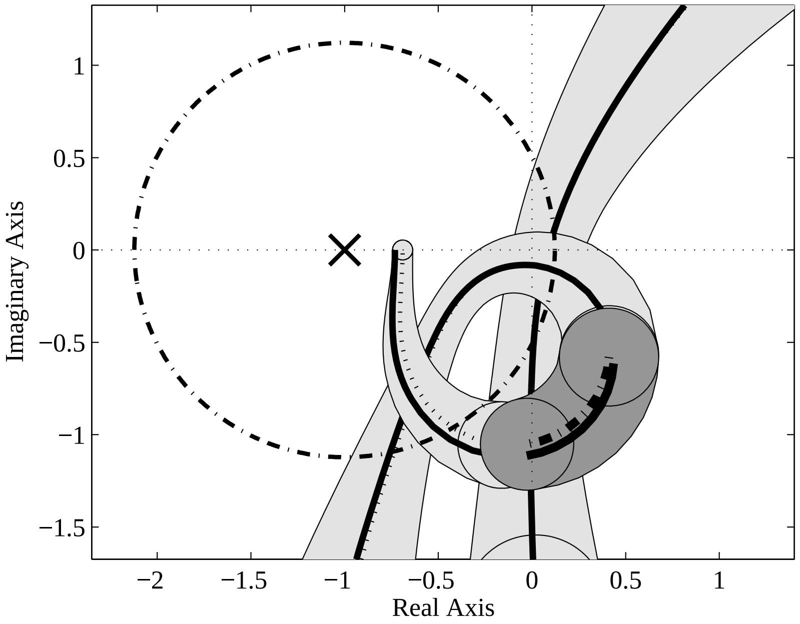

Figure 4.5: Enlarged Nyquist plot of $P_D C$ (thick solid lines) passing through allowable regions from Constraint (b) and robust stability criterion.

of P_D is greater than the order of P by one as discussed in Chapter 2. The Nyquist plot of P_DC is shown by the solid lines in Figures 4.4 and 4.5, where the discontinuities are used to indicate the intervals where performance specifications are considered. The frequency response of P_D with resonant frequencies at 4.7 kHz and 13.5 kHz is derived as shown in Figure 4.6.

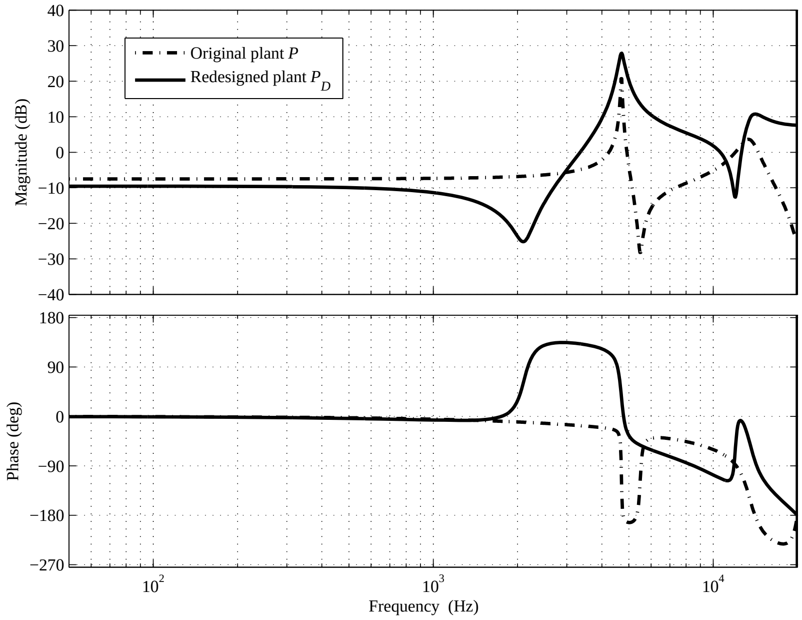

Figure 4.6: Frequency responses of original mechanical plant P and redesigned plant P_D.

4.6 Performance and Robustness Analysis

The frequency responses of PC and P_DC are shown in Figure 4.7. The resonant modes of P are neither gain nor phase-stabilized by C, while both resonant modes of P_D are phase-stabilized by C. However, the open loop bandwidth of P_DC is reduced to 0.9 kHz mainly as a result of an anti-resonant zero at 2.12 kHz. The frequency response of the sensitivity transfer function $(1+P_DC)^{-1}$ is shown in Figure 4.8. From Figure 4.8, it can be seen that disturbance attenuation capabilities at the phase-stabilized resonant modes are guaranteed as a result of designing $P_D C$ based on satisfying the graphical constraints. Due to increased disturbance attenuation capabilities based on the robust stability criterion as mentioned in Theorem 4.2, the resonant peaks of P_D are larger compared to P as shown in Figure 4.6.

The open loop bandwidth and disturbance attenuation capabilities can be increased further by increasing the controller gain or k_P in Step 8 while satisfying the graphical constraints. However, spillover effects as described in Section 2.4 will be increased, and robust stability will be reduced as a result. The spillover effects may also be increased when unstable zeros are placed by the algorithm for phase-stabilizing the resonant modes. This may occur due to requiring greater disturbance attenuation at the resonant modes and/or a reduced α in Step 3. The rough guide for the synthesis of two distinct resonant modes as mentioned in Chapter 2 remains valid for the proposed algorithm. Besides, the realization of the mechanical plant can be similarly carried out as discussed in Chapter 2.

The robustness of the designed feedback control system is verified using a set of H=10000 Independent and Identically Distributed (i.i.d.) samples, where H is specified according to the guidelines in [17, 55] as discussed in chapter 3. The samples are generated by assuming $\tilde{\delta}_k$ to be uniformly distributed within the interval assumed in the design phase for k=$1, 2, ..., 8$. In fact, the set of samples considered results in a violation of the assumptions for the robust stability criterion, as formulation was carried out during the design phase using the known $\hat{P}_D$ instead of P_D. The support of $\tilde{\delta}_k$ for k=$5, 6, 7, 8$, should have been adjusted

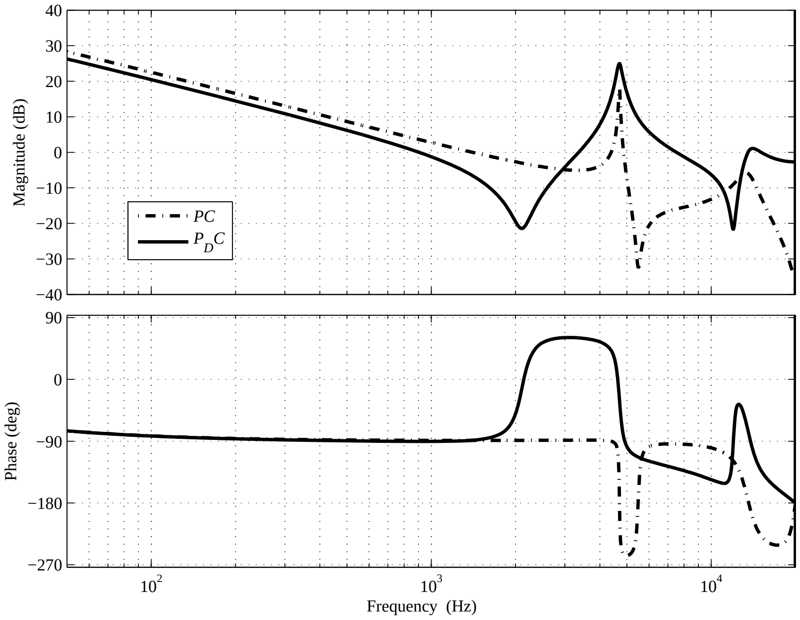

Figure 4.7: Frequency responses of open loop transfer functions.

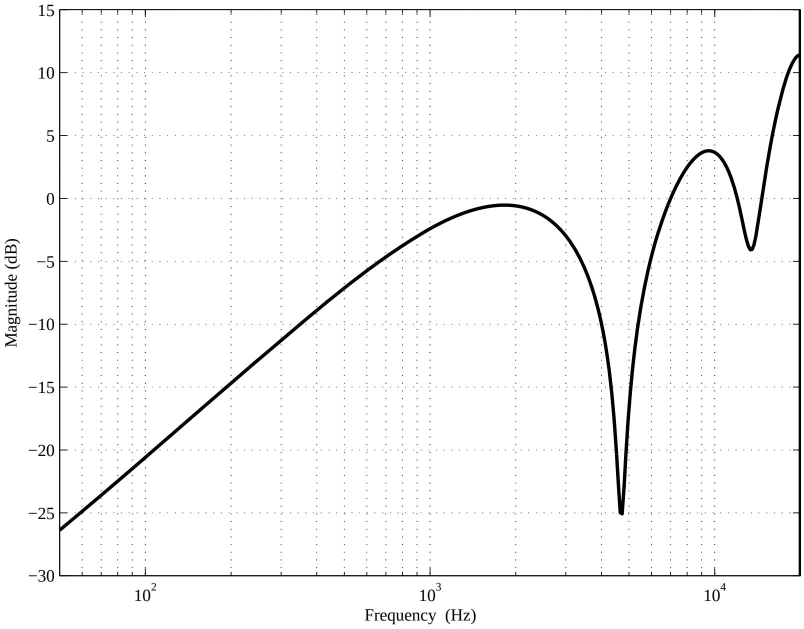

Figure 4.8: Frequency response of sensitivity transfer function.

to $\left[(\underline{\delta}_k+1)\frac{\hat{b}_{k-n_p+1}}{b_{k-n_p+1}}-1, (\bar{\delta}_k+1)\frac{\hat{b}_{k-n_p+1}}{b_{k-n_p+1}}-1\right]$, where $[\underline{\delta}_k, \bar{\delta}_k]$ represents the previous assumption on the support for deriving the variance, and $\hat{b}_{k-n_p+1}$ and b_{k-n_p+1} represent the numerator coefficients of $\hat{P}_D$ and P_D, respectively.

The results show that 100% of the feedback control systems have stable closed-loop poles, which is much greater than the specified $1-\epsilon$ despite the violations. Based on the samples generated, the specified $1-\epsilon$ remains satisfied for $k_P \leq 1.45$. The difference between $1-\epsilon$ and proportion of feedback control systems with stable closed-loop poles is due to the fact that phase-stabilization of resonant modes for satisfying the performance specifications result in a highly robust feedback control system as discussed in Chapter 3.

4.7 Comparative Investigations

In this section, the proposed graphical approach is compared with alternative graphical approaches in the literature for shaping P_DC. The methods considered include the use of sensitivity discs, negative imaginary approach, as well as RBode and SBode plots.

Based on the sole use of sensitivity discs, it is assumed that the designed P_DC is an initial fictitious system from Step 4 of the design algorithm with Nyquist plot as shown by the thick solid lines in Figures 4.9 and 4.10. The constraints of the sensitivity disc approach are satisfied, as the thick solid lines just avoid the dashed and dashed-dot sensitivity discs for frequency ranges $\bar{\theta}_a$ and $\bar{\theta}_b$, respectively. Due to the absence of robust stability constraints, the effect of increasing the distance between the thick solid lines and the sensitivity discs cannot be observed explicitly.

The thick dotted lines in Figures 4.9 and 4.10 represent the Nyquist plot of $P_D C$ obtained in Section 4.5 using the proposed graphical approach. The open loop transfer functions from both approaches have identical gains at low frequencies, and ten thousand perturbed plants are similarly generated using uniformly distributed $\tilde{\delta}$ with intervals as assumed in Section 4.5. For the sensitivity disc approach, 8.85% of the perturbed feedback control systems are stable and simultaneously satisfy Constraints (a–b). The robust performance criterion is satisfied by 26.6% of the perturbed feedback control systems for $P_D C$ designed using the proposed approach. The specified $1-\epsilon$ in Section 4.5 is violated in both cases as it was solely based on robust stability. Better robust performance is achieved using the proposed approach due to the ability to improve nominal performance while satisfying the robust stability criterion.

Strictly negative imaginary uncertainties commonly arises in mechanical systems such as the PZT active suspension which has a force input and a position output [76]. Based on the negative imaginary theorem, the transfer function $P_D C$ will be restricted to the lower half of the Nyquist plane as shown by the shaded area in Figure 4.11. The Nyquist plot of $P_D C$ designed based on the negative imaginary theorem is shown by the thick solid line in Figure 4.11. In this case, it can be seen that Constraints (a–b) are not simultaneously satisfied as the Nyquist plot of $P_D C$ does not exit and avoid the dashed disc from Constraint (a).

Both performance specifications and robust stability criterion can be considered using the RBode plot approach. The uncertainty weight W_u is similarly derived as the upper bound on the magnitude of Δ_h given

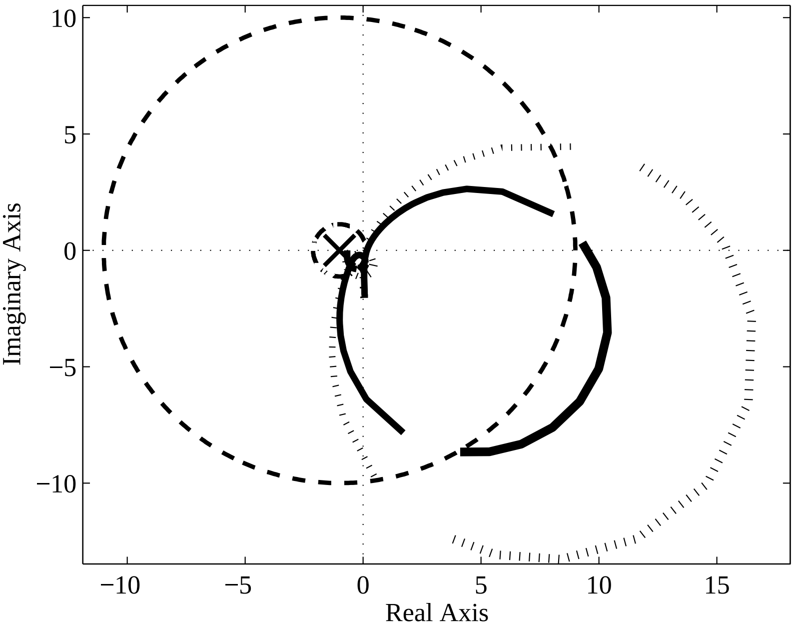

Figure 4.9: Nyquist plots of open loop transfer functions satisfying Constraint (a). Solid: Sensitivity disc approach. Dotted: Proposed.

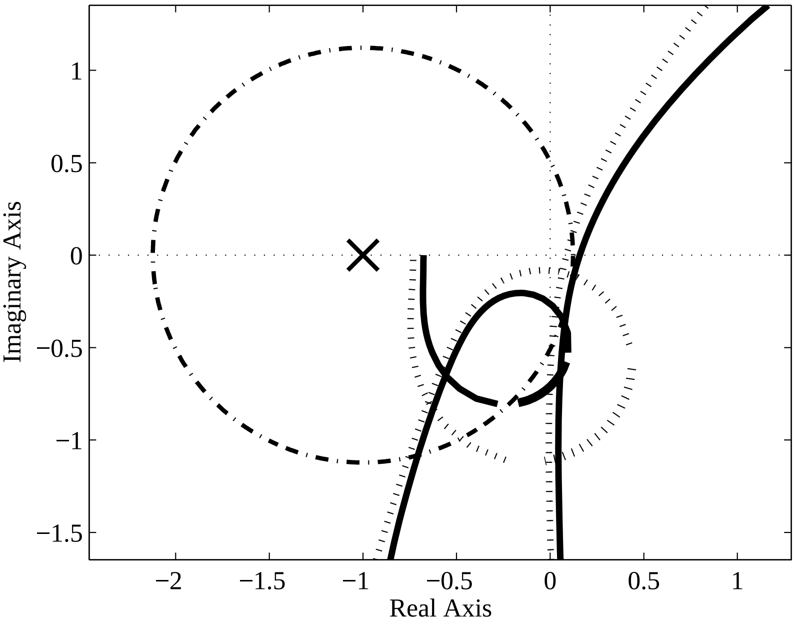

Figure 4.10: Enlarged Nyquist plots of open loop transfer functions satisfying Constraint (b). Solid: Sensitivity disc approach. Dotted: Proposed.

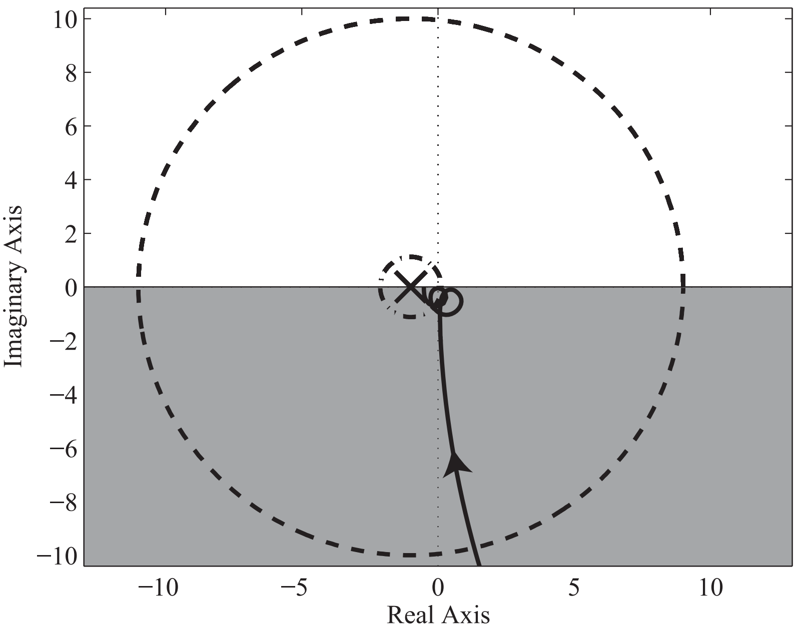

Figure 4.11: Nyquist plot of $P_D C$ based on negative imaginary theorem.

by (3.42). P_D is as synthesized in Section 4.5, and $\tilde{P}_D$ represents a perturbed P_D considering uniformly distributed $\tilde{\delta}$ with intervals as assumed in Section 4.5. The RBode plot is shown in Figure 4.12 without the performance specifications, where it can be seen that the shaded areas derived from the robust stability constraints are not avoided by the frequency response of $P_D C$. As the RBode plot approach is based on gain stabilization of resonant modes using the small-gain theorem, the primary resonant peak of $P_D C$ has to be reduced in order to avoid the shaded areas and satisfy the robust stability constraints. However, Constraints (a–b) will be violated as a result.

Using the proposed graphical approach, the performance constraints in the SBode plot are guaranteed to be satisfied. The SBode plot is shown in Figure 4.13, where it can be seen that the shaded areas derived from Constraints (a–b) are avoided by the frequency response of $P_D C$. In fact,

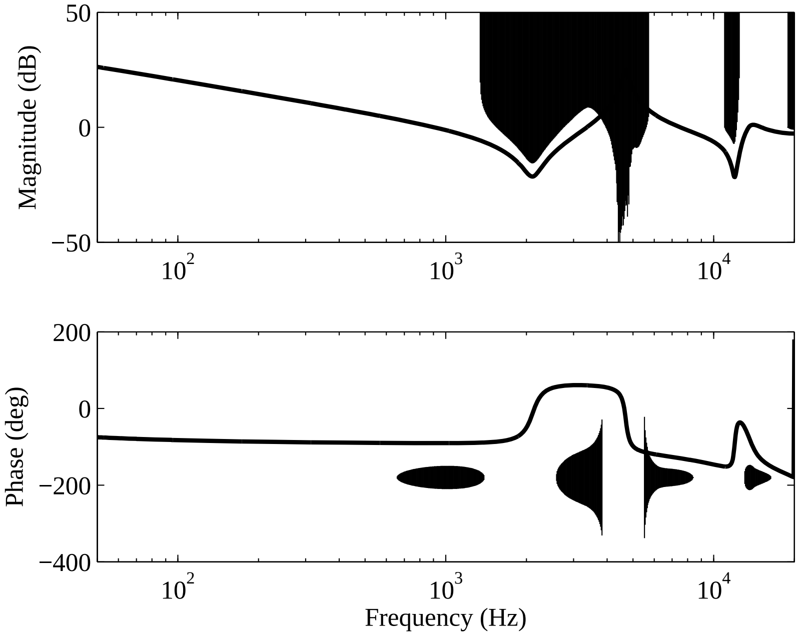

Figure 4.12: Frequency response of $P_D C$ and RBode constraints for robust stability.

the SBode plot can be regarded as a modification of the Bode plot to include the sensitivity discs. It is worth noting that the phase and gain conditions for robust stability in Theorem 1 [69] are also satisfied.

Based on the results obtained, it is generally difficult to satisfy Constraints (a–b) when uncertainties are represented deterministically. As the feedback control system can be designed based on a desired defect tolerance level using the proposed graphical approach, Constraints (a–b) can be satisfied simultaneously. In addition, robust performance is improved as compared to the sensitivity disc approach. In Chapter 3, CVaR approximation has been compared with other deterministic and probabilistic-based numerical methods such as Kharitonov's theorem, $\mathcal{H}_\infty$ probabilistic theory, and distribution-free randomized approach. The conclusions reached will be similar when the proposed graphical approach is compared with those

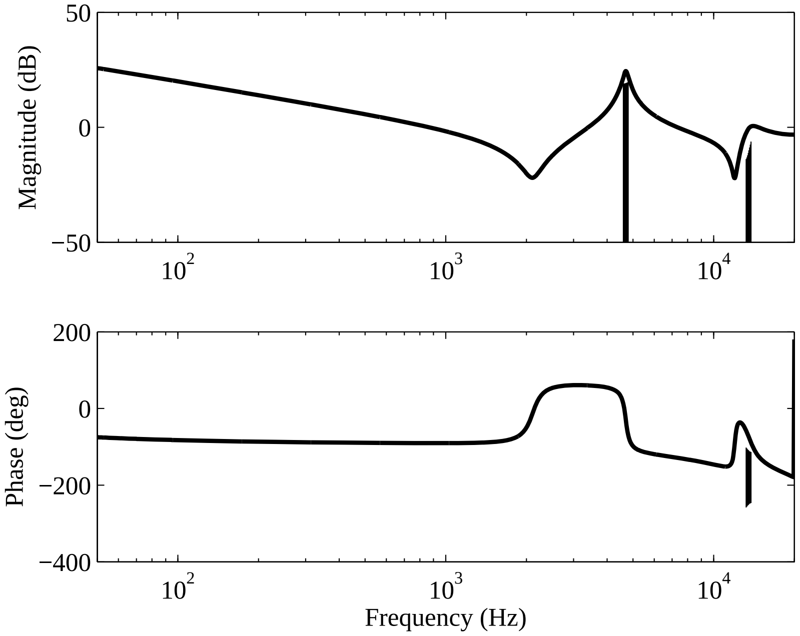

Figure 4.13: Frequency response of $P_D C$ and SBode constraints for performance.

methods.

4.8 Summary

In this chapter, the Nyquist plane is used for the synthesis of a feedback control system with performance and chance-constrained robust stability specifications satisfied. Simulation results using the proposed approach synthesize a feedback control system with high-frequency disturbance attenuation specifications further satisfied based on the robust stability criterion. Based on the results from comparison with other graphical methods, it can be seen that the chance-constrained robust stability criterion in the proposed approach enables performance specifications to be simultaneously satisfied with greater robust performance.

In the next chapter, we conclude this dissertation and discuss future research directions.

Chapter 5

Conclusion and Future Work

The traditional approach of designing a controller based on a fixed mechanical plant design is insufficient for satisfying the increasing challenging demands of high-performance mechatronics. This dissertation focuses on developing algorithms for integrated servo-mechanical design of Linear Time-Invariant (LTI) systems with a single-input-single-output mechanical plant to satisfy performance and robust stability specifications.

The main findings and results presented in this dissertation are:

1. Proposing an algorithm for reshaping the frequency response of the mechanical plant at high frequencies based on a low-order controller. The mechanical plant is redesigned to synthesis a minimum phase feedback control system which satisfies the performance specifications represented as Linear Matrix Inequality (LMI) constraints. Simulation results achieve a high-bandwidth control system with disturbance attenuation capabilities at the phase-stabilized resonant modes of the plant.

2. Formulating a convex separable parametrization for reshaping the

high-frequency response of both mechanical plant and low-order controller to satisfy performance and chance-constrained robust stability specifications. The robust stability criterion is represented as several convex constraints under the Conditional-Value-at-Risk (CVaR) approximation. Simulations results demonstrate that the specified $1-\epsilon$ remains satisfied when distributional changes in plant parameters result in moderate violation of the mean and variance assumptions during the design phase. Comparison investigations with other deterministic and probabilistic numerical methods in the literature show that the CVaR approximation enables performance specifications to be satisfied based on the specified $1-\epsilon$, and ensures a higher proportion of stable feedback control systems compared to the distribution-based approach.

3. Deriving a Nyquist plot-based approach for reshaping the response of the mechanical plant at high frequencies based on a low-order controller. Simulation results using the proposed algorithm synthesize a feedback control system with high-frequency disturbance attenuation specifications further satisfied based on the robust stability criterion. The ability to simultaneously satisfy performance specifications and achieve greater robust performance using the proposed approach is demonstrated through comparative investigations with other graphical methods in the literature.

Future high-performance mechatronics will be required to have greater positioning accuracy with robust stability due to increasing demand for smaller electronic devices, larger computational power, and larger digital storage capabilities, *etc.* As such, integrated servo-mechanical design for satisfying performance and robust stability specifications will become more essential. In view of the results obtained, the following works should be emphasized in future research:

1. Integrated servo-mechanical design of flexure-based MagLev planar motor:

   Extreme Ultra-Violet (EUV) lithography is a next-generation lithography technology for potentially enhancing the resolution of photolithography to below 10 nm [79]. As EUV lithography requires a near-vacuum environment, the moving stage for supporting the silicon wafers can only be actuated using Magnetic Levitation (MagLev) technology. The MagLev planar motor for EUV lithography is another example of a high-performance mechatronic system, which is required to have high bandwidth and resolution, as well as a large displacement range. A feedback control system with high bandwidth and resolution will be achieved when the structure of the MagLev planar motor is designed to have small mass and high stiffness. However, the displacement range may be limited as a result of high stiffness. The proposed algorithms in this dissertation can possibly be used to shape the resonant modes of the Maglev planar motor to satisfy the conflicting control objectives, after which mass and stiffness parameters can be determined from the shaped resonant modes as discussed in Section 2.5. At present, a prototype of a linear motor has been constructed and verified to satisfy performance specifications using the proposed method in Chapter 3 in continuous-time domain. The algorithm is implemented in continuous-time domain as the Nyquist frequency is at more than 100 times away from the shaped resonant mode. Besides, constraints are placed on the plant parameters during synthesis in order to ensure physical realizability of the plant design. The construction of a MagLev planar motor for EUV lithography is a furthering of the work on the linear motor, in which actuator saturation is to be included as a nonlinearity.

2. Integrated servo-mechanical design considering zeros of sampled systems:

   Using the proposed algorithms in this dissertation, a discrete-time plant model is obtained which can be realized by performing an inverse Zero-Order Hold (ZOH) followed by curve-fitting. This is due to the fact that there are in general no simple closed-form expressions for sampling zeros resulting from ZOH discretization. However, the limiting cases for small or large sampling periods can be characterized [50]. In order to simplify the realization of the discrete-time plant model, the effects of specifying the sampling zero during the design phase as the limiting value with small perturbations can be investigated.

3. Integrated servo-mechanical design for attenuating Non-Repeatable Run-Out (NRRO) resulting from both mechanical vibrations and external disturbances:

   In this dissertation, the focus of integrated servo-mechanical design is on the attenuation of NRRO induced by mechanical vibrations of the resonant modes. However, NRRO includes external disturbances such as noise with random phase [13]. As such, it is important to ensure that disturbance attenuation of NRRO resulting from mechanical vibrations do not result in spillover effects which amplify the external disturbances. In addition, the effects of mechanical redesign on the NRRO spectrum has to be investigated as well.

4. Integrated servo-mechanical design for attenuation of aliased NRRO:

   Aliased narrow-band disturbances are commonly encountered as a result of sampling, and several multirate control techniques [80–82] have been proposed in the literature. Modification of the algorithm for shaping of mechanical resonant poles and anti-resonant zeros at above Nyquist frequency will possibly allow the advantages of integrated servo-mechanical design to remain applicable. The graphical approach proposed in Chapter 4 is based on designing a fictitious system $\hat{P}_D C$ to satisfy performance and robust stability specifications, after which allowable regions for the Nyquist plot of the open loop transfer function $P_D C$ can be determined. This method can possibly be extended to the shaping of mechanical resonant modes at above Nyquist frequency as the discrete-time lifting technique can be applied to the fictitious system.

Bibliography

[1] T. Yamaguchi, M. Hirata, and C. K. Pang, *Advances in High-Performance Motion Control of Mechatronic Systems.* Boca Raton, FL, USA: CRC Press, 2013.

[2] International Roadmap Committee, "International technology roadmap for semiconductors 2013 edition executive summary," April 2014. [Online]. Available: `http://www.itrs.net/Links/2013ITRS/2013Chapters/2013ExecutiveSummary.pdf`.

[3] D. Anderson, "HDD opportunities & challengers, now to 2020," Seagate, May 2013. [Online]. Available: `https://www.dtc.umn.edu/resources/bd2013_anderson.pdf`.

[4] C. K. Pang, T. S. Ng, F. L. Lewis, and T. H. Lee, "Managing complex mechatronics R&D: A systems design approach," *IEEE Transactions on Systems, Man, and Cybernetics Part A: Systems and Humans*, vol. 42, no. 1, pp. 57–67, 2012.

[5] K. Ohnishi, "A new servo method in mechatronics," *Transactions of the Japanese Society of Electrical Engineering*, vol. 107-D, pp. 83–86, 1987.

[6] S. P. Chang, "A disturbance observer for robot manipulators with application to electronic components assembly," *IEEE Transactions on Industrial Electronics*, vol. 42, no. 5, pp. 487–493, 1995.

[7] X. Chen and M. Tomizuka, "A minimum parameter adaptive approach for rejecting multiple narrow-band disturbances with application to hard disk drives," *IEEE Transactions on Control Systems Technology*, vol. 20, no. 2, pp. 408–415, 2012.

[8] T. Atsumi, T. Arisaka, T. Shimizu, and H. Masuda, "Head-positioning control using resonant modes in hard disk drives," *IEEE/ASME Transactions on Mechatronics*, vol. 10, no. 4, pp. 378–384, 2005.

[9] J. Zheng, G. Guo, Y. Wang, and W. E. Wong, "Optimal narrow-band disturbance filter for PZT-actuated head positioning control on a spinstand," *IEEE Transactions on Magnetics*, vol. 42, no. 11, pp. 3745–3751, 2006.

[10] F. Hong and C. K. Pang, "A peak filtering method with improved transient response for narrow-band disturbance rejection in hard disk drives," *International Journal of Systems Science*, vol. 45, no. 2, pp. 109–119, 2014.

[11] M. Kobayashi, S. Nakagawa, and S. Nakamura, "A phase-stabilized servo controller for dual-stage actuators in hard disk drives," *IEEE Transactions on Magnetics*, vol. 39, no. 2, pp. 844–850, 2003.

[12] W. C. Messner, M. D. Bedillion, X. Lu, and D. Karns, "Lead and lag compensators with complex poles and zeros: Design formulas for

modeling and loop shaping," *IEEE Control Systems Magazine*, vol. 27, no. 1, pp. 44–54, 2007.

[13] T. Yamaguchi, M. Hirata, and C. K. Pang, *High-Speed Precision Motion Control*. Boca Raton, FL, USA: CRC Press, 2011.

[14] C. K. Pang, F. Hong, and W. Wang, "Integrated servo-mechanical control systems design using Nyquist plots for high-performance mechatronics," *Microsystem Technologies*, vol. 18, no. 9–10, pp. 1719–1729, 2012.

[15] K. Zhou, J. C. Doyle, and K. Glover, *Robust and Optimal Control*. Englewood Cliffs, NJ, USA: Prentice Hall, 1996.

[16] V. L. Kharitonov, "Asymptotic stability of an equilibrium position of a family of systems of linear differential equations," *Differentsial'nye Uravneniya*, vol. 14, pp. 2086–2088, 1978.

[17] R. Tempo, G. Calafiore, and F. Dabbene, *Randomized algorithms for analysis and control of uncertain systems with applications*. London, United Kingdom: Springer-Verlag, 2013.

[18] R. E. Skelton, "Model error concepts in control design," *International Journal of Control*, vol. 49, no. 5, pp. 1725–1753, 1989.

[19] Q. Li, W. J. Zhang, and L. Chen, "Design for control - a concurrent engineering approach for mechatronic systems design," *IEEE/ASME Transactions on Mechatronics*, vol. 6, no. 2, pp. 161–169, 2001.

[20] C. Mohtadi, "Bode's integral theorem for discrete-time systems," *IEE Proceedings*, vol. 137, no. 2, pp. 57–66, 1990.

[21] Aberdeen Group, "System design: New product development for mechatronics," January 2008. [Online]. Available: `http://www.plm.automation.siemens.com/zh_cn/Images/Aberdeen_MechatronicsSystemDesignBenchmark_nonlogo_Jan08_tcm78-58217.pdf`.

[22] H. K. Fathy, J. A. Reyer, P. Y. Papalambros, and A. G. Ulsoy, "On the coupling between the plant and controller optimization problems," in *Proceedings of the 2001 American Control Conference*, pp. 1864–1869, Arlington, VA, USA, June 25–27, 2001.

[23] M. J. Smith, K. M. Grigoriadis, and R. E. Skelton, "Optimal mix of passive and active control in structures," *Journal of Guidance, Control, and Dynamics*, vol. 15, no. 4, pp. 912–919, 1992.

[24] K. M. Grigoriadis, G. Zhu, and R. E. Skelton, "Optimal redesign of linear systems," *ASME Journal of Dynamic Systems, Measurement and Control*, vol. 118, no. 3, pp. 598–605, 1996.

[25] K. M. Grigoriadis and F. Wu, "Integrated $\mathcal{H}_\infty$ plant/controller design via linear matrix inequalities," in *Proceedings of the 36th IEEE Conference on Decision and Control*, pp. 789–790, San Diego, CA, USA, December 10–12, 1997.

[26] K. Hiramoto and K. M. Grigoriadis, "Integrated design of structural and control systems with a homotopy like iterative method," *International Journal of Control*, vol. 79, no. 9, pp. 1062–1073, 2006.

[27] J. Lu and R. E. Skelton, "Integrating structure and control design to achieve mixed $\mathcal{H}_2/\mathcal{H}_\infty$ performance," *International Journal of Control*, vol. 73, no. 16, pp. 1449–1462, 2010.

[28] J. Onoda and R. T. Haftka, "An approach to structure/control simultaneous optimization for large flexible spacecraft," *AIAA Journal*, vol. 25, no. 8, pp. 1133–1138, 1987.

[29] H. K. Fathy, P. Y. Papalambros, A. G. Ulsoy, and D. Hrovat, "Nested plant/controller optimization with application to combined passive/active automotive suspensions," in *Proceedings of the 2003 American Control Conference*, pp. 3375–3380, Denver, CO, USA, June 4–6, 2003.

[30] B. A. Paden and J. Moehlis, "Point-to-point control near heteroclinic orbits: Plant and controller optimality conditions," *Automatica*, vol. 49, no. 12, pp. 3562–3570, 2013.

[31] I. Kajiwara and A. Nagamatsu, "Simultaneous optimum design of structure and control systems by sensitivity analysis," *Finite Elements in Analysis and Design*, vol. 14, no. 2–3, pp. 187–195, 1993.

[32] R. J. Niewoehner, *Plant/controller optimization by convex methods.* PhD thesis, Naval Postgraduate School, Monterey, CA, USA, 1994.

[33] B. H. Wilson, C. Erin, and A. Messac, "Optimal design of a vibration isolation mount using physical programming," *ASME Journal of Dynamic Systems, Measurement and Control*, vol. 121, no. 2, pp. 171–178, 1999.

[34] T. Ravichandran, D. Wang, and G. Heppler, “Simultaneous plant-controller design optimization of a two-link planar manipulator,” *Mechatronics*, vol. 16, no. 3–4, pp. 233–242, 2006.

[35] J. M. Velni, M. Meisami-Azad, and K. M. Grigoriadis, “Integrated damping parameter and control design in structural systems for $\mathcal{H}_2$ and $\mathcal{H}_\infty$ specifications,” *Structural and Multidisciplinary Optimization*, vol. 38, no. 4, pp. 377–387, 2009.

[36] K. Hiramoto, T. Matsuoka, and K. Sunakoda, “Simultaneous optimal design of the Lyapunov-based semi-active vibration control device: Inverse Lyapunov approach,” *Journal of Pressure Vessel Technology*, vol. 134, no. 6, pp. 061211–1–061211–13, 2012.

[37] M. Bozca, A. Mugan, and H. Temeltas, “Decoupled approach to integrated optimum design of structures and robust control systems,” *Structural and Multidisciplinary Optimization*, vol. 36, no. 2, pp. 169–191, 2008.

[38] S. Hara, T. Iwasaki, and F. Shimizu, “Finite frequency characterization of easily controllable mechanical systems under control effort constraint,” in *Proceedings of the 15th IFAC World Congress*, pp. 332–337, Barcelona, Spain, July 21–26, 2002.

[39] T. Iwasaki, “Integrated system design by separation,” in *Proceedings of the 1999 IEEE International Conference on Control Applications*, pp. 97–102, Kohala Coast, HI, USA, August 22–27, 1999.

[40] T. Iwasaki, S. Hara, and H. Yamauchi, “Dynamical system design from a control perspective: Finite frequency positive-realness approach,”

IEEE Transactions on Automatic Control, vol. 48, no. 8, pp. 1337–1354, 2003.

[41] M. Kanno and S. Hara, “Symbolic-numeric hybrid optimization for plant/controller integrated design in $\mathcal{H}_\infty$ loop-shaping design,” *Journal of Math for Industry*, vol. 4, no. 2012B-8, pp. 135–140, 2012.

[42] T. Semba, F. Y. Huang, and M. T. White, “Integrated servo/mechanical design of HDD actuators and bandwidth estimation,” *IEEE Transactions on Magnetics*, vol. 39, no. 5, pp. 2588–2590, 2003.

[43] T. H. Yan, X. D. Chen, and R. M. Lin, “Servo system modeling and reduction of mechatronic system through finite element analysis for control design,” *Mechatronics*, vol. 18, no. 9, pp. 466–474, 2008.

[44] T. Atsumi, “Head-positioning control of hard disk drives through the integrated design of mechanical and control systems,” *International Journal of Automation Technology*, vol. 3, no. 3, pp. 277–285, 2009.

[45] K. Suzuki, E. Soga, S. Nakagawa, and T. Shimizu, “A U-shaped actuation system for dual-stage actuators used in hard disk drives,” *Microsystem Technologies*, vol. 18, no. 9–10, pp. 1543–1547, 2012.

[46] T. Iwasaki and S. Hara, “Generalized KYP lemma: Unified frequency domain inequalities with design applications,” *IEEE Transactions on Automatic Control*, vol. 50, no. 1, pp. 41–59, 2005.

[47] W. Chen and M. Sim, “Goal-driven optimization,” *Operations Research*, vol. 57, no. 2, pp. 342–357, 2009.

[48] C. Du and L. Xie, *Modeling and Control of Vibration in Mechanical Systems.* Boca Raton, FL, USA: CRC Press, Taylor and Francis Group, 2010.

[49] L. Hitz and B. D. O. Anderson, "Discrete positive-real functions and their application to system stability," *Proceedings IEE*, vol. 116, no. 1, pp. 153–155, 1969.

[50] K. J. Astrom, P. Hagander, and J. Sternby, "Zeros of sampled systems," *Automatica*, vol. 20, no. 1, pp. 31–38, 1984.

[51] S. P. Bhattacharyya, H. Chapellat, and L. H. Keel, *Robust Control: The Parametric Approach.* Englewood Cliffs, NJ, USA: Prentice Hall, 1995.

[52] A. Karimi, H. Khatibi, and R. Longchamp, "Robust control of polytopic systems by convex optimization," *Automatica*, vol. 43, no. 8, pp. 1395–1402, 2007.

[53] M. S. Sadabadi and A. Karimi, "Fixed-order $\mathcal{H}_\infty$ and $\mathcal{H}_2$ controller design for continuous-time polytopic systems: An LMI-based approach," in *Proceedings of the 2013 European Control Conference*, pp. 1132–1137, Zurich, Switzerland, July 17–19, 2013.

[54] M. C. Campi and E. Weyer, "Non-asymptotic confidence sets for the parameters of linear transfer functions," *IEEE Transactions on Automatic Control*, vol. 55, no. 12, pp. 2708–2720, 2010.

[55] G. C. Calafiore, F. Dabbene, and R. Tempo, "Research on probabilistic methods for control system design (survey paper)," *Automatica*, vol. 47, no. 7, pp. 1279–1293, 2011.

[56] S. Garatti and M. C. Campi, "Modulating robustness in control design: Principles and algorithms," *IEEE Control Systems Magazine*, vol. 33, no. 2, pp. 36–51, 2013.

[57] L. Hong, Y. Yang, and L. Zhang, "Sequential convex approximations to joint chance constrained programs: A Monte Carlo approach," *Operations Research*, vol. 59, no. 3, pp. 617–630, 2011.

[58] B. R. Barmish and C. M. Lagoa, "The uniform distribution: A rigorous justification for its use in robustness analysis," *Mathematics of Control Signals and Systems*, vol. 10, no. 3, pp. 203–222, 1997.

[59] C. M. Lagoa and B. R. Barmish, "Distributionally robust Monte Carlo simulation: A tutorial survey," in *Proceedings of the 15th IFAC World Congress*, pp. 1327–1338, Barcelona, Spain, July 21–26, 2002.

[60] D. Bertsimas and M. Sim, "Tractable approximations to robust conic optimization problems," *Mathematical Programming*, vol. 107, no. 1–2, pp. 5–36, 2006.

[61] A. Ben-Tal, L. E. Ghaoui, and A. Nemirovski, *Robust Optimization*. Princeton, NJ, USA: Princeton University Press, 2009.

[62] W. Chen, M. Sim, J. Sun, and C. P. Teo, "From CVaR to uncertainty set: Implications in joint chance-constrained optimization," *Operations Research*, vol. 58, no. 2, pp. 470–485, 2010.

[63] S. Hara, D. Shiokata, and T. Iwasaki, "Fixed order controller design via generalized KYP lemma," in *Proceedings of the 2004 IEEE International Conference on Control Applications*, pp. 1527–1532, Taipei, Taiwan, September 2–4, 2004.

[64] B. D. O. Anderson, S. Dasgupta, P. Khargonekar, F. J. Kraus, and M. Mansour, “Robust strict positive realness: Characterization and construction,” *IEEE Transactions on Circuits and Systems*, vol. 37, no. 7, pp. 869–875, 1990.

[65] Y. Z. Tan, M. Tang, C. K. Pang, T. S. Ng, F. Hong, and T. H. Lee, “Integrated servo-mechanical design of distribution-based robust mechatronics using GKYP Lemma,” in *Proceedings of the 6th IFAC Symposium on Mechatronic Systems*, pp. 511–516, Hangzhou, China, April 10–12, 2013.

[66] W. C. Messner and H. Shragai, “Loop shaping controller design using the Sbode plot,” in *Proceedings of the 2001 American Control Conference*, pp. 2792–2796, Arlington, VA, USA, June 25–27, 2001.

[67] T. Atsumi and W. C. Messner, “Modified Bode plots for robust performance in SISO systems with structured and unstructured uncertainties,” *IEEE Transactions on Control Systems Technology*, vol. 20, no. 2, pp. 356–368, 2012.

[68] J. D. Taylor and W. C. Messner, “Controller design for nonlinear systems using the contoured robust controller Bode plot,” *International Journal of Robust and Nonlinear Control*, in press, DOI:10.1002/rnc.3049.

[69] K. Z. Liu, “A high-performance robust control method based on the gain and phase information of uncertainty,” *International Journal of Robust and Nonlinear Control*, in press, DOI:10.1002/rnc.3125.

[70] H. H. Rosenbrock, *Computer-Aided Control System Design*. Waltham, MA, USA: Academic Press, Elsevier, 1974.

[71] S. Yabui, A. Okuyama, M. Kobayashi, and T. Atsumi, "Optimization of adaptive feedforward repeatable run-out cancellation for positioning control system of hard disk drives," *Microsystem Technologies*, vol. 18, no. 9–10, pp. 1703–1709, 2012.

[72] G. Zames, "On the input-output stability of time-varying nonlinear feedback systems-part II: Conditions involving circles in the frequency plane and sector nonlinearities," *IEEE Transactions on Automatic Control*, vol. 11, no. 3, pp. 465–476, 1966.

[73] Y. Maeda and M. Iwasaki, "Circle condition-based feedback compensation with frequency shaping for improvement of settling performance," *IEEE Transactions on Industrial Electronics*, vol. 61, no. 10, pp. 5500–5508, 2014.

[74] J. Zhou, "Sequential circle criterion approach for robustly stabilizing individual generators with SVC," *International Journal of Robust and Nonlinear Control*, in press, DOI: 10.1002/rnc.3227.

[75] B. Brogliato, R. Lozano, B. Maschke, and O. Egeland, *Dissipative Systems Analysis and Control: Theory and Applications (2nd Edition)*. New York, NY, USA: Springer-Verlag, 2007.

[76] I. R. Petersen and A. Lanzon, "Feedback control of negative-imaginary systems," *IEEE Control Systems Magazine*, vol. 30, no. 5, pp. 54–72, 2010.

[77] B. D. O. Anderson, “The small-gain theorem, the passivity theorem and their equivalence,” *Journal of the Franklin Institute*, vol. 293, no. 2, pp. 105–115, 1972.

[78] H. Khatibi and A. Karimi, “$\mathcal{H}_\infty$ controller design using an alternative to Youla parameterization,” *IEEE Transactions on Automatic Control*, vol. 55, no. 9, pp. 2119–2123, 2010.

[79] C. Wagner and N. Harned, “EUV lithography: Lithography gets extreme,” *Nature Photonics*, vol. 4, no. 1, pp. 24–26, 2010.

[80] H. Fujimoto, *General Framework of Multirate Sampling Control and Applications to Motion Control Systems.* PhD thesis, The University of Tokyo, Tokyo, Japan, 2000.

[81] T. Atsumi, “Disturbance suppression beyond Nyquist frequency in hard disk drives,” *Mechatronics*, vol. 20, no. 1, pp. 67–73, 2010.

[82] Y. Z. Tan, C. K. Pang, F. Hong, and T. H. Lee, “Aliased narrow-band disturbance rejection using phase-stabilization above Nyquist frequency,” *IEEE Transactions on Magnetics*, vol. 49, no. 6, pp. 2693–2696, 2013.

List of Publications

- International refereed journals

  1. C. K. Pang, Y. Z. Tan, and T. H. Lee, “Integrated servo-mechanical design of chance-constrained robust mechatronics using Nyquist plots,” *International Journal of Robust and Nonlinear Control*, submitted.
  2. C. K. Pang, Y. Z. Tan, T. S. Ng, and T. H. Lee, “Integrated servo-mechanical design of robust mechatronics based on ambiguous chance constraint,” *IEEE Transactions on Control System Technologies*, submitted.
  3. Y. Z. Tan, C. K. Pang, F. Hong, and T. H. Lee, “Integrated servo-mechanical design of high-performance mechatronics using generalized KYP Lemma,” *Microsystem Technologies*, Vol. 19, Nos. 9-10, pp. 1549-1557, September 2013.
  4. Y. Z. Tan, C. K. Pang, F. Hong, and T. H. Lee, ”Aliased narrow-band disturbance rejection using phase-stabilization above Nyquist frequency,” *IEEE Transactions on Magnetics*, Vol. 49, No. 6, pp. 2693-2696, June 2013.

- International refereed conference proceedings

  1. Y. Z. Tan, C. K. Pang, T. S. Ng, and T. H. Lee, "Integrated servo-mechanical design of robust mechatronics based on low-order moments and support," in *Proceedings of the 2014 IEEE AMC*, pp. 49-54, Yokohama, Japan, March 14-16, 2014 (invited).
  2. Y. Z. Tan, C. K. Pang, T. H. Lee, and T. J. Teo, "Convex separable parametrization in integrated servo-mechanical design for high-performance mechatronics," in *Proceedings of the 2013 IEEE IECON*, SS28-2, pp. 6446-6451, Vienna, Austria, November 10-13, 2013 (invited).
  3. Y. Z. Tan, M. Tang, C. K. Pang, T. S. Ng, F. Hong, and T. H. Lee, "Integrated servo-mechanical design of distribution-based robust mechatronics using GKYP Lemma," in *Proceedings of the 6 th IFAC Symposium on Mechatronic Systems*, MECH2013–0039, pp. 511-516, Hangzhou, China, April 10-12, 2013 (invited).
  4. Y. Z. Tan, C. K. Pang, F. Hong, and T. H. Lee, "Aliased NRRO rejection using phase-stabilization above Nyquist frequency," in *Digests of the 2012 APMRC*, DS-5, Singapore, October 31-November 2, 2012.
  5. Y. Z. Tan, C. K. Pang, F. Hong, and T. H. Lee, "Integrated servo-mechanical design of high-performance mechanical systems using generalized KYP Lemma," in *Proceedings of the 2012 JSME-IIP/ASME-ISPS Joint Conference on MIPE*, S17_05, pp. 376-378, Santa Clara, CA, USA, June 18-20, 2012.
  6. Y. Z. Tan, C. K. Pang, F. Hong, S. Won, and T. H. Lee, "Hystere-

sis compensation of piezoelectric actuators in dual-stage hard disk drives," in *Proceedings of the 2011 ASCC*, TuB3.2, pp. 1024-1029, Kaohsiung, Taiwan, May 15-18, 2011 (invited).